Geosciences and engineering : a publication of the University of Miskolc

4. évf. 6. sz. / 2015

Dobróka Mihály Preface	7
Drahos D. - Galsa A. Modeling Groningen Effect on Deep Laterolog	9-21
Somogyi Molnár J. - Kiss A. - Dobróka M. - Szűcs I. An Automatic Test System to Measure Acoustic Velocities: Proof for the Applicability of a New Rock Physical Model	22-35
Molnár G. - Timár G. Inversion Application in Cartography: Estimation of the Parameters of the Best Fitting Cassini-projections of the First Habsburg Military Survey	36-44
Szabó N. P. - Kiss A. - Halmágyi A. Hydrogeophysical Characterization of Groundwater Formations Based on Well Logs: Case Study on Cenozoic Clastic Aquifers in East Hungary	45-71
Molnár G. Joint Inversion of Different Types of Geodetic Measurements to Obtain Accurate Horizontal Coordinates	72-80
Völgyesi L. - Tóth Gy. - Dobróka M. Inversion Reconstruction of 3D Gravity Potential Function Including Vertical Deflections	81-92
Balázs L. Inversion of Well Logging Measurements with a Constant Interval Parameter	93-104
Nádasi E. - Madarasi A. - Turai E. Magnetotelluric Exploration in the Vicinity of Irota and Gadna	105-115
Szűcs P. - Fejes Z. - Zákány B. - Székely F. - Turai E. - Gyulai Á. - Szabó N. P. - Baracza M. K. The Improvement of the Regional Flow Model of the Tokaj Mountains with the Help of Geophysical Inversion Methods	116-124

PREFACE

The Geophysics Department at the University of Miskolc together with the Committee on Geophysics of the Hungarian Academy of Sciences, the Geoinformatical Work-Committee of the Regional Committee in Miskolc HAS and the North-Hungarian Group of the Association of Hungarian Geophysicists organize *Conference on Inversion* traditionally every two years. The event provides great opportunity for scientists to show their latest results in the different fields of geophysical inversion.

This special issue contains a colorful selection from the topics presented at the conference in autumn 2014. Most of the papers cover the fields of geophysics: modeling the Groningen effect on deep laterolog, acoustic wave velocity measuring system and rock physical model for the interpretation, inversion reconstruction of 3D gravity potential function, inversion of well logging data, results of magnetotelluric surveying. Hydrogeophysical applications of statistically processed nuclear and electric well logging data as well as regional flow model are presented. Two papers discuss the possibilities provided by inversion techniques in geodesy and cartography.

It is always a pleasure to attend the Conference on Inversion, to meet colleagues and to make conversations about newly developed techniques. The articles in this issue may encourages the Reader to participate at the next event.

Prof. Mihály Dobróka, DSc
University of Miskolc

Geosciences and Engineering, Vol. 4, No. 6 (2015), pp. 9–21.

MODELING GRONINGEN EFFECT ON DEEP LATEROLOG

DEZSŐ DRAHOS–ATTILA GALSA

Department of Geophysics and Space Sciences, Eötvös Loránd University, Budapest, Hungary
drahos@pangea.elte.hu, gali@pangea.elte.hu

Abstract. Two-dimensional finite element numerical modeling has been carried out to investigate the Groningen effect on an apparent resistivity log recorded by deep penetration laterolog sonde (LLD). A method was developed to implement numerically the laterolog operating principle for an LLD device with finite extent in an inhomogeneous medium. The numerical model was extensively tested to map the effect of the mesh resolution, the domain size and the borehole mud. Artificial two- and three-layer models were studied to measure the influence of the Groningen effect on LLD logs. Computation of the apparent resistivity log was made along a typical geological section in the Fore-Sudetic Monocline, southwestern Poland. Due to the Groningen effect an elevated resistivity value of up to 40% was observed beneath the highly resistive anhydrite/halite sequence of strata.

1. INTRODUCTION

The Dual Laterolog is a modern probe for determining the resistivity of rocks around a borehole. The advantage of the device is that it is less sensitive to the shoulder bed resistivities and the presence of borehole mud than the classical normal and lateral sondes. The Dual Laterolog sonde combination consists of the deep penetrating Laterolog-7 (LLD), the Shallow Laterolog-9 (LLS) and an RMSFL tool to calculatethe resistivity of the flushed zone.

In the Laterolog-7 operating mode the device uses three positive current electrodes – A_0, A_1 and A_2 – and four monitor electrodes – M_1, N_1, M_2, N_2. A_1 and A_2 denote the guard electrodes that focus the current field of the middle electrode A_0 to ensure maximal penetrating depth. Monitor electrodes measure the electric potential from which the apparent resistivity of the geologic formation is calculated. The return current electrode B is above the probe by some hundred meters. The potential of monitor electrodes is measured relative to the reference electrode N, which is situated between electrode B and the sonde body with seven electrodes.

In usual circumstances the potential of electrode N is practically zero, because it is far enough from A_0, A_1, A_2 and B. However, the situation is different when a highly resistive thick layer overlies the probed zone. The low resistivity mud concentrates the current of the electrode B, causing negative potential on the electrode N. As a consequence the voltage between the reference electrode N and measuring electrode M_1 is elevated, resulting in an increase of the apparent resistivity [1].This is called the Groningen effect and it is illustrated in Figure 1. Figure 2 shows the geometry of the numerical implementation of the DLT–GA device produced by Halliburton Company.

The main goal of this paper is to calculate the Groningen effect of the LLD for artificial resistivity distributions (layer boundary, bedded layer) and to show an example of the occurrence of the Groningen effect through a real geological situation. Finite element numerical modeling was applied to handle the problem, and a method was developed to implement the adjustment of the tool in the simulation. Extensive testing of the model was carried out in order to verify the results. These calculations are considered as the first steps toward solving the inversion problem, namely to compute the true resistivity of rocks more exactly.

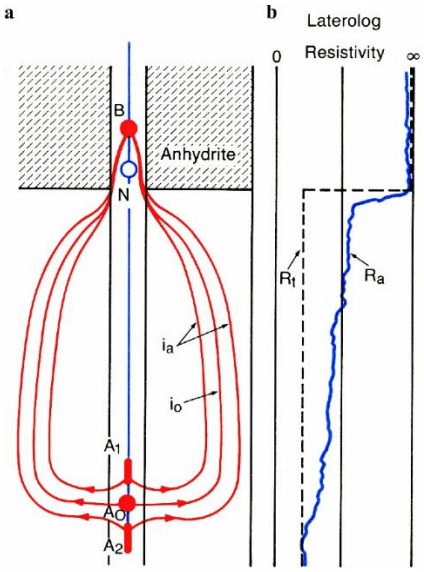

Figure 1

Illustration of the Groningen effect [1]. (a) Sketch of the current lines from LLD electrodes (A_0, A_1 and A_2) to the return electrode B. (b) Apparent resistivity increase of LLD log beneath the anhydrite layer having high true resistivity

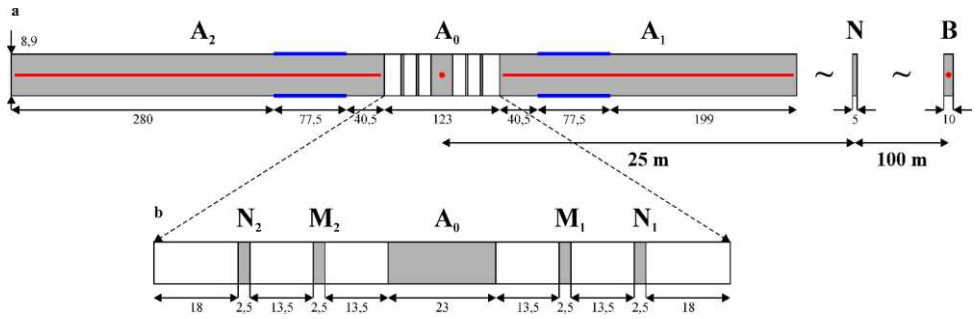

Figure 2

Sketch of the numerical implementation of the DLT–GA device produced by Halliburton Company (Technical Manual). (a) General scheme and (b) zoomed in electrode A_0 and the measuring electrodes. Size is given in cm

2. MODELING THE LATERLOLOG PRINCIPLE FOR THE GRONINGEN SITUATION

The principle of Laterolog is keeping the voltage on zero value both between the pairs of the monitor electrodes M_1 and N_1, and between M_2 and N_2 by controlling the currents emitted from the guard electrodes A_1 and A_2. In mathematical form:

$$V(M_1) = I_0\left(\tilde{R}(A_0M_1) + n_1\tilde{R}(A_1M_1) + n_2\tilde{R}(A_2M_1)\right), \tag{1}$$

$$V(N_1) = I_0\left(\tilde{R}(A_0N_1) + n_1\tilde{R}(A_1N_1) + n_2\tilde{R}(A_2N_1)\right) \tag{2}$$

and

$$V(M_2) = I_0\left(\tilde{R}(A_0M_2) + n_1\tilde{R}(A_1M_2) + n_2\tilde{R}(A_2M_2)\right), \tag{3}$$

$$V(N_2) = I_0\left(\tilde{R}(A_0N_2) + n_1\tilde{R}(A_1N_2) + n_2\tilde{R}(A_2N_2)\right). \tag{4}$$

In the above equations $\tilde{\mathrm{R}}(\mathrm{X_i Y_j})$ means the transfer resistance between the current electrode X_i and the potential electrode Y_j. As is known:

$$\tilde{R}(X_iY_j) = \frac{V(Y_j)}{I(X_i)}. \tag{5}$$

The n_1 and n_2 current intensity multiplicators are determined to satisfy the operating principle of the laterolog.They are

$$V(M_1) = V(N_1) \text{ and } V(M_2) = V(N_2). \tag{6}$$

The apparent resistivity can be calculated as

$$R_a^{LLD} = K^{LLD}\frac{V(M_1) - V(N)}{I_0}, \tag{7}$$

where K^{LLD} denotes the sonde coefficient of the LLD sonde. Because the potential of the return electrode N is zero,

$$R_a^{LLD} = K^{LLD}\frac{V(M_1)}{I_0}. \tag{8}$$

The K^{LLD} sonde coefficient comes from the potential expression for the infinite homogeneous medium with point electrodes, and has the form of [2]

$$K^{LLD} = \frac{4\pi}{\frac{1}{\overline{A_0M_1}} + n\left(\frac{1}{\overline{A_1M_1}} + \frac{1}{\overline{A_2M_1}}\right)}, \tag{9}$$

where $\overline{A_iM_j}$ denotes the distance between the electrodes and

$$n = \frac{\frac{1}{\overline{A_0M_1}} - \frac{1}{\overline{A_0N_1}}}{\frac{1}{\overline{A_1N_1}} + \frac{1}{\overline{A_2N_1}} - \frac{1}{\overline{A_1M_1}} - \frac{1}{\overline{A_2M_1}}}. \tag{10}$$

We note that the symmetrical sonde arrangement in a homogeneous medium requires only one current multiplicator to satisfy Eq. (6).

However, in the case of the Groningen situation the effect of the return current electrode is not negligible; therefore, the potential of the reference electrode N will be as follows:

$$V(N) = I_0\left\{\tilde{R}(A_0N) + n_1\tilde{R}(A_1N) + n_2\tilde{R}(A_2N) - (1+n_1+n_2)\,\tilde{R}(BN)\right\}, \tag{11}$$

and also the potential of the monitor electrodes:

$$V(M_1) = I_0\left\{\tilde{R}(A_0M_1) + n_1\tilde{R}(A_1M_1) + n_2\tilde{R}(A_2M_1) - (1+n_1+n_2)\,\tilde{R}(BM_1)\right\}, \tag{12}$$

$$V(N_1) = I_0\left\{\tilde{R}(A_0N_1) + n_1\tilde{R}(A_1N_1) + n_2\tilde{R}(A_2N_1) - (1+n_1+n_2)\,\tilde{R}(BN_1)\right\}, \tag{13}$$

$$V(M_2) = I_0\left\{\tilde{R}(A_0M_2) + n_1\tilde{R}(A_1M_2) + n_2\tilde{R}(A_2M_2) - (1+n_1+n_2)\,\tilde{R}(BM_2)\right\}, \tag{14}$$

$$V(N_2) = I_0\left\{\tilde{R}(A_0N_2) + n_1\tilde{R}(A_1N_2) + n_2\tilde{R}(A_2N_2) - (1+n_1+n_2)\,\tilde{R}(BN_2)\right\}. \tag{15}$$

The controlling conditions for the LLD are

$$V(M_1) - V(N) = V(N_1) - V(N), \tag{16}$$

from which we obtain

$$V(M_1) = V(N_1) \text{ and } V(M_2) = V(N_2) \tag{17}$$

Because the potential of the reference electrode N is negative – due to the effect of the return current electrode B – it must be taken into account when calculating the apparent resistivity,

$$R_a^{LLD} = K^{LLD} \frac{V(M_1) - V(N)}{I_0}. \tag{18}$$

Because of the finite dimensions of both the current and monitor electrodes, the calculation of the potentials can be done only by numerical modeling. A finite element numerical modeling software package, COMSOL Multiphysics [3], was applied to compute the electrode potentials by solving the Laplace equation in a 2D axisymmetrical, inhomogeneous medium:

$$\mathbf{div}\left(\frac{1}{R(r,z)} \mathbf{grad}\, V(r,z) \right) = 0, \tag{19}$$

where R is the resistivity of the rock and r, z denote the radial and vertical coordinates. When the potentials (i.e. transfer resistances, $\tilde{R}(X_i Y_j)$) are determined the next step is to compute the current multiplicators n_1 and n_2 from Eqs. (12)–(15) using the controlling principle in Eq. (17).The final step is the calculation of the R_a^{LLD} apparent resistivity. In the following part of the paper the details of the calculations are described and results are shown.

3. RESULTS

3.1. Testing the method

In order to verify the numerical results the effect of (1) the mesh resolution, (2) the model size and (3) the device response to the presence of mud on the electrode potentials and apparent resistivity was intensively tested. Obviously, the size and the distribution of the finite elements influence the solution. First, the LLD device and its surroundings were discretized using the built-in automatic mesh function in COMSOL. Electrode potentials with different mesh were compared to the solution with the coarsest resolution to compute relative potential variation (Figure 3a). Predefined discretization modes from the 'coarser' to the 'extremely fine' resulted in the range of number of elements from 35 067 to 119 945. Since automatic mesh refinement does not necessarily provide a more exact solution, local mesh refinement were applied where the current density was high. For the preferred discretization the maximal size of finite elements was restricted to 1 mm along the surface of the device and 2 mm within the metal electrodes, resulting in 366 250 elements altogether (Figure 3b). During this test only electrode A_0 and B were switched on with $I_0 = 1$ A and $I_B = -1$ A, and the resistivity of the medium and the mud was $R_t = R_m = 1$ Ωm, respectively. The sensitivity of these electrodes was the most observable and the potential varied about 3% depending on the mesh resolution.

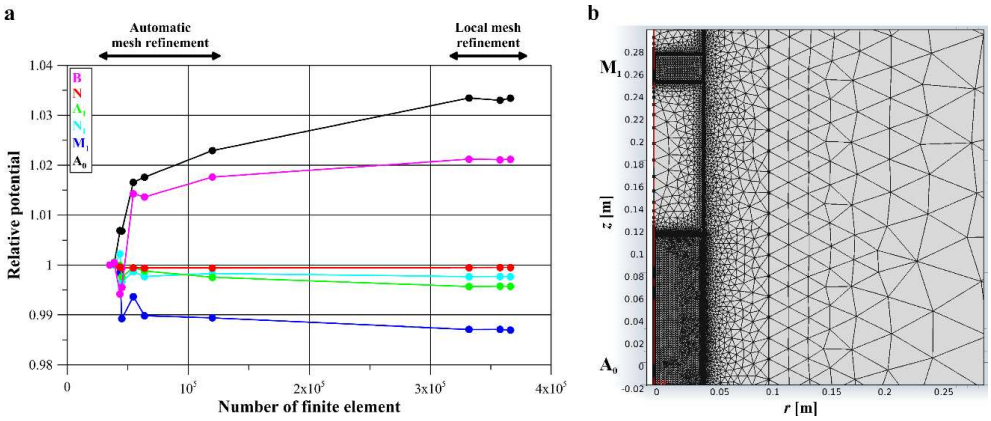

Figure 3

(a) Potential variation relative to the electrode potentials of the coarsest mesh resolution as a function of the number of finite elements. (b) Illustration of the mesh in and around electrode A_0 and M_1 for the final discretization

Second, the size of the model domain was varied to investigate the effect of the outer grounded boundary conditions on the electrode potentials. In the initial model the LLD device was encapsulated by a cylinder with radius $r_c = 100$ m and height $h_c = 325$ m (Figure 4a).

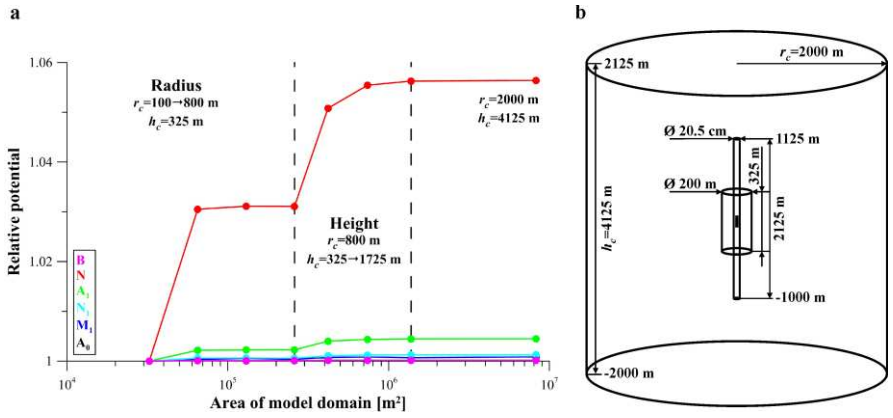

Figure 4

(a) Effect of the size of the model domain on electrode potentials. First, the radius of the outer grounded cylinder was increased; second, the height; third, the size of cylinder was doubled. (b) Sketch of the final model geometry

As a first step the radius was increased to 800 m until the potential became insensitive to the variation of the model size, then the height was enlarged to 1725 m with a fixed radius. Thirdly, the radius and the height of the cylinder were doubled to get an accurate solution. The final size of the model domain was $r_c = 2000$ m and $h_c = 4125$ m, the device with a length of about 125 m was centered in a borehole with

a diameter of 20.5 cm and length 2125 m (Figure 4b). The sonde was encircled also by an inner cylinder to ensure better resolution in the neighboring medium. Increasing the size of the model resulted in almost 6% variation in the potential of electrode N.

In order to calculate the apparent resistivity from electrode potential the sonde coefficient of the device is needed. In practice, the apparent resistivity R_a is calculated from the voltage between electrode M_1 and N according to Eq. (18). Point-wise approximation does not give an accurate solution because of the adjacent extended electrodes. However, in a homogeneous medium with known true resistivity K^{LLD} can be computed. Four model runs were made with homogeneous geological medium of R = 0.1, 1, 10 and 100 Ωm to determine the value of the sonde coefficient,

$$K^{LLD} = R\frac{I_0}{V_{M1} - V_N} \cong 0.90693m\,, \tag{20}$$

where K^{LLD} recovered the resistivity within the standard deviation of less than 0.3% for the four models.

Third, the effect of a borehole filled with low resistive mud was studied on the apparent resistivity obtained from LLD device. The true resistivity of the homogeneous medium was ranged from R_t=0.1 to 1000 Ωm at a fixed mud resistivity of R_m=1 Ωm and borehole diameter of d=20.5 cm. Figure 5 illustrates that the laterolog in deep penetration mode is almost insensitive to the presence of mud; a small deviation from the identity function (R_a=R_t) appears only at very low values of rock resistivity.

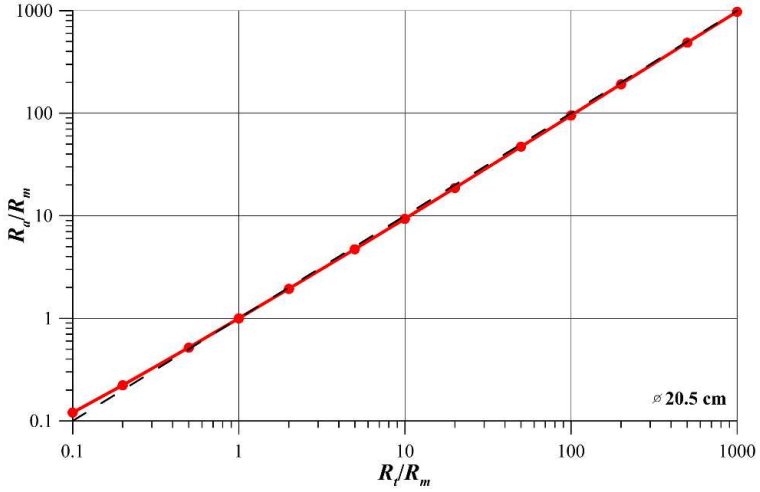

Figure 5

Relation between the apparent (R_a) and true (R_t) resistivity in the presence of borehole filled with mud. Borehole diameter is 20.5 cm, mud resistivity R_m = 1 Ωm

3.2. Device performance at layer boundaries

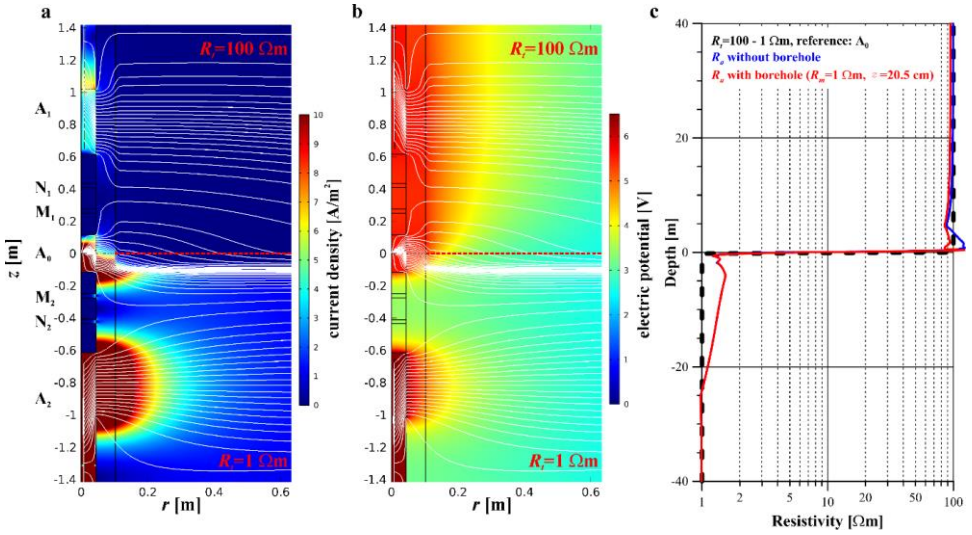

Figure 6

Behavior of the LLD device near boundary separating layers having high (top) and low (bottom) resistivity. (a) Current density and (b) electric potential field at the position where A_0 is opposite the layer boundary (dashed red line). White lines denote the current lines. (c) Apparent resistivity log across the layer boundary in the absence (blue) and presence (red) of borehole mud. The theoretical true resistivity is displayed by dashed black curve

From the point of view of the Groningen effect it is essential how the device behaves near layer boundaries. Two general tests were made to analyze the apparent resistivity logs of the LLD device. In the first model the simplest inhomogeneous situation was studied where two homogeneous layers with high (top) and low (bottom) resistivity are separated at the depth of 0 m (Figure 6). Figure 6a shows the current density distribution and current lines when A_0 is positioned opposite the layer boundary in the presence of borehole mud. It is obvious that current density yields a higher value in the low-resistive lower layer to ensure potential equivalence between measuring electrodes. Current lines tend to the lower layer. Figure 6b illustrates that the potential is much more elongated in the upper resistive layer than in the lower layer encircling the upper part of the device. If there is no borehole the apparent resistivity in the upper layer tends to the true resistivity at some distance from the boundary, while in the models including borehole the apparent resistivity stays below the true resistivity due to the low-resistive mud (Figure 6c). A maximum appears in the apparent resistivity log just above the boundary; the maximum is much more localized in the model including the borehole. The main deviation from the true resistivity curve is generated by the Groningen effect. While the reference electrode N is moving in the upper resistive layer, the effect of the return electrode B is enlarged. R_a shows a linear decreasing trend as N moves to the boundary (the distance between A_0 and N is 25 m). Theoretically, R_a becomes equal to R_t after B

has left behind the upper layer (as the sonde moves downward), but this effect is negligible. We note that the two curves (with and without borehole) run together in the lower layer because here the resistivity of the rock and the mud is equal.

The effect of a thin bedded layer with high resistivity was investigated on the apparent resistivity log. The thickness of the bed was 12 m, approximately half of the distance between A_0 and N. Owing to the thin layer effect R_a is lower than R_t within layer, and the presence of mud reduces R_a more efficiently (Figure 7). Maximums appear near the layer boundaries, similarly to the two-layer model (see Figure 6). The apparent maximums above and below the layer are asymmetrical because of the Groningen effect. As N is situated within or above the thin bed the effect of electrode B is magnified resulting in an elevated value of R_a. Apparent resistivity curves above and below the bed run together due to the horizontally homogeneous resistivity distribution.

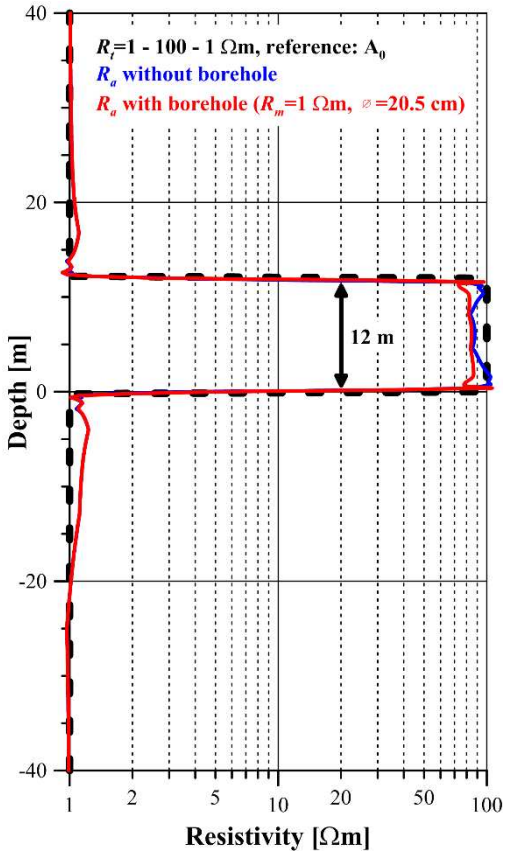

Figure 7

Effect of the thin, resistive bed on the apparent resistivity log in the absence (blue) and presence (red) of borehole mud. Theoretical true resistivity is shown by dashed black curve

3.3. Groningen effect in a geological profile

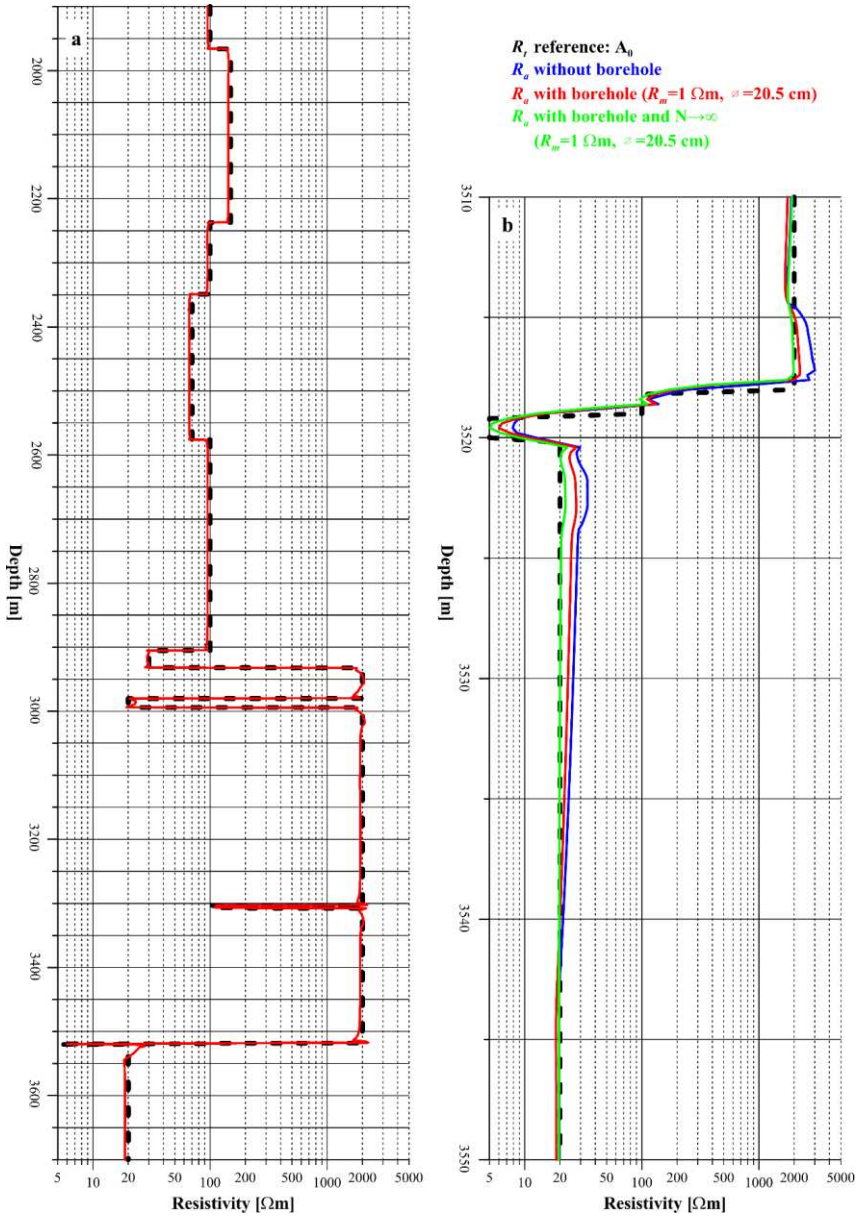

Figure 8

Apparent resistivity log along a typical geological profile in the Fore-Sudetic Monocline, southwestern Poland. (a) The whole profile, length 1800 m. (b) The lowermost part of the log where Rotliegend sandstone is overlain by anhydrite with high resistivity. True resistivity is denoted by dashed black line, apparent resistivity is blue without and red with a borehole, green shows the case when the reference electrode N is moved to infinity, i.e. V(N) = 0

Along a typical geological section in the Fore-Sudetic Monocline, southwestern Poland an apparent resistivity log was computed to test the appearance of the Groningen effect. In the upper part of the 1800 m long profile sandstone, limestone and claystone lithology alternates, which change to halite and anhydrite sequence of strata below the depth of 2930 m (Figure 8a). The Lower Anhydrite stratum, with resistivity of 2000 Ωm, is underlaid by Zechstein Limestone (3518–3519 m, $R_t \cong$ 100 Ωm), Copper Shale (3519–3520 m, $R_t \cong 5$ Ωm) and Rotliegend Sandstone (below 3520 m, $R_t \cong 20$ Ωm). A detailed description of the geological succession of strata is presented by [4].

Apparent resistivity was computed along the whole geological profile containing a borehole with a diameter of 20.5 cm filled with mud of $R_m = 1$ Ωm. R_a approximates well the true resistivity, emphasizing the insensitivity of the LLD device to the presence of the low-resistive mud. From the point of view of the Groningen effect the most relevant part of the profile is zoomed in Figure 8b. The apparent maximum in the lower part of the anhydrite and below 3520 m due to the Groningen effect is more pronounced without the borehole (blue). In the presence of low resistive mud the effect is attenuated. In theory, the apparent resistivity could be calculated if the reference electrode N was moved to infinity, that is V(N) = 0. The green curve proves that the Groningen effect is caused by the influence of the return electrode on the reference electrode, that is, when N is far from B the Groningen effect vanishes. It is worth noting that the Groningen effect enhances the apparent resistivity in the presence of the borehole mud from 20 Ωm to 27.6 Ωm (34.4 Ωm in its absence), which gives a 38% (72%) virtual increase.

Applying the Archie formula for hydrocarbon reservoirs

$$S_w = \sqrt{\frac{R_0}{R_t}} \quad and \quad S_w^{Gr} = \sqrt{\frac{R_0}{\alpha_{Gr} \cdot R_t}}, \tag{21}$$

where S_w and S_w^{Gr} denote the water saturation without and with Groningen effect, R_0 is the resistivity of the water-bearing layer, and α_{Gr} is the influence of the Groningen effect on the apparent resistivity. From Eq. (21) the virtual water saturation decrease due to the peak effect of $\alpha_{Gr} = 1.38$ gives

$$\frac{S_w^{Gr}}{S_w} = \frac{1}{\sqrt{\alpha_{Gr}}} \cong 0.85. \tag{22}$$

This means that the Groningen effect induces a virtual hydrocarbon saturation increase with a maximum of 15%. Taking into account the fact that the Groningen effect decreases linearly moving away from the high-resistive bed, and considering the distance between the dual laterolog tool and the reference electrode,the result is

anaverage 7.5% increase in hydrocarbon saturation along a zone with a thickness of A_0N = 25 m (see Fig. 8b between 3520 and 3545 m).

4. DISCUSSION AND CONCLUSIONS

A technique was developed to model numerically the response of a borehole geophysical sonde – a dual laterolog DLT–GA device produced by Halliburton Company – along a geological profile focusing on the Groningen effect. An analytical method was worked out in order to calculate the current discharge of the guard electrodes and to ensure the potential equivalence of measuring electrodes in an inhomogeneous medium. The finite element method was applied to solve the Laplace equation and the solution was verified by extensive testing of the model size and discretization and the device performance in the presence of borehole mud and at layer boundaries.

The sonde coefficient of the dual laterolog device in deep penetration mode (LLD) was calculated in different homogeneous media resulting in a value of K^{LLD} = 0.90693 m. Based on our numerical results it was established that the sonde is almost insensitive to the presence of borehole mud; a small deviation between the true and apparent resistivity curve was observed only in rocks having very low resistivity (Figure 5). Model calculations were made to present the current density and potential distribution at artificial layer boundaries as well as to analyze the appearance of the Groningen effect below a highly resistive bed. The Groningen effect elevated the observed resistivity by 20–40%, depending on the thickness and resistivity of the layer.

The method was proven through a typical stratigraphic section of Fore-Sudetic Monocline in southwestern Poland constructed from geological data and different well logs [4]. Simulations revealed unequivocally that the Groningen effect influences the resistivity log. Beneath the anhydrite sequence of strata the apparent resistivity of the underlying sandstone is elevated by a maximum value of about 40% (Figure 8b). This apparent increase might lead to the misinterpretation of well logs and false reserve estimation, thus the influence of the Groningen effect on LLD resistivity curves must be taken into account.

5. ACKNOWLEDGEMENTS

The authors are grateful to Jadwiga Jarzyna, Adam Cichy, Maria Joanna Bala and Andrzej Ossowski at AGH University of Science and Technology, Krakow for their constructive remarks and the fruitful cooperation.

6. LIST OF SYMBOLS

Symbol	Description	Unit
A	notation of current electrodes	–
M	notation of monitor electrodes	–
N	notation of monitor electrodes	–

α_{GR}	relative Groningen effect on apparent resistivity	–
$\overline{A_i M_j}$	distance between current electrode *i* and monitor electrode *j*	m
h_c	height of outer model cylinder	m
I_0	current of middle electrode	A
I_B	current of return electrode	A
K^{LLD}	LLD sonde coefficient	m
n	current multiplicator in homogeneous medium for symmetrical sonde	–
n_1	current multiplicator for upper guard electrode	–
n_2	current multiplicator for lower guard electrode	–
R	resistivity	Ωm
$\tilde{R}$	transfer resistance	Ω
R_0	resistivity of water-saturated layer	Ωm
R_a	apparent resistivity	Ωm
r_c	radius of outer model cylinder	m
R_m	borehole mud resistivity	Ωm
R_t	true resistivity of rock	Ωm
S_w	water saturation without Groningen effect	–
S_w^{Gr}	water saturation with Groningen effect	–
V	electric potential	V

7. REFERENCES

[1] SCHLUMBERGER: *Log interpretation. Principles/Applications*. Schlumberger Educational Services, Houston, USA, 198.

[2] BARLAI, Z.: Special problems in borehole geophysics. In: Hung.: *Fúrólyukban végzett geofizikai mérések speciális problémái*. Országos Kőolaj- és Gázipari Tröszt, Budapest, 1971, Vol. 1, 219.

[3] ZIMMERMAN, W. B. J.: *Multiphysics Modeling With Finite Element Methods*. World Scientific Publishing Company, Singapore, 2006.

[4] JARZYNA, J. A.–CICHY, A.–DRAHOS, D.–GALSA, A.–BALA, M. J.–OSSOWSKI, A.: New methods for modeling laterolog resistivity corrections. *Acta Geophysica,* 2015, accepted.

Geosciences and Engineering, Vol. 4, No. 6 (2015), pp. 22–35.

AN AUTOMATIC TEST SYSTEM TO MEASURE ACOUSTIC VELOCITIES: PROOF FOR THE APPLICABILITY OF A NEW ROCK PHYSICAL MODEL

JUDIT SOMOGYI MOLNÁR[1, 2]–ANETT KISS[1]–MIHÁLY DOBRÓKA[1,2]–ISTVÁN SZŰCS[3]

[1]*Department of Geophysics, University of Miskolc*
[2]*MTA–ME Geoengineering Research Group*
gfmj@uni-miskolc.hu
[3]*University of Pécs*

Abstract. In this study longitudinal (P) and transverse (S) wave velocities measured in laboratory on sandstone samples are presented. The uniaxial loading of the samples was carried out by an automatic acoustic test system. During the measurements the Freely Programmable Interface module of the software DION 7 and the acoustic software GMuG/GL Test Systems PCUSpro were used. By applying the programmed algorithm and the acoustic software the measurements become completely automatic. Measurement data were processed by a joint inversion technique based on the developed petrophysical model which describes the relationship between acoustic P and S wave velocities and pressure. The quality checked joint inversion results showed that the misfits between measured and calculated data are small, proving that the proposed petrophysical model can be applied well in practice.

1. INTRODUCTION

Determination of the pressure dependence of rock physical parameters has a key role in the accurate interpretation of geophysical measurement data. Investigation of acoustic wave velocities and elastic properties has great significance in seismic practice. The velocity of elastic waves in rocks are influenced primarily by the elastic properties of the rock-forming minerals, relative volumes of minerals, consolidation and cementation of the rock matrix, porosity, pore shape and content, pressure and temperature.

It has been observed that pressure has greater influence on velocities in the beginning phase of loading, and later it lessens and the velocities tend to a limit value. Two main theories have been published to explain this process. According to BIRCH [1] the reason for the velocity increase is the decreasing pore volume with increasing pressure. WALSH and BRACE [2] explain it with the closure of microcracks. A phenomenological theory for fractured rocks from SCHÖN [3] describes the effect of all defects (fractures, defects at grain boundaries, intragranular defects etc.). WANG et al. showed the application of this model describing the velocity vs. depth function on terrestrial and lunar rock specimens [4].

For an analytical description of the nonlinear velocity vs. pressure relationship, exponential functions are most commonly used [5] [6] [7] [8] [9] [10]. In these

empirical equations only the regression parameters are given and no physical explanation of the process is provided. In this paper a rock physical model based on quantitative explanation of the pressure dependence of seismic/acoustic velocities is introduced with the application of the constant Q model. The model is validated on laboratory data measured by an automatic test system. The system allows us to measure velocities accurately, which is important for the precise deduction of the pressure dependent elastic parameters and loss angles.

2. MEASURING SYSTEM

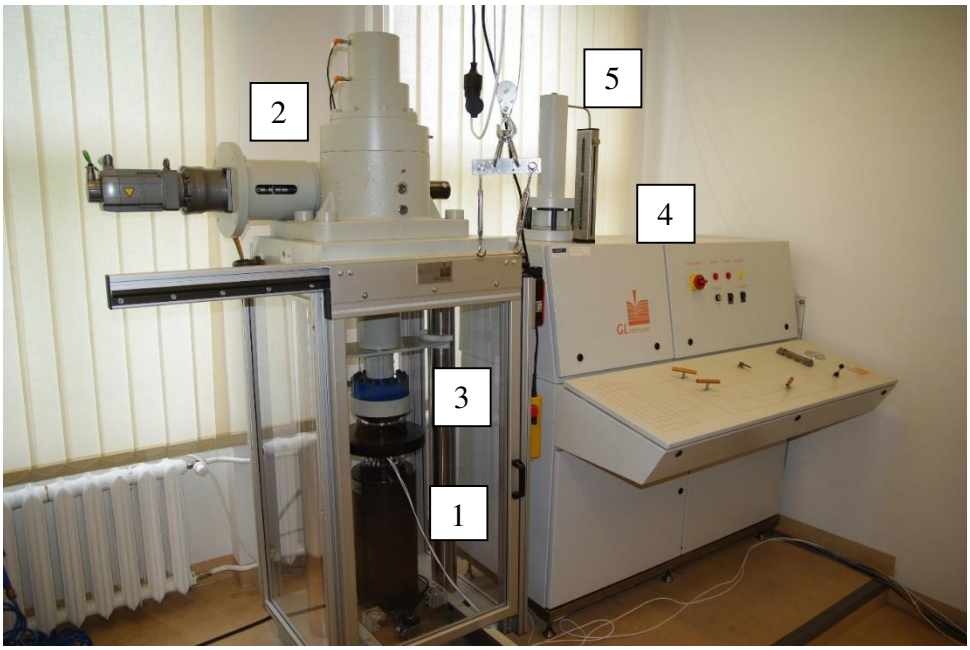

Figure 1
Automatic testing system: (1) testing cell; (2) load frame; (3) pressure plate;
(4) pressure generator; (5) piston

Acoustic longitudinal (P) and tranverse (S) wave velocities are measured in the laboratory, primarily by using the pulse transmission technique [11]. The detection of transverse wave arrival is a greater challenge than that of longitudinal. The reason is that at small transmitter-receiver distances the differentiation of P and S waves is difficult; however, if the distances are increased then also the attenuation increases and the signal-to-noise ratio decreases. We performed measurements on many different cylindrical sandstone samples with an automatic acoustic test system under uniaxial stresses. The digitally controlled test system (Figure 1) includes a pressure cell, an ultrasonic 2-channel testing device, a load frame and a pressure generator.

The pressure cell enables triaxial loading ($\sigma_1 \neq \sigma_2 = \sigma_3$) of 35 mm diameter cylindrical, maximum 100 mm height specimens. The pressure stamps of the cell are interchangeable, which allows samples with different diameters to be measured. The stamps are drained, which offers the opportunity to saturate the samples. They include also piezoelectric crystals for acoustic measurements. Transducers in the stamps have 1 MHz eigenfrequency and are sealed against the confining pressure. An electrical lead-through ED4-200-RT in the cell (operating temperature 0–50 °C, pressure 200 MPa, electric current up to 100 mA) transmits electrical supply voltage into the stamps and electrical signals out of the cell. The device uses 4-wire cables with LEMO FFA.0S plugs on both sides. At the moment only two lead-throughs are built in but it is extendable to eight (e.g. for temperature, radial and axial strain measurements). Detailed technical data can be seen in Table 1.

Table 1
Technical data of the test system

Pressure cell	
maximum operating pressure	80 MPa
maximum axial load	400 MPa
maximum axial deformation in compression	30 mm
linearity	0.05%
Ultrasonic testing device	
frequency filter	0.5 MHz, 1 MHz, 2 MHz, broadband
run time of the strike pulse	<10 ns
excitation voltage	–350 V, –550 V
amplification	–20 dB – 90 dB
averaging	2, 4, 8, …, 256
Load frame	
maximum compression force	300 kN
maximal path of the pressure plate (stroke)	100 mm
load frame stiffness	250 kN/mm
accuracy up to 30 kN	grade 1
accuracy above 30 kN	grade 0.5
digital resolution of displacement measurement system	0.05 microns
diameter of pressure plate	300 mm
hardness of pressure plate	55 HRC
Pressure generator	
maximum pressure	80 MPa
maximum volume	500 ml
pressure measurement accuracy	grade 1
stroke measurement accuracy	grade 0.5

The ultrasonic 2-channel testing device enables the possibility to measure the travel times of both P and S waves. It consists of two pairs of transmitters and receivers, input amplifier, ADC, measuring memory, signal processing unit, computer interface. Therefore the complete system is suitable for generating, receiving, converting and visualizing (real-time) ultrasonic waves, as well as evaluating their propagation properties by PC (data export in ASCII). Technical data and the experimental setup are shown in Table 1 and Figure 2, respectively.

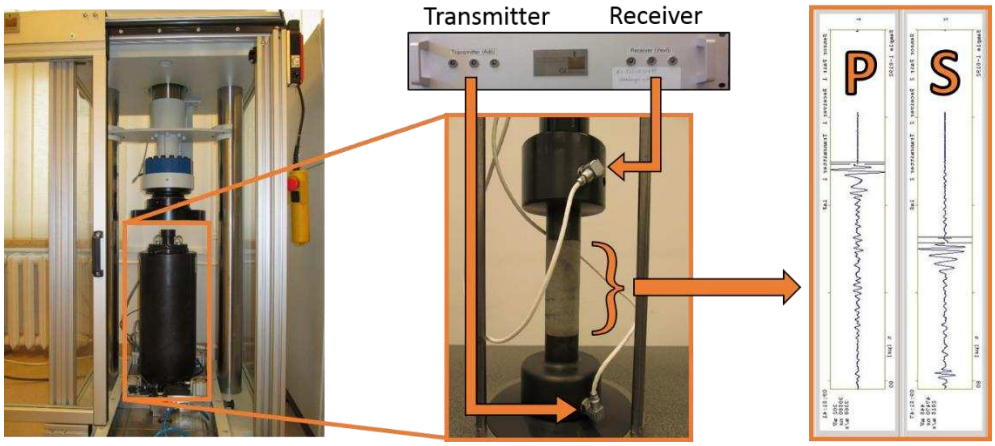

Figure 2

Experimental setup. Left: load frame and pressure cell. Middle: ultrasonic device, sandstone sample between transmitter and receiver built in the pressure stamps. Right: P and S wave arrivals

The pulse generator of the ultrasonic 2-channel testing device transmits a voltage pulse (run time 10 ns) which starts acoustic waves in the rock sample. The receivers transform these acoustic signals to voltage pulses. The arrival times of the pulse can be detected by the software GMuG/GL Test Systems PCUSpro, i.e. from the length of the sample it is possible to measure P and S wave velocities. This is the so-called pulse transmission technique. Note that the signal quality depends on the properties of the rock, i.e. in very porous and/or coarse grained rock measurement can be difficult (especially for S waves in wetted rocks, because S waves cannot physically propagate in liquids).

The system is optimized regarding high precision load measurements by its digital 2-channel controller with an extremely high resolution Synchronous Serial Interface (25 bit). The system consists of two loops: Servo 1 is the uniaxial load (see load frame in Figure 1) while Servo 2 is the confining pressure (see pressure generator in Figure 1). With the filling pump the pressure cell can be filled with oil (the sample is isolated from the oil by a rubber jacket), and thus a triaxial load ($\sigma_1 \neq \sigma_2 = \sigma_3$) can be achieved. Some technical data of the system can be seen in Table 1. High load frame stiffness is important to minimize the effect of deformation energy stored in the frame. The

accuracy of the electromechanic load frame and pressure generator is given according to ISO 7500-1.

2.1. GMuG/GL Test Systems PCUSpro software

As was mentioned, velocities can be measured automatically by the ultrasonic (US) software GMuG/GL Test Systems PCUSpro. The user interface with the settings of the software and the detected waveform can be seen in Figure 3.

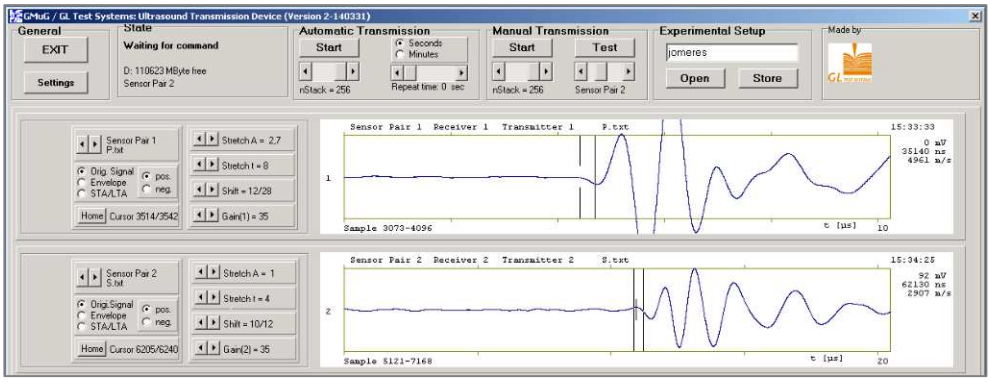

Figure 3
User interface of the ultrasonic software

It is possible to measure in test, manual or automatic mode. In test mode the real-time waveform can be seen in the display and stacking cannot be applied. The manual mode means one single measurement with optional 2^n (n=1, 2, …, 256) stacking to increase the signal-to-noise ratio. The advantage of the stacking (also available in automatic mode) is that the amplitudes of external noises can be reduced, and thus the first arrival can be picked more accurately. In automatic mode, after the elapsed measurement time the relay switches between the 2 channels (meaning P and S) thus one can measure continuously with the chosen stacking. The time between two measurements can be set between 2-120 seconds or minutes. In case of each mode the measured waveform can be stretched in the direction of both the amplitude and time axis. If it is necessary gain can be adjusted to the full waveform (maximum 80 dB).

2.2. DION7 software

DION7 is complex software for planning and executing material tests, data acquisition, as well as for controlling the elements of the system. It handles physical and virtual (i.e. calculated) channels, which can be controlled. The physical channels of the load frame (Servo 1) are load and stroke, while for the pressure generator (Servo 2) they are pressure and volume. The number of the physical channels can be extended with further sensors (e.g. temperature, radial and axial strain).

The software is built on a modular base: in our software version Easy, Manual and FPI (Freely Programmable Interface) modules are available. Each application package focuses on a typical domain of mechanical testing of materials. The Easy and Manual modules are intended for simple dynamic component testing, while with the FPI module individual and specific measurement algorithms can be programmed. With the free programmable software DION7 test procedures can run automatically. Test algorithms are made graphically using a flowchart editor. In each module it is possible to select various periodic control functions (ramp, sine haversine, rectangle, triangle, trapeze, sawtooth) whose parameters (e.g. loading velocity, frequency or amplitude) and stop criteria can be defined freely. All channels can be monitored in graphs (Figure 4).

Figure 4
User interface of DION7 – Manual module

3. MEASUREMENTS

In this paper we present the P and S wave velocity data measured on two fine-grained sandstone samples with our test system. The two cylindrical samples *A* (diameter: 3.5 cm, length: 8.9 cm, density: 2.62 g/cm^3) and *B* (diameter: 3.5 cm, length: 9.4 cm, density: 2.56 g/cm^3) were jacketed in a NBR (nitrile butadiene rubber) tube to stay fixed between the pressure stamps of the testing cell. The uniaxial loading of the samples was carried out with the automatic measurement program written in the FPI module of the software DION 7. Figure 5 shows the test algorithm. The samples were loaded stepwise with 0.05 kN/s ramp function between the single stages. As can be seen, after each stress steps a 340-second break was embedded because of the relaxation time of the samples.

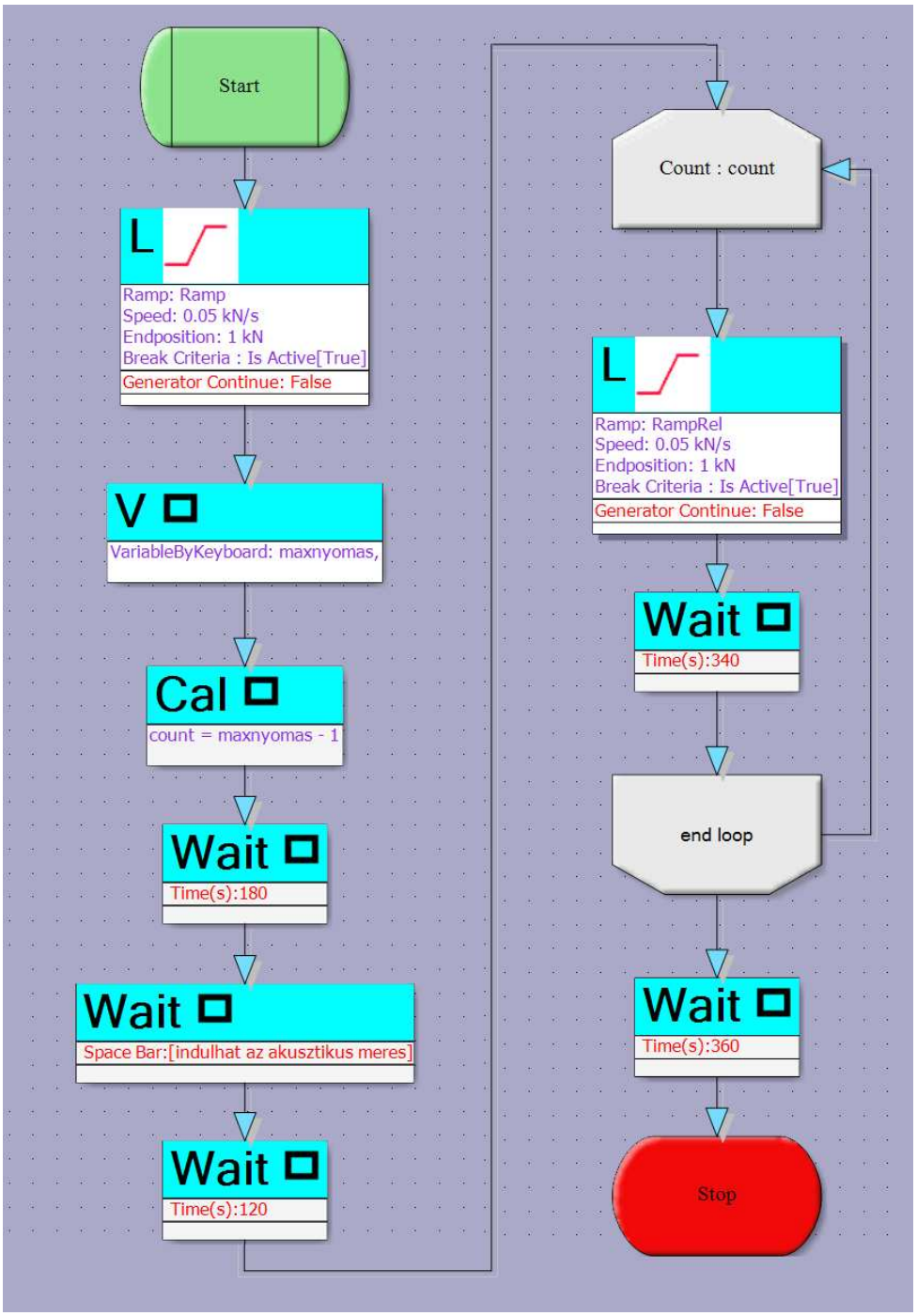

Figure 5
Test algorithm of the automatic measurement

To avoid the failure of the samples we loaded them only up to 1/3 of the uniaxial strength. The mentioned pulse transmission technique was used to measure the acoustic velocities. We applied 256-fold stacking to increase the signal/noise ratio and 32 dB gain as well as honey for coupling. By applying the programmed algorithm and the acoustic software the measurements become completely automatic.

The measured velocities versus pressure are shown in Figure 6. It can be seen that in the lower pressure range, the increase in velocities with increasing pressure is steep and nonlinear. This is due to the closure of pore volume, which significantly affects the elastic properties of rock and thereby the velocities. In the higher pressure range, the increase in velocities (with increasing pressure) become moderate as the closeable pore volume lessens.

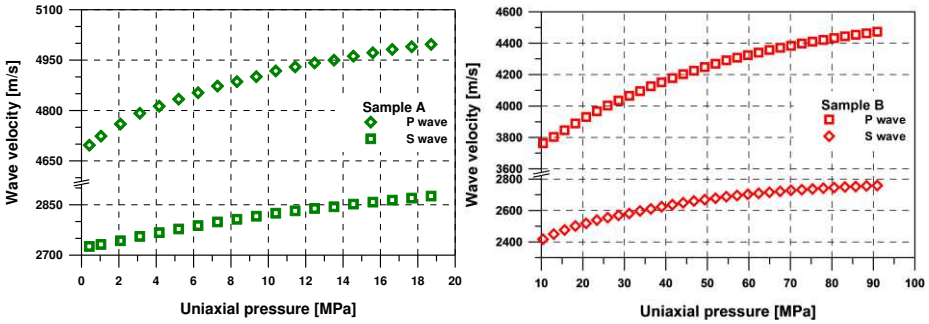

Figure 6
Measurement data of Sample A and B

4. ROCK PHYSICAL MODEL FOR THE PRESSURE DEPENDENCE OF ACOUSTIC VELOCITIES

Two main concepts can be distinguished concerning the pressure dependence of acoustic wave velocities. WALSH and BRACE [2] explain the increasing velocities under loading by the closure of microcracks. BIRCH [1] connects the process to the closure of pore space. The authors take the latter assumption as their model law, i.e. a stress increase $d\sigma$ causes unit pore volume change dV in the rock. This relationship can be described with the differential equation

$$dV = -\lambda_V V d\sigma , \tag{1}$$

where λ_V is a new rock physical constant. The inverse proportion of the change in pore volume to the change in stress is shown by the negative sign. Assuming a linear relationship between the infinitesimal change in wave velocity dv and the change in pore volume, a second differential equation can be written as well

$$dv = -\kappa dV , \tag{2}$$

where κ is the proportionality factor, a new material characteristic. The negative sign indicates that the pore volume and wave velocity change inversely. Based on Eqs. (1)–(2) the model equation of the velocity model [12] can be derived as

$$v = v_0 + \Delta v_0 (1 - exp (-\lambda_V \sigma)) , \tag{3}$$

where v_0 is the velocity at stress-free state which can be measured in laboratory, and Δv_0 is the velocity-drop [10], i.e. the velocity difference measured at maximum and zero stresses $\Delta v_0 = v_{max} - v_0$. The new rock physical parameter λ_V is the logarithmic stress sensitivity of the velocity-drop [13].

Since the base of the introduced velocity model is the pore volume, or rather the change in pore volume, which is an isotropic quantity, Eq. (3) can be rewritten for the longitudinal (α) and transverse (β) wave velocities, respectively,

$$\alpha = \alpha_0 + \Delta\alpha_0 (1 - exp(-\lambda_V \sigma)), \tag{4}$$

$$\beta = \beta_0 + \Delta\beta_0 (1 - exp(-\lambda_V \sigma)) . \tag{5}$$

5. INVERSION PROCEDURE

The P and S wave velocity data measured by the test system presented in Section 2 were processed according to the introduced velocity model. As the P and S wave velocity data sets are linked by the parameter λ_V, we applied a joint inversion procedure, where the five model parameters α_0, $\Delta\alpha_0$, β_0, $\Delta\beta_0$, λ_V have to be estimated. Since the inverse problem is overdetermined (the number of data N is greater than the number of model parameters M) the Gaussian Least Square Method was used. The workflow is shown in Figure 7.

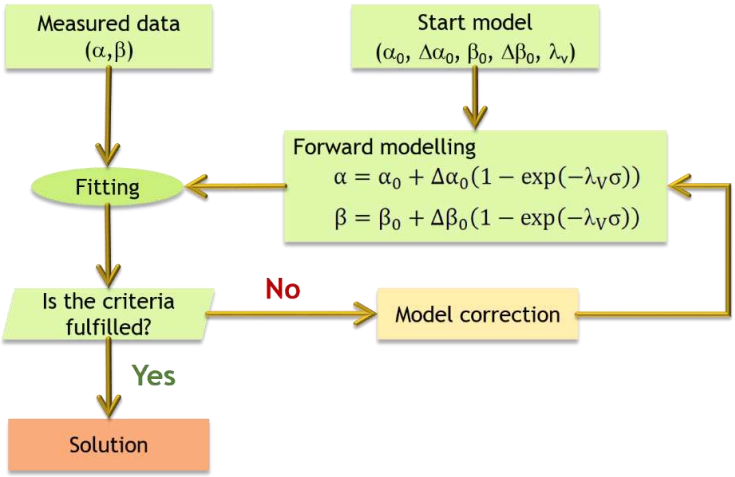

Figure 7
Flow chart of the joint inversion process

First a start model has to be defined. With its "start" model parameters the direct problem is solved in the phase of forward modeling. As the next step, the measured and calculated data have to be compared and fitted. If the distance in data space is not small enough, i.e. the deviation between the measured and calculated data is not minimal, the model parameters should be changed and the direct problem should be recalculated until the data misfit is small enough. The model parameters used in the last iteration step are considered as the results of the inversion procedure. After determining the model parameters in the joint inversion procedure, the velocities can be calculated for any arbitrary stresses.

The variance of the *i*-th estimated model parameter (σ_{mi}) is given by the *i*-th element of the main diagonal in the covariance matrix ($cov(m)$)

$$\sigma_{mi} = \sqrt{cov(m)_{ii}} \ . \tag{6}$$

The accuracy of the inversion can be described with the misfit between the measured and calculated data, which is given by the relative distance in data space, i.e. the Root Mean Square [14]

$$RMS = \sqrt{\frac{1}{N}\sum_{i=1}^{N}\left(\frac{d_i^{(m)} - d_i^{(c)}}{d_i^{(c)}}\right)^2} \cdot 100\,[\%]\,, \tag{7}$$

where $d_i^{(m)}$ is the *i*-th measured data and $d_i^{(c)}$ is the *i*-th calculated data. The reliability of the inversion estimates can be described by the mean spread

$$S = \sqrt{\frac{1}{M(M-1)}\sum_{i=1}^{M}\sum_{j=1}^{M}\left(corr(m)_{ij} - \delta_{ij}\right)^2} \ , \tag{8}$$

where δ is the Kronecker delta symbol ($\delta_{ij} = 1 \ \ if \ i = j, \ \ \delta_{ij} = 0 \ \ if \ i \neq j$) and $corr(m)$ is the correlation matrix. The small correlation coefficients (S<|0.4|) show a reliable solution. For |0.4|<S<|0.7| the correlation is moderate, and in case of |0.7|<S<|1| it is strong. In Eq. (8) the correlation matrix is calculated by

$$corr(m)_{ij} = \frac{cov(m)_{ij}}{\sqrt{cov(m)_{ii}\, cov(m)_{jj}}} \ , \tag{9}$$

and characterizes the strength of the relationship between the parameters.

6. INVERSION RESULTS

Table 2
Model parameters with estimation errors by joint inversion

Sample	α_0 (m/s)	$\Delta\alpha_0$ (m/s)	λ_V (1/MPa)	β_0 (m/s)	$\Delta\beta_0$ (m/s)	RMS (%)	S (-)
A	4696 (±3)	379.6 (±7.8)	0.0844 (±0.0040)	2711 (±2)	198.6 (±5.2)	0.11	0.52
B	3553 (±5)	1073.6 (±6.9)	0.0211 (±0.0004)	2323 (±5)	525.6 (±7.3)	0.27	0.47

Table 3
Correlation matrices

Sample A

	$\Delta\alpha_0$	$\Delta\beta_0$	λ_V	α_0	β_0
$\Delta\alpha_0$	1.00	0.59	–0.86	0.21	0.37
$\Delta\beta_0$	0.59	1.00	–0.68	0.45	–0.30
λ_V	–0.86	–0.68	1.00	–0.66	–0.43
α_0	0.21	0.45	–0.66	1.00	0.28
β_0	0.37	-0.30	–0.43	0.28	1.00

Sample B

	$\Delta\alpha_0$	$\Delta\beta_0$	λ_V	α_0	β_0
$\Delta\alpha_0$	1.00	0.21	-0.69	0.15	0.30
$\Delta\beta_0$	0.21	1.00	–0.31	0.25	–0.67
λ_V	–0.69	–0.31	1.00	–0.80	–0.43
α_0	0.15	0.25	–0.80	1.00	0.34
β_0	0.30	–0.67	–0.43	0.34	1.00

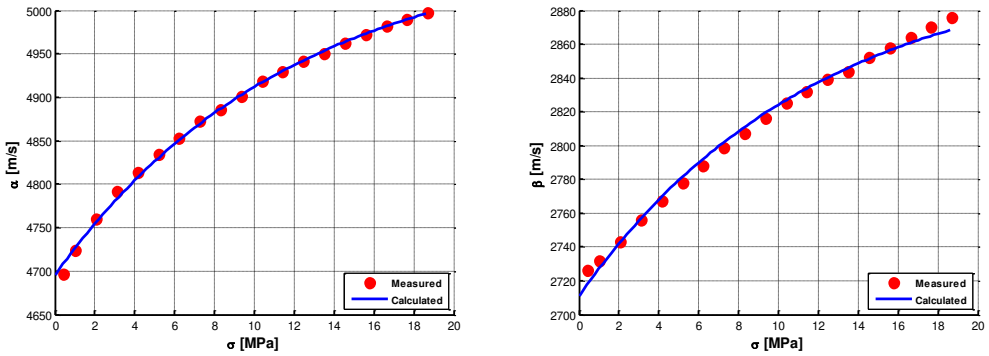

Figure 8
Velocity data measured and calculated for sample A

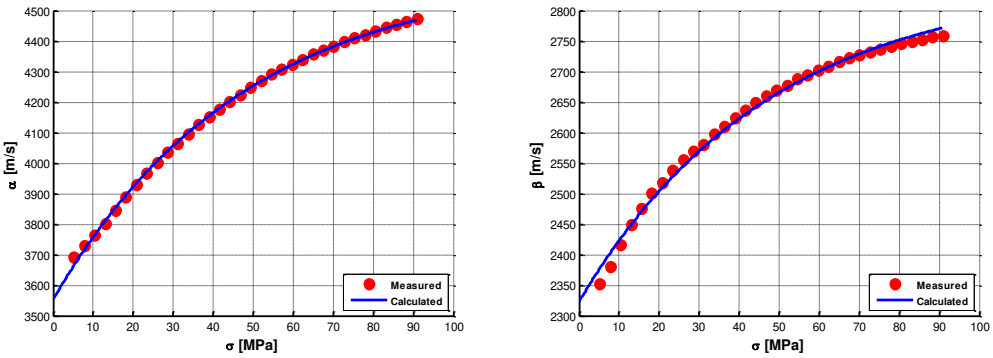

Figure 9
Velocity data measured and calculated for sample B

Measured data were inverted jointly following the algorithm in Figure 7. The estimated model parameters are summarized in Table 2 together with their estimation errors calculated by Eq. (6). With these model parameters the pressure-dependent acoustic P and S wave velocities were calculated for the whole pressure range by Eqs. (4)-(5). In Figures 8-9 red symbols represent the measured data and the calculated results are shown with blue lines. It can be seen in the graphs that the distances between the measured and calculated data are small, which are also confirmed by the RMS values in Table 2. The table contains the mean averages as well, which indicate that the parameters are in moderate correlation. Table 3 shows the correlation matrices.

7. CONCLUSIONS

In this paper the authors introduce the rock physical testing system of the Department of Geophysics, University of Miskolc. It consists of a pressure cell with a 2-channel ultrasonic testing device for P and S wave velocity measurements, a load frame allowing uniaxial loading up to 300 kN and a pressure generator for obtaining confining pressure up to 80 MPa. The testing system is controlled by the software DION7, the acoustic wave arrivals are determined with the software GMuG/GL Test Systems PCUSpro. Acoustic P and S wave velocity measurements of two fine-grained sandstone samples were carried out under increasing uniaxial load. It was found that the velocities increase with increasing pressure, and the rate of increase is high at low pressures and levels off at higher pressures. Measured data were processed in a joint inversion procedure based on the developed rock physical model, which describes the pressure dependence of acoustic velocities. The high accuracy of measurement data and the applicability of the model was shown.

8. ACKNOWLEDGEMENTS

The research of Judit Somogyi Molnár and Anett Kiss was carried out in the framework of the Sustainable Resource Management Center of Excellence at the

University of Miskolc, as part of the TÁMOP-4.2.2/A-11/1-KONV-2012-0049 "WELL aHEAD" project in the framework of the New Széchenyi Plan, funded by the European Union, co-financed by the European Social Fund.The research of Mihály Dobróka was supported by OTKA project No. K 109441.

9. LIST OF SYMBOLS

Symbol	Description	Unit
corr(m)	correlation matrix	–
cov(m)	covariance matrix in parameter space	–
RMS	Root Mean Square	%
$d_i^{(c)}$	calculated velocity at the i-th pressure value	m/s
$d_i^{(m)}$	measured velocity at the i-th pressure value	m/s
dv	change of propagation wave velocity	m/s
dV	change in the unit pore volume	m^3
$d\sigma$	stress increase	MPa
M	number of model parameters	–
N	number of measured points	–
$S(\sigma)$	stress sensitivity of velocity-drop	1/MPa
S	mean spread	–
V	pore volume	m^3
v	acoustic wave velocity	m/s
v_0	wave velocity at stress-free state	m/s
v_{max}	wave velocity at maximum pressure	m/s
α	longitudinal (P) wave velocity	m/s
α_0	longitudinal (P) wave velocity at stress-free state	m/s
β	transverse (S) wave velocity	m/s
β_0	transverse (S) wave velocity at stress-free state	m/s
δ	Kronecker-delta symbol	–
Δv	velocity-drop at pressure σ	m/s
Δv_0	velocity-drop at zero pressure	m/s
$\Delta\alpha_0$	longitudinal (P) wave velocity-drop at zero pressure	m/s
$\Delta\beta_0$	transverse (S) wave velocity-drop at zero pressure	m/s
κ	proportionality factor	$1/m^2s$
λ_V	new material quality dependent petrophysical parameter	1/MPa
σ	stress	MPa
σ_{mi}	estimated error of the i-th model parameter	–

10. REFERENCES

[1] BIRCH, F.: The velocity of compression waves in rocks to 10 kilobars, Part 1. *Journal of Geophysics Research*, 1960, 65, 1083–1102.

[2] WALSH, J. B.–BRACE, W. F.: A fracture criterion for brittle anisotropic rock. *Journal of Geophysical Research*, 1964, 69, 3449–3456.

[3] SCHÖN, J. H.: Physical properties of rocks: fundamentals and principles of petrophysics. In: HELBIG, K.–TREITEL, S. (eds): *Handbook of Geophysical Exploration. Seismic exploration.* Pergamon Press, Trowbridge, Volume 18, 1996.

[4] WANG, H.–TODD, T.–WEIDNER, D.–SIMMONS, G.: Elastic properties of Apollo 12 rocks. *Proc. 2nd Lunar Science Conference*, 1971, Vol. 3, 2327–2336.

[5] YU, G.–VOZOFF, K.–DURNEY, D. W.: The influence of confining pressure and water saturation on dynamic elastic properties of some Permian coals. *Geophysics*, 1993, 58 (1), 30–38.

[6] BEST, A. I.: The effect of pressure on ultrasonic velocity and attenuation in near-surface sedimentary rocks. *Geophysical Prospecting*, 1997, 45, 345–364.

[7] WEPFER, W. W.–CHRISTENSEN, N. I.: A seismic velocity-confining pressure relation, with applications. *International Journal of Rock Mechanics and Mining Science*, 1991, 28, 451–456.

[8] WANG, Q.–JI, S. C.–SALISBURY, M. H.–XIA, M. B.–PAN, B.–XU, Z. Q.: Shear wave properties and Poisson's ratios of ultrahigh-pressure metamorphic rocks from the Dabie-Sulu orogenic belt: Implications for the crustal composition. *Journal of Geophysical Research,* 2005, 110, B08208.

[9] SINGH, R.–RAI, C.–SONDERGELD, C.: Pressure dependence of elastic wave velocities in sandstones. *76th International Exposition and Annual Meeting*, SEG, 2006, 1883–1887.

[10] JI, S.–WANG, Q.–MARCOTTE, D.–SALISBURY, M. H.–XU, Z.: P wave velocities, anisotropy and hysteresis in ultrahigh-pressure metamorphic rocks as a function of confining pressure. *Journal of Geophysical Research*, 2007, 112, B09204.

[11] TOKSÖZ, M. N.–JOHNSTON, D. H.–TIMUR, A.: Attenuation of seismic waves in dry and saturated rocks, I. Laboratory measurements. *Geophysics*, 1979, 44 (4), 681–690.

[12] SOMOGYI MOLNÁR, J.–KISS, A.–DOBRÓKA, M.: Petrophysical models to describe the pressure dependence of acoustic wave propagation characteristics. *Acta Geodaetica et Geophysica*, 2014, DOI: 10.1007/s40328-014-0074-4.

[13] DOBRÓKA, M.–SOMOGYI MOLNÁR, J.: New petrophysical model describing the pressure dependence of seismic velocity. *Acta Geophysica*, 2012, 60 (2), 371–383.

[14] MENKE, W.: *Geophysical Data Analysis – Discrete Inverse Theory*. Academic Press, Inc. London Ltd., 1984.

Geosciences and Engineering, Vol. 4, No. 6 (2015), pp. 36–44.

INVERSION APPLICATION IN CARTOGRAPHY: ESTIMATION OF THE PARAMETERS OF THE BEST FITTING CASSINI-PROJECTIONS OF THE FIRST HABSBURG MILITARY SURVEY

GÁBOR MOLNÁR[1]–GÁBOR TIMÁR[2]

[1]*MTA–ELTE Geological, Geophysical and Space Science Research Group*
molnar@sas.elte.hu
[2]*Department of Geophysics and Space Science*

Abstract. Map projection parameters and metadata (location of projection origin, pixel size of the scanned maps) are estimated using classical inversion-based estimation methods for the scanned survey sheets of the First Military Survey (end of 18th century) of the Habsburg Empire. The studied sheets cover five regions of the Empire: historical Hungary, Lower Austria, Bohemia, Croatia and Galicia. The sheets are organized into virtual mosaics according to these regions. For each region, the image coordinates in these mosaics and WGS84 geodetic coordinates from Google Earth are determined for several hundred identified points (ground control points). The map projection was modeled by the Cassini (Cassini-Soldner) projection and their projection equation set.

Using this approximation, the linear fit of the virtual mosaics to the Google Earth base layers was carried out with the same error magnitude (generally a few hundred meters, in extreme cases 2–3 kilometers), which was provided by the quadratic fit using modern coordinate systems. This implies that the Cassini projection is a good mathematical model of these map products. The longitude values of the projection center of the investigated regions are given and the latitude values of the projection centers proved to be arbitrary constants. In the case of Lower Austria, the resulting prime meridian is near the Stephansdom of Vienna, within the mentioned error margin, which indicates that this landmark might have been used for projection origin even in this early cartographic work.

1. INTRODUCTION

1.1. The First Military Survey of the Habsburg Empire

The First Military Survey of the Habsburg Empire was an outstanding geodetic and cartographic project of the second part of the 18th century. Its result is a huge set of 1:28,800 scale manuscript maps, covering the actual territory of the Empire: Austria without its modern western territories, Bohemia, Galicia, historical Hungary with Croatia and Transylvania, as well as the Austrian Netherlands, more or less the present-day Belgium [1] [2] [3].

The survey was carried out on the order of Empress Maria Theresa, issued after the Seven Years War (1750–57). She and her headquarters realized that the Austrian armies needed a high-scale and precise map product for the territories of the empire. In cartographic history, the predecessor of this survey was the one of France, carried out by Cassini and Maraldi [4], slightly earlier than the Austrian work [5]. The scale of the French map system was 1:86,400, so the Austrian survey can be considered to

be the first high-scale military topographic map system, and definitely the first one of the Central European region.

1.2. Georeference of the historical maps

Historical cartographic products have importance as archival documents, carrying information of the time of their creation. In addition, in many cases we can define mathematical relations between their contents and modern map grids. The result of this, a so-called geo-referred map, can be fit to any modern cartographic dataset or map, e.g. to the layers of Google Earth. This way, the original content of the old map can be analyzed also spatially, in any GIS (Geographic Information System) environment [6].

To make a geo-referred map of any old cartographic product, we have to define or estimate its original map projection, and in case of high-scale maps also the geodetic datum (for their detailed description, see [6]). Altogether, these data give the planar coordinate system of the map. Besides this, we have to provide an algorithm to give the coordinates in this system for all pixels of the scanned version of the map. In a GIS environment, a map rectified in a coordinate system defined by the map grid (projection) and the geodetic datum can be converted to any other cartographic coordinate system, especially to the native system of Google Earth.

The fit is regularly marred by some horizontal errors. The main error sources are: errors of the original geodetic survey; inaccurate grid and datum estimation by our process, and drawing errors/generalizations. In the case of the First Military Survey, the errors occurring after ordinary ground control point (GCP) rectification can be up to 1–2 kilometers [7].

1.3. The Cassini-projection as a possible mathematical model of the unknown map grid

According to the literature, there is an agreement that the First Military Survey had no geodetic basis [2]. However, the authors are convinced that the survey could not have been carried out, even with these high errors, without some geodetic background. It is known that there were baseline measurements at the time of the survey in Austria and also in Hungary [8]. Joseph Liesganig, who led these operations, was also the coordinator of the First Survey works in Galicia [9]. The determination of astronomical position, which is the very basis of any geodetic survey, was at quite a high level, even in determining the longitude differences between far prime meridians, e.g. those of Paris, Vienna, Greenwich and Ingolstadt, by special methods [10]. The lack of documentation of a geodetic survey in the Austrian archives is not evidence in itself. Even we could not accomplish this survey without some geodetic background, with the technology of the 18th century, with such relatively high global accuracy.

If we assume the existence of some (unknown) geodetic basis, an important question is what was the map projection of the resulting sheets. In short, the map projection is the function set between the geographical (latitude, longitude) and the

map planar coordinates. According to the literature, the survey sheets have no projection, their system is ‘projectionless’.

However, for a georeference method, we need at least some assumption of the map projection type. An obvious selection is the Cassini-projection [11], the method used for the map of France [12] [13]. We must emphasize that we do not state that the projection of the First Military Survey is exactly the Cassini-projection – we simply use this projection as a mathematical model of their native grid.

1.4. The goal of this study

In this study, we collect a set of ground control points (GCPs) in order to derive the optimum projection parameters – the parameter set that provides the minimum horizontal difference between the points’ real and computed position in modern systems. Here the word ‘computed’ refers to the method of the georeference, coordinates computed from the object positions in the map grid, in practice in the scanned image matrix. Our study contains two important regions of the former Habsburg Empire: Lower Austria (with Vienna) and Hungary. The estimation of these projection parameters is only the first step in the accurate georeferencing of these survey sheets [14]; however it falls within the scope of this volume: in the field of inversion methods.

2. THE PROCESSED DATASET

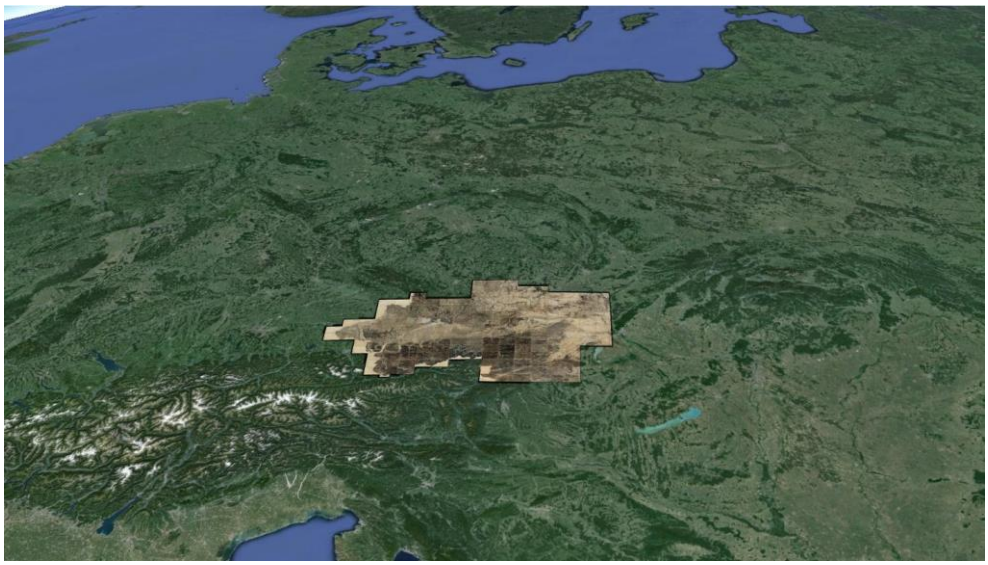

Figure 1
The mosaic of the Lower Austrian sheets of the First Military Survey
on the Google Earth geolayer: the target area of the present study

We used several hundred GCPs from the investigated regions, with an average density of 2–3 points per map sheet, or in other words, cca. one point per 100 km^2. For each point, the following data items are given:

- Geodetic coordinates in the WGS84 system, read from Google Earth, and
- Cartesian (planar) coordinates in the map mosaic grid.

To obtain the Cartesian coordinates, a virtual map mosaic was constructed for the map sheets belonging to each investigated region (Figure 1). Thus, the origins of these planar systems were taken at the upper left (north-western) corner of these mosaics.

We considered these planar coordinate systems as Cassini-type projected ones, with still unknown map projection parameters. The Cassini-projection has four compulsory parameters to be defined in any cartographic applications: the geodetic coordinates of the projection center in the base ellipsoid (a longitude and a latitude; two values) and the coordinates of the projection center in the projected plane (two length data in meters). Using this input data set, we planned to estimate the following parameters:

- the pixel size of the scanned map sheet images;
- the Cassini-coordinates of the origins (NW corner of the mosaics) and
- location of the map projection in the WGS84 system.

In this approach, the projection center's planar coordinates are set to zero in both directions and the mosaic is placed into this plane by the coordinates of the NW corner. With the above data, the virtual map mosaic can be geo-referred – the location of each pixel is given, thus the old map can be placed into a modern geodetic reference system, or, more practically, shown as a correctly placed overlay in the Google Earth environment, for popular publications.

3. METHOD: THE ESTIMATION OF THE PROJECTION PARAMETERS

To estimate the above-listed parameters, we shall start from the direct projection equations of the Cassini projection [11]:

$$\begin{aligned} x &= R \cdot \arcsin\left(\cos\Phi \cdot \sin\left(\lambda - \lambda_0\right)\right) \\ y &= R \cdot \left[\arctan\left[\tan\Phi / \cos\left(\lambda - \lambda_0\right)\right] - \Phi_0\right] \end{aligned} \tag{1}$$

where R is the radius of Earth, Φ and λ are latitude and longitude of the point, Φ_0 and λ_0 are the latitude and longitude of the center of the projection, x and y are the Cartesian coordinates of the projected point.

The usual approach of the inversion for parameter estimating is to provide a series of equations expressing the partial derivatives of Eq. (1), with respect to the parameters to be estimated ([15]; for more practical considerations cf. e.g. [16] [17] [18]). In the present case we could apply numerical derivatives instead of the analytical derivatives. However, in practice these parameters can be divided into two groups. According to the definition of the Cassini-projection, the only real

independent parameter here is the longitude of the projection origin. The latitude of the projection origin and the south-northern location of the map plane together show total equivalency in the parameter estimation. Practically, this latitude value was set intentionally to around the mid-latitude of the investigated regions. All of the other parameters are expressed from the above ones, while the only independent parameter – the origin's longitude – was estimated by a single one-dimensional iteration.

4. RESULTS

Our results are considered to be of two kinds:

- the accuracy of the fitting of the map mosaic to the modern coordinate systems, and
- the longitude values of the projection origins of some First Military Survey regions.

The accuracy is considerably worse than that of the Second Military Survey [19]. In our case, the maximum displacements are up to 2.4 kilometers for Lower Austria and even more (up to 3 kilometers) in historical Hungary. This implies that a further refinement of the geo-reference is still needed for more exact scientific analyses; we refer to this in the last section of this paper. The displacement vectors for the Lower Austrian mosaic are shown in Figure 2.

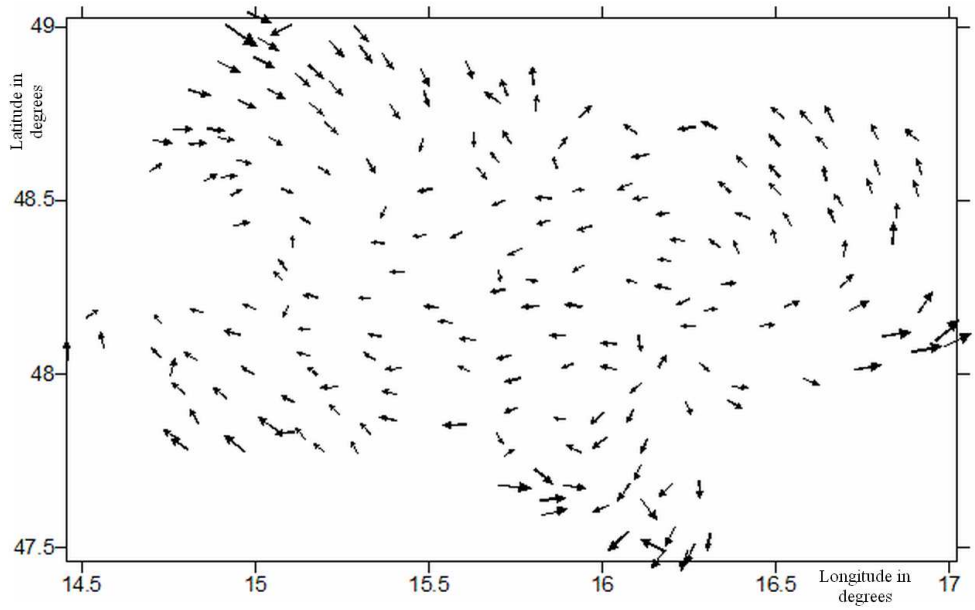

Figure 2
The remaining error vectors after using the best fitting Cassini-projections for the Lower Austrian mosaic, as a mathematical model of the horizontal control of the historical map mosaic

The longitude of the above-mentioned two regions, are quite interesting. In the case of Hungary, it is slightly east of Pest (a part of present-day Budapest), where we could not find any important landmark, either in modern maps or in the processed historical map sheet mosaic. The resulting longitude (19.29 degrees from Greenwich) runs within the mentioned error margin from the present-day geodetic observatory of Penc, which is a mere co-incidence.

The resulting central longitude for Lower Austria (16.35 degrees from Greenwich), however, interestingly enough, cuts into the downtown of the capital city, Vienna. It runs near the Schottentor at the western end of the historical city, just around 800 meters west of the most obvious landmark of the city, the Stephansdom.

In the case of Croatia the orientation of the map sheets is far from the normal 'north up' convention; the meridian convergence exceeds 10 degrees. Even this region can be geo-referred using the estimation of the longitude of projection origin. In this case, this theoretical central longitude does not cross the region but runs far (cca. 20 degrees) east of it. The central meridians of all investigated regions are shown in Table 1.

Table 1

Longitudes of the best fitting Cassini-projection origins in the investigated regions

Hungary	**Lower Austria**	**Bohemia**	**Croatia**	**Galicia**
19.29	16.35	18.79	37.36	39.19

5. DISCUSSION

The accuracy of the mosaic fitting to the modern coordinate systems has to be compared to the horizontal control of the previous georeferencing attempts of the First Military Survey sheets. These are published by Arcanum (2006), using the estimation of the 10 parameters of a simple quadratic polynomial connection between modern (UTM) coordinates and image pixel coordinates on virtual mosaics at identical GCPs. It is important to underline that the original map sheets could not be mapped in the UTM coordinate system, as it was defined almost 200 years later. The horizontal error of this quadratic fitting is of the very same order as that of the linear fitting to the best-fitting Cassini-projection. This is a good indication that the First Military Survey has a Cassini-projection.

The case of Lower Austria is even more convincing. According to the parameter estimation, the projection origin falls in the downtown of Vienna, and we can use the Stephansdom as a projection center with the same accuracy (with a small shift in the east-west location of the mosaic corner point). This is a useful contribution to the debate about the existence of geodetic network behind the First Military System.

6. CONCLUSIONS AND FURTHER REFINEMENT POSSIBILITIES

We suggest that the First Military Survey had a well-defined geodetic background, even if the connected geodetic point list has not yet been found in the archives. The Cassini-projection with the above-mentioned meridians provides an acceptable

mathematical model for the geo-referencing of Hungary and Lower Austria (the investigated regions). The model reproduces the modern coordinates of the scanned pixels with an error of up to 2.4 and 3 kilometers.

A further correction step (which is not discussed here, as it does not concern the topic of inversion methods) can be compiled using local correction grids, based on the same input point list and the parameter estimation results [20] (Figure 3).

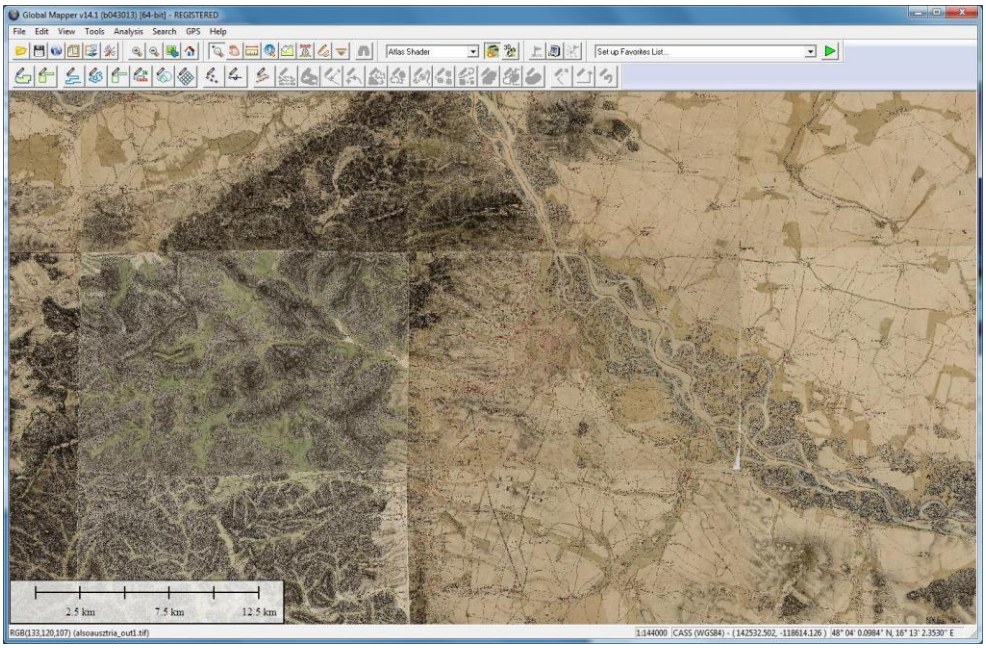

Figure 3
The originally linear boundaries of the rectangular map sheets are slightly distorted by the correction grid refinement in order to achieve better horizontal fit

7. LIST OF SYMBOLS

Symbol	Description	Unit
R	is the radius of Earth,	km
λ	longitude of the point	°
λ_0	longitude of the center of the projection	°
Φ	latitude of the point	°
Φ_0	latitude of the center of the projection	°
x, y	Cartesian coordinates of the projected point	m

8. ACKNOWLEDGEMENTS

The authors are grateful to Arcanum Database Ltd. (Budapest) and its managers, Sándor and Előd Biszak, for the frames of this study, and also to the

ÖsterreichischesStaatsarchiv (Kriegsarchiv) and personally to Hannes Kulovits and all cooperating partners of the Mapire initiative.

9. REFERENCES

[1] HOFSTÄTTER, E.: *Beiträge zur Geschichte der österreichischen Landesaufnahmen, I. Teil*. Bundesamt für Eich- und Vermessungwesen, Wien, 1990.

[2] KRETSCHMER, I.–DÖRFLINGER, J.–WAWRIK, F.: *Austrian cartography (in German)*. Wiener Schriften zur Geographie und Kartographie, 2004, Band 15. Institut für Geographie und Regionalforschung der Universität Wien.

[3] JANKÓ, A.: *Military surveys of Hungary 1763–1950 (in Hungarian)*. Argumentum, Budapest, 2007.

[4] CASSINI, C. F.–MARALDI, G. D.: *Nouvelle carte qui comprend les principaux triangles qui servent de fondement a la description géometrique de la France. Levée par Ordre du Roi.* Aubin & Heulland, Paris, 1744.

[5] TIMÁR, G.–MÉSZÁROS, J.–MOLNÁR, G.: A simple solution for georeferencing the Cassini map series of France. *9th International Workshop on Digital Approaches to Cartographic Heritage*, Budapest, 2014.

[6] TIMÁR, G.–MOLNÁR, G.: *Map grids and datums*. University handout. Eötvös Loránd University, Budapest, 2013, 84.

[7] MOLNÁR, G.: Making a georeferenced mosaic of historical map series using constrained polynomial fit. *Acta Geodaetica et Geophysica Hungarica*, 2010, 45 (1), 24–30.

[8] LIESGANIG, J.: *Dimensio graduum meridiani viennensis et hungarici*. A Bernardi, Wien, 1770, 264.

[9] SEEGEL, S.: *Mapping Europe's borderlands: Russian cartography in the age of Empire*. University of Chicago Press, 2012, 384.

[10] HELL, M.: *Observatio Transitus Veneris Ante Discum Solis Die 3. Junii Anno 1769 Wardoëhusii. Giese*, Hafniae (Copenhagen), 1770, 82.

[11] SNYDER, J. P: *Map projections – a working manual*. USGS Professional Papers, 1987, 1395.

[12] COSTES, B.–GROSSO, E.–PLUMEJEAUD, C.: *Géoreferencement et appariement de donnés issues des cartes du Cassini: Intégration dans un réferentiel topographique actuel*. SAGEO, Liège, Belgium, 2012.

[13] HERRAULT, P. A.–SHEEREN, D.–FAUVEL, M.–MONTEIL, C.–PAEGELOW, M.: A comparative study of geometric transformation models for the historical 'Map of France' registration. *Geographia Technica*, 2013, 8 (1), 34–46.

[14] MOLNÁR, G.–TIMÁR, G.–BISZAK, E.: Can the First Military Survey maps of the Habsburg Empire (1763–1790) be georeferenced by an accuracy of 200 meters? *9th International Workshop on Digital Approaches to Cartographic Heritage*, Budapest, 2014.

[15] MOLNÁR, G.: *Geophysical Inversion (in Hungarian)*. University handout, Eötvös Loránd University, Budapest, 2013, 118.

[16] SZABÓ, N.: Global inversion of well log data. *Geophysical Transactions*, 2004, 44 (3-4), 313–329.
[17] DOBRÓKA, M.–SZABÓ, N.: Interval inversion of well-logging data for objective determination of textural parameters. *Acta Geophysica*, 2011, 59 (5), 907–934.
[18] DOBRÓKA, M.–SZABÓ, N.: Interval inversion of well-logging data for automatic determination of formation boundaries by using a float-encoded genetic algorithm. *Journal of Petroleum Science and Engineering*, 2012, 86–87, 144-152.
[19] TIMÁR, G.–MOLNÁR, G.–SZÉKELY, B.–BISZAK, S.–VARGA, J.–JANKÓ, *A.: Historical maps of the Habsburg Empire – The map sheets of the Second Military Survey and their georeferenced version*. Arcanum, Budapest, 2006, 57.
[20] MOLNÁR, G.–TIMÁR, G.: Using of Grid Shift Binary (GSB) data to improve the geo-reference of the Third Military Survey of the Habsburg Empire. *Geophysical Research Abstracts*, 2011, 13, 11861.

Geosciences and Engineering, Vol. 4, No. 6 (2015), pp. 45–71.

HYDROGEOPHYSICAL CHARACTERIZATION OF GROUNDWATER FORMATIONS BASED ON WELL LOGS: CASE STUDY ON CENOZOIC CLASTIC AQUIFERS IN EAST HUNGARY

NORBERT PÉTER SZABÓ[1, 2]–ANETT KISS[1]–ANETT HALMÁGYI[1]

[1]*Department of Geophysics, University of Miskolc*
[2]*MTA-ME Geoengineering Research Group, University of Miskolc*
norbert.szabo.phd@gmail.com

Abstract. Ground geophysical surveys can be effectively used for detecting and delineating shallow groundwater structures. For calculating the freshwater reserves, well-logging measurements need to be made in prospecting wells. In this paper, groundwater formations are evaluated using electric and nuclear logging data to extract the petrophysical and hydraulic parameters of aquifers and aquitards. To quantify the relative fractions of rock constituents, the effective porosity, shale content, water saturation and rock-matrix volumes should be estimated. The effective layer-thicknesses of permeable beds are of importance in locating the depth-intervals of water exploitation. The above parameters cannot be calculated reliably when the zone parameters such as cementation exponent, tortuosity factor, pore-water density and resistivity are not certain. With accurate petrophysical and zone parameters, an estimate can be given to hydraulic conductivity, which is one of the most important hydraulic rock properties in solving hydrogeophysical problems. First, a comprehensive interpretation method proposed by Professor János Csókás (1918–2000), former head of the Department of Geophysics, University of Miskolc, is used to give an estimate of hydraulic conductivity and critical velocity of flow without the need for grain-size data. Then, shale volume and hydraulic conductivity are determined by statistical factor analysis of well logs. Effective porosity, specific surface of grains and water saturation can be derived by well-known deterministic equations. Those of core measurements confirm the results of well log analysis. A set of detailed regression analyses is performed to specify the local regression relationships between the estimated parameters. It is also shown that there is a strong correlation between shale volume and hydraulic conductivity (and other quantities) and that the independent interpretation results are consistent. The advantage of the Csókás and factor analysis-based approaches is that instead of using a single well log, they utilize all types of well logs sensitive to the relevant petrophysical/hydraulic parameters for a more reliable hydrogeophysical characterization of aquifers.

1. INTRODUCTION

Well-logging methods are widely used in the reconnaissance of mineral and hydrocarbon resources, as they provide detailed in-situ information about the geometrical and petrophysical parameters of geological structures [1]. They are applicable also for the investigation of shallow formations, for instance, in water prospecting and solving environmental and engineering geophysical problems [2]. The main task encountered by well log analysts when solving hydrogeophysical problems is to estimate the layer thickness, effective porosity, and water (sometimes

air) saturation, amount of shaliness, matrix volumes hydraulic conductivity of unconsolidated beds as accurately as possible. Some petrophysical properties can be given with relatively high accuracy, for instance porosity is normally estimated with an error of 1–2 p.u. depending on the uncertainty of measured data. At the same time, the estimation error of hydraulic conductivity can reach an order of magnitude, thus, well logs can be primarily applied to detect only the variation of hydraulic conductivity along a borehole or between neighboring boreholes. Suitable borehole geophysical methods for estimating hydrogeophysical parameters with related applications are detailed in [3].

Almost all types of well-logging suites used in hydrocarbon exploration can be implemented in groundwater prospecting. Natural gamma-ray intensity and spontaneous potential logs are applied for lithology identification and layer-thickness determination. The former measures the natural radioactivity of formations caused by different amounts of potassium, thorium and uranium content. The latter records the electric potential difference between a surface and a downhole electrode excited by the ion movement between the drilling mud and original pore fluid as well as the presence of shale. Both of them can be used to predict shale content quantitatively. For porosity determination, nuclear well logs such as formation density and neutron porosity are used. Bulk density observed by gamma-gamma probes shows a strong inverse proportionality to porosity. Neutron-neutron measurements are mainly sensitive to the hydrogen index of formations and allow us to infer the total porosity in the absence of hydrogen atoms in the rock matrix. Several types of resistivity tools with different depth of investigation and vertical resolution can be applied to detect the invasion profile and to estimate water saturation in different zones around the borehole. Since freshwater has higher resistivity than brine, traditional (non-focused) resistivity probes are generally suitable for groundwater exploration. While shallow resistivity tools measure the apparent resistivity of the zone invaded by mud, the deep resistivity instrument observes the same quantity in the original (non-invaded) formation. The resistivity readings are corrected to predict the true resistivity of groundwater formations, which is of great importance in calculating water saturation in aquifers. Well-logging methods usually encompass also technical measurements that are not used directly in the petrophysical characterization of rocks, but that give important information on the technical conditions of the borehole wall and its environment, pressure, temperature, flow rate and composition of the original pore fluid along the borehole.

In addition to conventional well-logging techniques, there is a possibility for using advanced tools in the evaluation of aquifers. In oilfield applications, the direct determination of permeability as a related quantity is possible by means of the nuclear magnetic resonance log. The ground geophysical application of this technique, known as magnetic resonance sounding, is an emerging method in hydrogeology. Borehole nuclear resonance magnetism has been lately adapted from the oilfield for hydrogeological applications, using boreholes typical of environmental and hydrogeological investigations [4]. Although nuclear magnetic resonance is a very expensive method, it has the added advantage of not only

providing free-fluid porosity, it can also be used to determine the distribution of pore sizes and fluid characteristics to provide a better estimate of the hydraulic properties of rocks.

The petrophysical parameters can be calculated by deterministic, inverse or statistical modeling procedures. The most common deterministic approaches are based on the individual analysis of well logs. Estimation that is more reliable can be given by using several well logs simultaneously. In this study, two advanced well-logging methodologies are discussed and compared to each other. In shallow clastic sediments, the evaluation of petrophysical and hydraulic parameters generally requires the preliminary knowledge of grain sizes and several fluid parameters. In the absence of direct geophysical measurements, one is confined to measuring some related physical parameters or taking rock samples from the borehole to extend hydrogeological information to a local area. In order to avoid core sampling, CSÓKÁS [5] worked out a comprehensive interpretation method to give an estimate of the hydraulic conductivity of unconsolidated freshwater-bearing formations based solely on well-logging data. By incorporating the field experiments of ALGER [6], Hazen's effective grain-size can be substituted by Archie's formation factor, which can be measured directly from well logs. The derived formula, including porosity and true resistivity of aquifers, gives a continuous estimate of hydraulic conductivity for the entire length of a borehole. In addition, the Csókás method comprises the determination of critical velocity of flow, which can be used to estimate the highest value of sand-free yield from the technical data of the filtering surface.

Factor analysis is traditionally used to reduce the dimensionality of multivariate statistical problems [7]. Technically, it is possible to decompose a data matrix of observed physical quantities of any dimension to a matrix of fewer statistical variables. This is called an exploratory statistical method, because it allows us to extract information on latent variables not directly measurable by well-logging probes. In this study, factor analysis is used to reveal correlation relations between well-logging data and petrophysical/hydraulic parameters of aquifers. An earlier study of hydrocarbon wells showed a non-linear relationship between one of the new variables derived by factor analysis and shale volume, which proved to be nearly independent of the measurement area [8].

A Hungarian feasibility study is presented in this paper. The multivariate statistical method applied to the investigated water well finds a similarly strong regression relation between the statistical factor and shale volume (and hydraulic conductivity) as a key parameter in the prediction of exploitable reserves of aquifers. Those of core measurements validate the interpretation results obtained independently by the Csókás-method and factor analysis. In addition, regression relations and correlation coefficients between petrophysical/hydraulic parameters are given for the area of Baktalórántháza, East Hungary. It is shown that there is a strong correlation between shale volume and hydraulic conductivity (and other quantities). The independent interpretation results are consistent. The advantage of the presented approaches is that instead of using a single well log they process simultaneously all suitable well logs sensitive to the relevant petrophysical

parameters in order to support groundwater exploration with reliable petrophysical/hydrogeological information.

2. CONVENTIONAL FORMATION EVALUATION

Darcy's equation is one of the basic relationships of hydrogeology to describe the flow of water through a porous formation

$$\frac{\partial \mathbf{u}}{\partial t} = -\frac{\kappa}{\Phi \mu} \nabla p \quad , \tag{1}$$

where κ (m^2) denotes rock permeability, Φ (volume/volume = v/v) is formation porosity, μ (Ns/m^2) is dynamic viscosity, **u** (m) is the relative displacement vector of the fluid and p (N/m^2) is the pore pressure. Hydraulic conductivity $k = \kappa^* \rho_w^* g/\mu$ (m/s) as a related quantity expresses the ease with which the water flows through the pore spaces. Quantity k is influenced by several properties of the rock matrix and pore fluid of primary porosity aquifers such as viscosity and density of pore-fluid (ρ_w in g/cm^3), grain-size distribution, porosity, and water saturation (S_w in v/v).

The Kozeny–Carman-equation has achieved widespread use as a standard model for estimating hydraulic conductivity of aquifers. In theory, the rock with primary porosity is treated as an assembly of capillary channels, which satisfies the Navier–Stokes-equation. The following form of the Kozeny–Carman-equation is one of the most widely used models for the estimation of hydraulic conductivity [9]

$$k = \frac{\rho_w g}{\mu} \frac{d^2}{180} \frac{\Phi^3}{(1-\Phi)^2} \quad , \tag{2}$$

where d (cm) is the dominant grain diameter and g (cm/s^2) is the normal acceleration of gravity (k is given in units of cm/s). Since rock samples can be taken from boreholes, the dominant grain diameter can be estimated from the grain-size distribution curve [10]

$$d = \frac{d_{10} + d_{60}}{2} \left(\frac{d_{10}}{d_{60}} \right)^{1/2} \quad , \tag{3}$$

where d_{10} (cm) and d_{60} (cm) are the grain diameters at 10% and 60% cumulative frequencies, respectively. The dominant grain size in Eq. (3) can be defined as the diameter of a homo-disperse conglomerate of grains, the surface of which equals that of the real sample with actual grain-size distribution and the same density. The effective porosity of shaly sandy beds fully saturated with freshwater ($S_w = 1$) can be

derived from well logs, for instance from gamma-gamma measurements by neglecting the term of air saturation

$$\Phi = \frac{\rho_{sd} + V_{sh}\left(\rho_{sh} - \rho_{sd}\right) - \rho_b^{(m)}}{\rho_{sd} - 1}, \tag{4}$$

where $\rho_b^{(m)}$ (g/cm^3) is the bulk density measured and ρ_{sd} and ρ_{sh} denote the density of sand and shale components, respectively. The amount of shaliness appearing in Eq. (4) can be estimated by the following empirical formula generally used in young sedimentary formations [11]

$$V_{sh} = 0.083\left[2^{3.7\left(\frac{GR - GR_{\min}}{GR_{\max} - GR_{\min}}\right)} - 1\right], \tag{5}$$

where GR (cps) is the measured natural gamma-ray intensity and GR_{min} and GR_{max} are the extreme values of the gamma-ray log in the groundwater zone. Equation (5) does not depend on the water type, but caution should be used in rocks including radioactive non-clay minerals or fractures filled with uranium- or thorium-rich water. The correlation between grain size and porosity should be revealed before well logs are applied to calculate the continuous curve of hydraulic conductivity.

In more advanced approaches, several well logs are processed together in one interpretation procedure. If the number of unknowns equals to that of the observed logs the modeling functions are treated as a set of linear equations, which can be solved graphically or numerically. If we measure more data types than unknowns some inversion method is generally used to extract petrophysical parameters. In the evaluation of domestic aquifers normally natural gamma-ray intensity (GR in cpm), spontaneous potential (SP in mV), neutron-neutron intensity (NN in kcpm), bulk density (ρ_b in g/cm^3), shallow and deep resistivity (R_s and R_d in ohmm) logs are recorded. The petrophysical parameters can be related to well-logging data by means of empirical modeling equations. These mathematical relations, called probe response equations, can be used to predict data in a forward modeling procedure. The values of theoretical data would be measured along the borehole if the geological structure were characterized by the assumed (exactly known) model parameters. In general, borehole geophysical data can be expressed as a set of nonlinear equations including the physical properties of rock matrix and fluid components weighted by the relative volumes of rock constituents. The following set of response functions can be used for the solution of the forward problem in fully saturated shaly sandy aquifers [12]

$$SP = SP_{sh}V_{sh} - C \cdot \lg\frac{R_{mf}}{R_w}\left(1 - V_{sh}\right), \tag{6}$$

$$GR = GR_{sd} + \frac{1}{\rho_b}\left(V_{sh} GR_{sh} \rho_{sh} + V_{sd} GR_{sd} \rho_{sd}\right), \tag{7}$$

$$\rho_b = \Phi \rho_{mf} + V_{sh} \rho_{sh} + V_{sd} \rho_{sd}, \tag{8}$$

$$NN = \Phi NN_f + V_{sh} NN_{sh} + V_{sd} NN_{sd}, \tag{9}$$

$$R_s = \left[\left(\frac{V_{sh}^{(1-0.5\,V_{sh})}}{R_{sh}^{1/2}} + \frac{\Phi^{m/2}}{\left(aR_{mf}\right)^{1/2}}\right)\right]^{-2}, \tag{10}$$

$$R_d = \left[\left(\frac{V_{sh}^{(1-0.5\,V_{sh})}}{R_{sh}^{1/2}} + \frac{\Phi^{m/2}}{\left(aR_{w}\right)^{1/2}}\right)\right]^{-2}, \tag{11}$$

$$\Phi + V_{sh} + V_{sd} = 1, \tag{12}$$

where V_{sd} (v/v) is the volume of sand and R_{mf}, R_w and R_{sh} (ohmm) denote the resistivity of mud filtrate, pore-water and shale, respectively. In Eqs. (6)−(11), there are some model parameters that do not vary (or vary just slowly) with depth, called zone parameters, which are practically kept constant during the forward modeling procedure. Zone parameters with subscripts *sh*, *sd*, *mf*, *w* refer to physical properties of shale, sand, mud-filtrate and water, respectively, whereas constants *m*, *n*, *a* represent the textural properties of rocks given from literature or empirical techniques. The definition, including the measurement unit of petrophysical and zone parameters, can be found in the section of list of symbols. Equation (12) is the material balance equation for the rock environment, which is used to specify the relative fractions of rock constituents per unit volume of rock and constrain the domain of volumetric parameters in the interpretation procedure. In inverse modeling, the model parameters (i.e. porosity, water saturation, shale content and matrix volume) are estimated simultaneously. Inversion procedures have the added advantage of also giving the estimation errors of petrophysical parameters, which characterize quantitatively the accuracy and reliability of inversion results. The hydraulic conductivity can be derived from the inversion results by using proper empirical equations [13]. The methodology of inverse modeling and some shallow examples can be found in DRAHOS [14] and SZABÓ and DOBRÓKA [15].

3. THE CSÓKÁS-METHOD

CSÓKÁS [5] worked out a comprehensive interpretation methodology to extract petrophysical and hydraulic parameters of aquifers solely from well logs. The Csókás model is an empirically modified form of Eq. (2) applicable in shallow formations, based on the relation between the effective grain size and formation

factor of freshwater-bearing unconsolidated sediments. The method gives a continuous estimate of hydraulic conductivity along a borehole by using electric and nuclear logging measurements without the need for grain-size data. In fully saturated aquifers the formation factor (F) is defined as the ratio of the resistivity of rock (R_0 in ohmm) to that of the pore-water

$$F = \frac{R_0}{R_w}. \tag{13}$$

ALGER [6] found a direct proportionality between the formation factor and grain size of freshwater saturated sediments in the laboratory that is the opposite of that experienced in hydrocarbon fields (i.e. in brine-saturated reservoirs). Based on these observations, Hazen's effective grain diameter (d_{10}) determined from sieve analysis was related to the formation factor of unconsolidated sediments

$$d_{10} = C_d \lg F, \tag{14}$$

where $C_d = 5.22 \cdot 10^{-4}$ was proposed for not too poorly sorted sediments with a formation factor less than 10. This requirement is normally met in shallow clastic aquifers. An interpretation methodology to evaluate freshwater-bearing (shaly) sands based on Eq. (14) was proposed by ALGER [6] for different types of well-logging suites adapted from the oilfield. Equation (14), as a constraint relation, forms the bridge between well-logging measurements and hydraulic conductivity of aquifers. The dominant grain size can be given from the grain-size distribution curve. The uniformity coefficient $U = d_{60}/d_{10}$ acts as a shape parameter which characterizes the form of the grain-size distribution curve and quantifies the degree of uniformity in a granular material. KOVÁCS [16] connected the uniformity coefficient of sands to the dominant grain diameter as $d/d_{10} = 1.919 \cdot \lg U + 1$. For poorly sorted sediments ($U > 5$), quantity U is inversely proportional to the logarithm of hydraulic conductivity. For not so badly sorted sands ($2.0 \leq U \leq 2.5$) the previous equation takes the form $d = 1.671 \cdot d_{10}$, with which Eq. (14) modifies to

$$d = 1.671 \cdot C_d \lg \frac{R_0}{R_w}. \tag{15}$$

ARCHIE [17] suggested an empirical formula developed from laboratory measurements made on numerous samples

$$F = a \Phi^{-m}, \tag{16}$$

where m is the cementation exponent (in poorly compacted sediments m~1.5−1.7) and a is the tortuosity coefficient (a~1). The study of ALGER [6] showed that the formation factor not only depends on porosity, but also on the resistivity of pore water and grain size in freshwater saturated sediments with primary porosity. Dispersed clay particles can considerably modify the resistivity of pore water, which then affects the value of the formation factor appearing in Eq. (15). OGBE and BASSIOUNI [18] coupled the tortuosity factor with porosity and formation factor

$$a^2 = \left(\frac{R_0}{R_w} \Phi \right)^{1.2} . \tag{17}$$

To find an estimate to hydraulic conductivity from well logs, Eq. (2) should be properly modified [16]

$$k = \frac{1}{5} \frac{g}{\upsilon} \frac{\Phi^3}{(1-\Phi)^2} \left(\frac{d}{\alpha_0} \right)^2 , \tag{18}$$

where α_0 is the average shape factor of sample particles in the range of 7 and 11 for sands (the average is 10). The kinematic viscosity of water $\upsilon = \mu / \rho_w$ (m^2/s) can be expressed in the function of formation temperature. The ratio of gravity acceleration and kinematic viscosity for water is $g/\upsilon = 5.517 \cdot 10^4 \cdot C_t$ (m^{-1}s^{-1}), where C_t is a temperature dependent coefficient calculated as $C_t = 1+3.37 \cdot 10^{-2}T+2.21 \cdot 10^{-4}T^2$ (where T is given in units of °C). PIRSON [19] published another form of the Kozeny equation used to predict permeability

$$k = \frac{1}{5} \frac{g}{\upsilon} \frac{\Phi^3}{(1-\Phi)^2} \left(\frac{1}{a \cdot S} \right)^2 , \tag{19}$$

where S (1/m) denotes the specific surface of the rock. By comparing Eqs. (18)−(19) the following identical equation is derived

$$\left(\frac{d}{\alpha_0} \right)^2 = \left(\frac{1}{a \cdot S} \right)^2 . \tag{20}$$

GÁLFI and LIEBE [20] summarized several empirical relations between the specific electric resistance and hydraulic conductivity for sands and gravels. In freshwater aquifers, the electric current is hardly conducted through the spaces between the grains, rather mainly on the surfaces of particles. Thus, the resistivity is inversely proportional to the specific surface of rock grains. By assuming that the

sedimentary rock is composed of spherical particles the specific surface can be calculated as

$$S = 6\frac{(1-\Phi)}{d} \quad . \tag{21}$$

The combination of Eqs. (15) and (21) gives

$$S^2 = \frac{36(1-\Phi)^2}{\left(1.671 \cdot C_d \cdot \lg\frac{R_0}{R_w}\right)^2} \quad . \tag{22}$$

The Csókás-model based on Eqs. (17), (18), (20), (22) can give an estimate to hydraulic conductivity in units of m/s

$$k = C_k \frac{\Phi^3}{(1-\Phi)^4} \frac{\left(\lg\frac{R_0}{R_w}\right)^2}{\left(\frac{R_0}{R_w}\Phi\right)^{1.2}} \quad , \tag{23}$$

where $C_k = 855.7 \cdot C_t C_d{}^2$ is a proportionality constant. Good aquifers are characterized by hydraulic conductivities k (m/s) $> 10^{-6}$, while aquitards are indicated by k (m/s) $< 3 \cdot 10^{-8}$. The uniqueness of the Csókás-formula resides in the fact that all parameters in Eq. (23) can be derived from well logs, and thus therewith a continuous (in-situ) estimate can be given for hydraulic conductivity along a borehole.

The Csókás-method gives further possibilities for the hydraulic characterization of aquifers. Tangential stresses are developed at the surfaces of rock grains because of the water flow. The critical velocity of flow at which the grains of size d_{10} are made to move to the direction of the borehole can be estimated from hydraulic conductivity [21]

$$v_c \approx 2(d_{10})^{1/2} \approx 0.067(k)^{1/2} \quad , \tag{24}$$

where v_c and k are both given in m/s, while d_{10} is given in mm. For maintaining a sand-free exploitation process, the above information can be used for setting an optimal pumping rate. Above the critical velocity, there is a risk that the water becomes of worse quality or sand grains invade the well. The volume capacity of the well in m^3/s can be calculated as

$$Q_{max} = 2\pi r_0 h_0 v_c , \tag{25}$$

where r_0 (m) is the radius of filter pack and h_0 (m) is its length. Well-site experience shows that significantly higher velocities can be applied than suggested in Eq. (24). Consequently, a higher value of water discharge can be produced than that of Q_{max}. From grain-size analysis a more realistic estimate to critical velocity was suggested by KASSAI and JAMBRIK [22]

$$v_c = 10^{0.446\lg(d)+0.1654-3} , \tag{26}$$

where v_c is measured in m/s, d is given in mm. Equation (26) gives a good approximation in the range of 0.09−5 mm dominant grain sizes. By combining Eqs. (25)−(26), the optimal water discharge can be estimated by

$$Q_{max} = 2\pi \cdot 10^{-3} \cdot r_0 h_0 \left(10^{0.446\lg(d)+0.1654}\right) , \tag{27}$$

which is multiplied by $6 \cdot 10^4$ to obtain the output in the unit of l/min. The Csókás-procedure is tested and compared to statistical factor analysis using well-logging data collected in Baktalórántháza, East-Hungary (Section 5).

4. EXPLORATORY FACTOR ANALYSIS

The multivariate statistical procedure is applicable to transform numerous geophysical data types into smaller number of variables called factors. As a result, a few factors explain the determinant amount of total variance of measurement data, which can be connected to petrophysical/hydraulic properties of the investigated geological structure. In the first step, well logs are standardized

$$d_{ln}^{(obs)'} = \frac{\left(d_{ln}^{(obs)} - \overline{d}_l^{(obs)}\right)}{\sqrt{\frac{1}{N-1}\sum_{n=l}^{N}\left(d_{ln}^{(obs)} - \overline{d}_l^{(obs)}\right)^2}} , \tag{28}$$

where $d_{ln}^{(obs)'}$ denotes the n-th scaled data of the l-th observed well log, $\overline{d}_l^{(obs)}$ is the average value of raw data of the l-th well log (L is the number of borehole geophysical tools and N is the number of measuring points in the processed depth-interval). All standardized data are gathered into data matrix **D'**, which is decomposed by the model of factor analysis as

$$\mathbf{D}' = \mathbf{F}\mathbf{W}^{\mathrm{T}} + \mathbf{E} , \tag{29}$$

where **F** denotes the *N*-by-*M* matrix of factor scores, **W** is the *L*-by-*M* matrix of factor loadings, **E** is the *N*-by-*L* matrix of residuals, *M* is the number of extracted factors (T indicates the operator of matrix transpose). The observed variables are developed as the linear combination of factors. The scores of the first factor as the elements in the first column of matrix **F** give the well log of the first factor, which explains the largest part of variance of the well-logging data. Other subsequent factors represent a relatively lower portion of variances. The individual weights of each data type associated with the factors are given in the matrix of factor loadings **W**, which measures the degree of correlation between the factors and original data, respectively. Since the factors are assumed linearly independent $\left(\mathbf{F}^{\mathrm{T}}\mathbf{F}/N=\mathbf{I}\right)$, the correlation matrix of the standardized well-logging data is

$$\mathbf{R}=\frac{1}{N}\mathbf{D}'^{\mathrm{T}}\mathbf{D}'=\frac{1}{N}\left(\mathbf{F}\mathbf{W}^{\mathrm{T}}\right)^{\mathrm{T}}\left(\mathbf{F}\mathbf{W}^{\mathrm{T}}\right)+\mathbf{E}^{2}=\mathbf{W}\mathbf{W}^{\mathrm{T}}+\mathbf{\Psi}, \tag{30}$$

where $\mathbf{\Psi}$ is the diagonal matrix of specific variances (**I** is the identity matrix). The diagonal elements of matrix **R** are equal to unity and are added up by the variances of the standardized observed variables. If one neglects the term $\mathbf{\Psi}$ in Eq. (30) the following reduced correlation matrix is introduced

$$\mathbf{R}^{*}=\mathbf{W}\mathbf{W}^{\mathrm{T}}=\mathbf{R}-\mathbf{\Psi}=\begin{pmatrix} h_1^2 & r_{12} & \cdots & r_{1L} \\ r_{12} & h_2^2 & \cdots & r_{2L} \\ \cdots & \cdots & \cdots & \cdots \\ r_{1L} & r_{2L} & \cdots & h_L^2 \end{pmatrix}, \tag{31}$$

where the *i*-th element in the main diagonal represents the communality defined as

$$h_i^2=\sum_{l=1}^{L}W_{il}^2\le 1. \tag{32}$$

From Eq. (31) it follows that matrix $\mathbf{\Psi}$ represents the part of variance of the observations that are not explained by the common factors, which is calculated in the knowledge of communalities

$$\mathbf{\Psi}=\mathbf{I}-\mathbf{H}^{2}. \tag{33}$$

If the elements of the *L*-by-*L* matrix of communalities ($\mathbf{H}^2$) are much smaller than unity, the observed variables can hardly be explained with the common factors.

Otherwise, the information of original variables can be represented well by some factors.

The factor loadings should be estimated first, to which three types of solutions are normally applied. In case of $\mathbf{\Psi} = \mathbf{0}$ the problem reduces to the solution of an eigenvalue problem, which is equivalent to Principal Component Analysis (PCA). In this approximation the reduced correlation matrix $\mathbf{R}^*$ is decomposed as

$$\mathbf{W}\mathbf{W}^{\mathrm{T}} = \mathbf{Z}\,\mathbf{\Lambda}\,\mathbf{Z}^{\mathrm{T}}, \tag{34}$$

where $\mathbf{Z}$ is the L-by-M matrix of eigenvectors, $\mathbf{\Lambda}$ is the M-by-M diagonal matrix of eigenvalues. From Eq. (34) the matrix of factor loadings is

$$\mathbf{W} = \mathbf{Z}\mathbf{\Lambda}^{1/2}, \tag{35}$$

where the matrix element $\Lambda_{ll}^{1/2} = \lambda_l^{1/2}$ is computed by the l-th eigenvalue. Since the covariance matrix of observed variables (i.e. correlation matrix of standardized data) contains the data variances in its main diagonal, the factors can be classified by the eigenvalues ($\lambda_1 \geq \lambda_2 \geq ... \geq \lambda_M \geq 0$). The direction of the largest data variance is indicated by the eigenvector corresponding to the largest eigenvalue, which is called the first principal direction (first factor). The second largest eigenvalue and its vector represent the second principal direction (second factor), which is perpendicular to the first one etc. The factor scores are calculated from factor loadings and measured data. PCA ignores matrix $\mathbf{E}$ in Eq. (30), which allows for the unique solution of a set of linear equations. For instance, consider five different types of well logs (*GR*, *SP*, *NN, DEN, RD*) represented by standardized data at six different depth levels ($L = 5$, $N = 6$). Factor analysis gives an estimate to two uncorrelated factors

$$\begin{pmatrix} F_{11} & F_{12} \\ F_{21} & F_{22} \\ F_{31} & F_{32} \\ F_{41} & F_{42} \\ F_{51} & F_{52} \\ F_{61} & F_{62} \end{pmatrix} = \begin{pmatrix} GR_{11} & SP_{12} & NN_{13} & DEN_{14} & RD_{15} \\ GR_{21} & SP_{22} & NN_{23} & DEN_{24} & RD_{25} \\ GR_{31} & SP_{32} & NN_{33} & DEN_{34} & RD_{35} \\ GR_{41} & SP_{42} & NN_{43} & DEN_{44} & RD_{45} \\ GR_{51} & SP_{52} & NN_{53} & DEN_{54} & RD_{55} \\ GR_{61} & SP_{62} & NN_{63} & DEN_{64} & RD_{65} \end{pmatrix} \begin{pmatrix} W_{11} & W_{12} \\ W_{21} & W_{22} \\ W_{31} & W_{32} \\ W_{41} & W_{42} \\ W_{51} & W_{52} \end{pmatrix}, \tag{36}$$

where F_{nm} represents the score of the m-th factor at the n-th depth, L_{lm} is the load of the l-th observed variable put on the m-th factor. The drawback of the above method is that the portion of data variance unexplained by the factors is neglected, thus, the resultant principle components do not represent the total variance of measured data.

With the second approach the matrices **W** and $\boldsymbol{\Psi}$ are estimated in a simultaneous optimization procedure. JÖRESKOG [23] suggested the minimization of the following objective function

$$\Omega(\mathbf{W},\boldsymbol{\Psi}) = \mathrm{tr}\left(\mathbf{R} - \mathbf{W}\mathbf{W}^{\mathrm{T}} - \boldsymbol{\Psi}\right)^2 = \min . \tag{37}$$

For solving the optimization problem the use of the maximum likelihood method is generally applied, which can give a robust solution [24]. The third alternative for estimating the factor loadings is the use of a non-iterative approximate algorithm [23]. At first the following matrix is calculated

$$\mathbf{S}^* = \left(\mathrm{diag}\mathbf{S}^{-1}\right)^{1/2}\mathbf{S}\left(\mathrm{diag}\mathbf{S}^{-1}\right)^{1/2}, \tag{38}$$

where **S** denotes the sample covariance matrix of the standardized data. The eigenvalues λ and eigenvectors $\boldsymbol{\omega}$ of matrix $\mathbf{S}^*$ should be computed before the matrix of factor loadings is given

$$\mathbf{W} = \left(\mathrm{diag}\mathbf{S}^{-1}\right)^{-1/2}\boldsymbol{\Omega}\left(\boldsymbol{\Gamma} - \theta\,\mathbf{I}\right)^{-1/2}\mathbf{U}, \tag{39}$$

where $\boldsymbol{\Gamma}$ is the diagonal matrix of the first M number of sorted eigenvalues, $\boldsymbol{\Omega}$ is a matrix of the first M number of eigenvectors, **U** is an arbitrary M-by-M orthogonal matrix. Parameter θ in Eq. (39) specifies the smallest number of factors when

$$\theta = \frac{1}{L - M}\left(\lambda_{M+1} + \lambda_{M+2} + \square + \lambda_L\right) < 1 . \tag{40}$$

Assuming that **W** and $\boldsymbol{\Psi}$ are known quantities, the well logs of factor scores can be extracted by the maximization of the following log-likelihood function

$$\lg(P) = -\frac{1}{2}\left[\lg|2\pi\,\boldsymbol{\Psi}| + \left(\mathbf{D}' - \mathbf{F}\mathbf{W}^{\mathrm{T}}\right)\boldsymbol{\Psi}^{-1}\left(\mathbf{D}' - \mathbf{F}\mathbf{W}^{\mathrm{T}}\right)^{\mathrm{T}}\right] = \max . \tag{41}$$

After solving Eq. (40) an unbiased estimate to factor scores can be given by the hypothesis of linearity [25]

$$\mathbf{F}^{\mathrm{T}} = \left(\mathbf{W}^{\mathrm{T}}\boldsymbol{\Psi}^{-1}\mathbf{W}\right)^{-1}\mathbf{W}^{\mathrm{T}}\boldsymbol{\Psi}^{-1}\mathbf{D}'^{\mathrm{T}} . \tag{42}$$

The optimal number of factors can be set by statistical tests [26] or by Eq. (40) according to Jöreskog's approximate algorithm. The resultant factors are usually

rotated for an easier interpretation. Since factor loadings are defined non-uniquely, an orthogonal transformation $\mathbf{W}\mathbf{W}^{\mathrm{T}} = \mathbf{W}^{*}\mathbf{W}^{*\mathrm{T}}$ can be applied to factor loadings, where $\mathbf{W}^{*} = \mathbf{W}\mathbf{V}$ holds for a suitably chosen *M*-by-*M* orthogonal matrix **V**. In this study, the *Varimax* algorithm suggested by KAISER [27] is used to generate rotated factors, which are directly compared to petrophysical/hydraulic parameters of aquifers by regression analysis. Singular value decomposition of matrix $\mathbf{R}^{*}$ gives the proportions of total variance explained by each factor

$$\mathbf{R}^{*} = \mathbf{U}\mathbf{S}_{e}\mathbf{V}^{\mathrm{T}}, \tag{43}$$

where **U** and **V** are *L*-by-*L* orthogonal matrices and $\mathbf{S}_{\mathrm{e}}$ is a diagonal matrix including the positive singular values sorted in descending order. The proportions of singular values estimate the information represented by the factors. The total variance is given by the trace of matrix $\mathbf{S}_{\mathrm{e}}$. The variance explained by the *q*-th factor is

$$\sigma_{q} = \frac{S_{e,qq}}{\mathrm{tr}(\mathbf{S}_{e})} \cdot 100\ (\%) \,. \tag{44}$$

Regression tests are performed to reveal the relations between the factors and petrophysical/hydraulic properties of rocks. In this study, the shale volume and hydraulic conductivity are estimated from the simultaneous processing of well logs. Earlier studies showed an exponential relation between the first factor and shale volume [8]. Hydraulic conductivity as a related quantity also correlates with the same statistical variable. In Section 5, the factor-analysis-based interpretation procedure is tested and compared to the Csókás-method in the Baktalórántháza well site. The quality of interpretation results are checked by numerical analysis. The degree of linear dependence between the petrophysical variables is measured by the classical Pearson's correlation coefficient (*R*). In case of nonlinear relationships, the Spearman's (rank) correlation coefficient characterizes better the strength of correlation

$$\rho = 1 - \frac{6\sum_{n=1}^{N}\delta_{n}^{2}}{N(N^{2}-1)}, \tag{45}$$

where δ_n is the difference between the ranks of the *n*-th data of the two investigated variables. When the value of the above correlation coefficient is nearly unity, a close (nonlinear) relationship is shown. The deviation between the well logs of petrophysical or hydraulic quantities is characterized by the Root-Mean-Square (*RMS*) error normalized to the relevant parameter.

5. CASE STUDY

The Csókás-method and factor analysis are tested in Well Baktalórátháza-1 located in Szabolcs-Szatmár-Bereg County, in North-East Hungary. The original aim of the ground geophysical surveys was the investigation of the geological structure for the purpose of hydrocarbon exploration. Although neither oil nor gas was found, the borehole was still suitable for producing thermal water. According to VES soundings the upper 80−100 m part of the well was drilled through Pleistocene sediments dominated by sands, in which only the variation of grain sizes was detectable by geoelectric methods. A well-logging survey was conducted to provide information on deeper formations. Borehole logs indicated that the underlying rock of the sandy sequence was shale. Between 100−160 m sands had been deposited, followed by a shaly formation, and 5−15 m thick coarse-grained beds could be found. The boundary of Pleistocene and Pannonian periods was detected at the depth of 240 m. The Pannonian shaly complex mainly consisted of clayey sand, some gravel, clayey silt, clayey marl and bituminous clay.

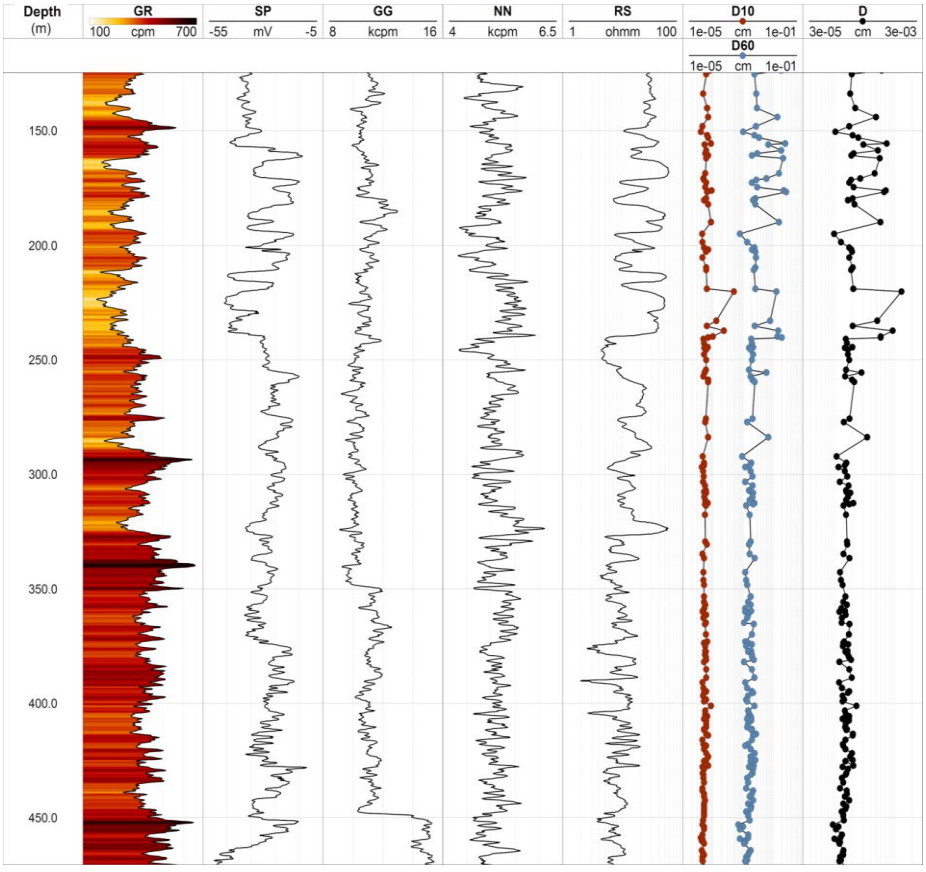

Figure 1
Observed well logs and grain-size data in Baktalórántháza-1

The investigated interval for the present study is between 124.6−470.5 m, where the pore spaces of sediments are fully saturated with freshwater. The available well logs, such as natural gamma-ray intensity (*GR*), spontaneous potential (*SP*), gamma-gamma (*GG*) and neutron-neutron (*NN*) and shallow resistivity (*RS*) are plotted in Figure 1. Grain-size data are also provided from laboratory measurements made on 176 core specimens. The values of d_{10} and d_{60} are derived from the grain-size distribution curves, while the dominant grain size (d) was calculated from Eq. (3). The grain size data are plotted with dots in the last two tracks in Figure 1.

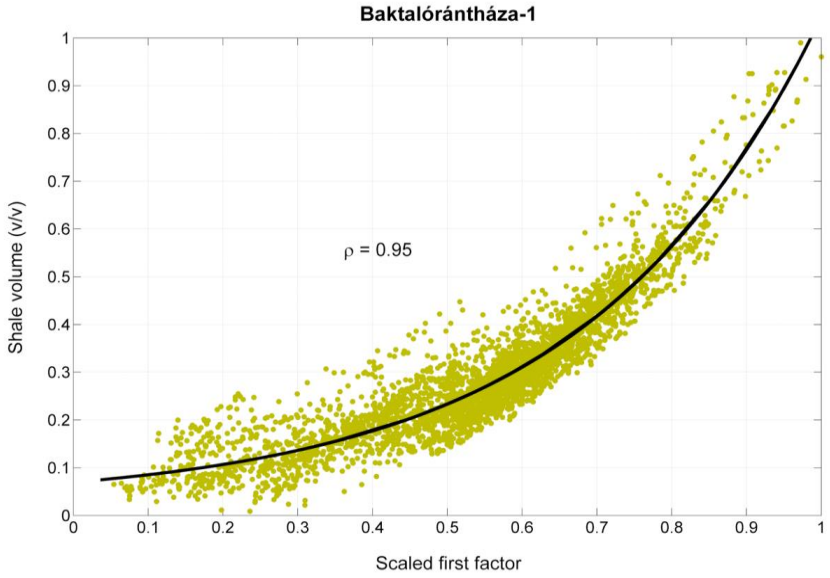

Figure 2
Regression relation between the first factor and shale volume in Baktalórántháza-1

First, the result of factor analysis is presented. The factor loadings and scores are estimated by the solution of Eqs. (37) and (42). Singular value decomposition of the data covariance matrix shows that the total variance of input data can be explained by two lithological factors. The first factor is responsible for 82% of data variance, while the second factor explains 18% of observed information. The greatest loads go to the resistivity and natural gamma-ray logs: −0.77 (*RS*), 0.80 (*GR*). The average correlation between the measured variables is weak (R = 0.16), where the highest coefficient is indicated between the resistivity and natural gamma-ray log (R = 0.62). The information of these two well logs is culminated mainly in the first factor. For comparing the results of different interpretation methods, the scores of the first factor are scaled into the interval of 0 and 1. Regression tests show that the exponential relation between the first factor and shale volume suggested earlier by SZABÓ [8] is valid in the area of Baktalórántháza (Figure 2). The general formula between the first scaled factor (F_1') and shale volume calculated by Eq. (5) is

$$V_{sh} = \alpha e^{\beta F_1'} + \gamma, \tag{46}$$

where the local regression coefficients are given with 95% confidence bounds: $\alpha = 0.0412$ [0.0373, 0.0452], $\beta = 3.204$ [3.102, 3.306], $\gamma = 0.0285$ [0.0196, 0.0374]. The rank correlation coefficient ($\rho = 0.95$) shows a strong correlation between the statistical variable and the shale content (the linear correlation is also strong at $R = 0.88$).

Hydraulic conductivity as a quantity related to shale volume can be directly derived by factor analysis of well-logging data. The first statistical factor can be compared to the values of hydraulic conductivity calculated by the Kozeny–Carman-model using dominant grain-sizes measured on the core samples and porosity by Eq. (2). The neutron-neutron readings are used to calculate the total porosity by using Eq. (9), where the constants of the response function of the neutron probe can be read from the *NN*−*GG* crossplot ($NN_{sh} = 4$ kcpm, $NN_{sd} = 7.5$ kcpm, $NN_f = 1$ kcpm). The general regression model is

$$\lg(K) = c_1 F_1' + c_2, \tag{47}$$

where K is the dimensionless hydraulic conductivity ($K = k/k_0$, where $k_0 = 1$ cm/s), c_1 and c_2 are site specific constants estimated with 95 % level of significance as $c_1 = -4.353$ [−4.956, −3.75], $c_2 = -3.46$ [−3.795, −3.125]. The Pearson's correlation coefficient ($R = -0.74$) shows a strong inverse proportionality between the first scaled factor and the decimal logarithm of hydraulic conductivity (Figure 3).

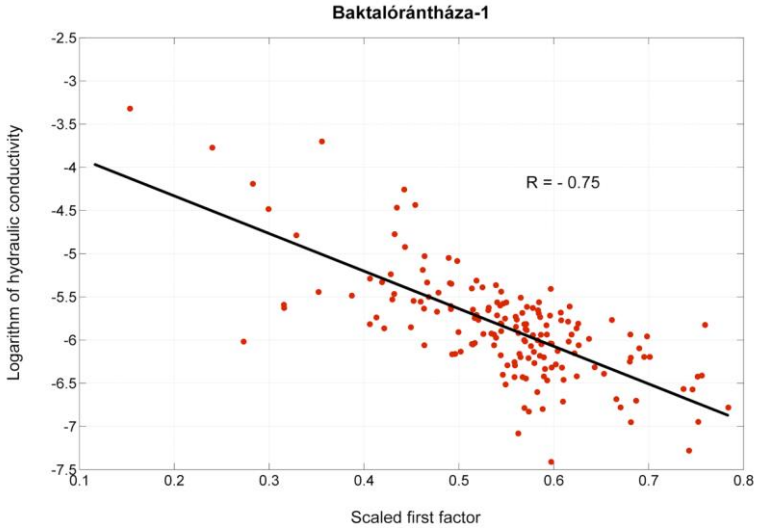

Figure 3
Regression relation between the first factor and hydraulic conductivity in Baktalórántháza-1

The use of the Csókás-method requires the preliminary knowledge of effective porosity and the formation factor. The effective porosity and sand volume can be calculated from neutron (total) porosity and shale volume by Eq. (12). The amount of shaliness can be calculated by factor analysis or independently by using Eq. (5), where the natural gamma-ray intensities of sands and shales are derived from the deflections of the gamma-ray log (GR_{min} = 188 cpm, GR_{max} = 685 cpm). The formation factor is normally derived from *SP* and R_0 logs. In the lack of some related quantities, the Humble formula is used to calculate the formation factor ($F = 0.62/\Phi^{2.15}$). With the formation factor and porosity, the Csókás-method based on Eq. (23) gives an estimate of hydraulic conductivity without having to use grain-size data along the entire length of the borehole. Equation (2) is applied to validate the resultant hydraulic conductivity log, where the dynamic viscosity is set to 0.019 Pa·s and the acceleration of gravity is 981 cm/s^2. Since the Kozeny–Carman-model cannot discard the measurement of grain sizes, the hydraulic conductivity is estimated only to that depth level where rock samples have been previously taken from the borehole. The numerical results show that the result of the Csókás-method is in close agreement with that of the Kozeny–Carman-procedure, because the *RMS* error is 3.4% averaged for the places of recovered rock samples. The hydraulic conductivity estimated by multivariate factor analysis fits acceptably to that of the Csókás-procedure, where the *RMS* is 8.8% for the processed interval. The estimation results of the Csókás' formula and factor analysis are represented in Figure 4. The critical velocity of water flow (VC_CS) can be derived from the hydraulic conductivity log (k_CS) by Eq. (24), moreover an estimate can be given for the specific surface of grains by Eq. (21). The latter is applicable to separate permeable and impervious intervals, i.e. aquifers appear at lower values of specific surfaces, while aquitards are represented by suddenly increased values of the interpolated well log of quantity S. The results of factor analysis are also included in the figure. Shale volume (VSH_FA) estimated by Eq. (46) is in track 4, which shows a close agreement with core data (VSH_CORE). The well log of VSH_LAR represents the shale volume based on the Larionov-formula. Hydraulic conductivity estimated by factor analysis (k_FA) is validated by core derived hydraulic conductivity data (k_CORE). Both methods gives acceptable estimates, although perhaps factor analysis works better in the higher range of hydraulic conductivities (e.g. in the aquifer at the depth 225−240 m). The volumetric rock composition is illustrated in the last track in the figure for reference.

A comparative study is made between the interpretation results of independent well log analyses. Figure 5 shows a strong linear correlation between the shale volumes estimated by the Larionov-formula, factor and core analyses. The regression functions including the expected values of regression coefficients and their estimation errors are listed in Table 1. The correlation between the results of Larionov-method and core analysis is somewhat weaker than that between results of factor and core analyses. The *RMS* error between the factor and core analyses also shows some 4% relative decrease.

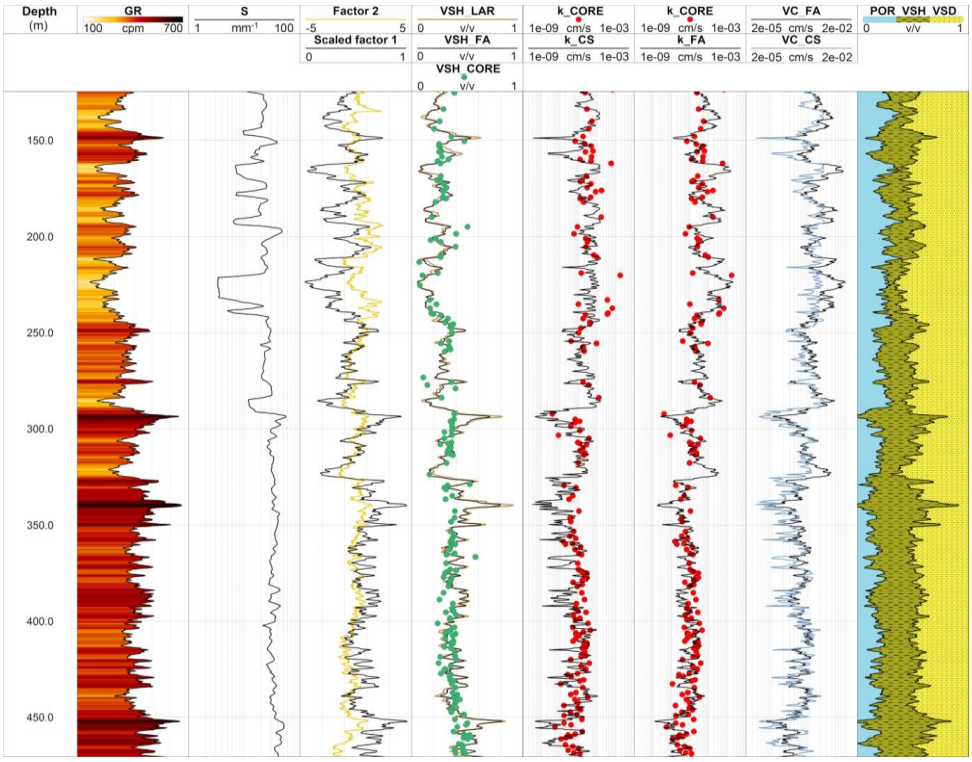

Figure 4
Well logs of estimated petrophysical and hydraulic parameters
in Baktalórántháza-1

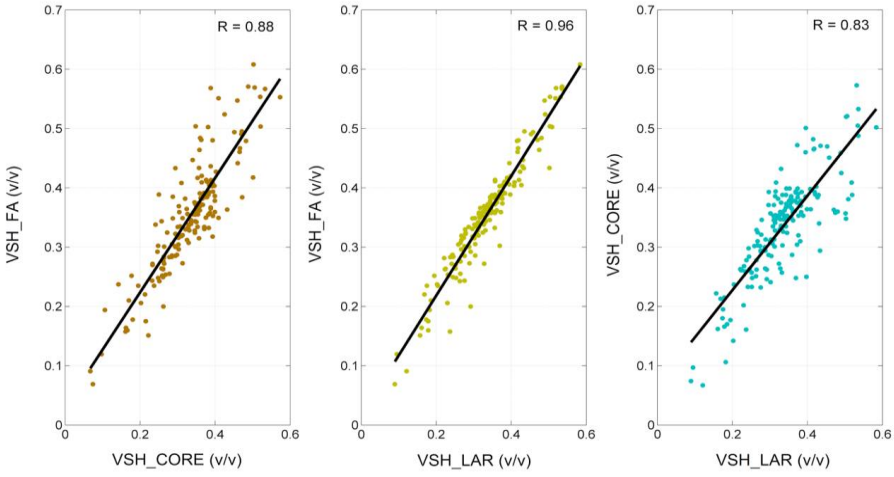

Figure 5
Regression relations between shale volumes estimated from different sources
in Baktalórántháza-1

The Csókás formula-derived hydraulic conductivity log can also be compared to the result of factor analysis in the entire logging interval (Figure 6). The hydraulic conductivity estimated by multivariate factor analysis fits acceptably to that of the Csókás procedure, where the correlation coefficient is $R = 0.79$ and the *RMS* error is 5.3%. In the places of core sampling the correlation coefficient between the Csókás- and Kozeny–Carman model-based hydraulic conductivity is $R = 0.75$, while it is $R = 0.74$ between the results of factor and core analyses. Even so, the *RMS* errors in Table 1 show that the factor analysis-derived hydraulic conductivities are closer to those of core measurements. This seems to be caused by the larger discrepancies between the Csókás- and Kozeny–Carman-methods compared to factor analysis and Kozeny–Carman-procedure in the higher range of hydraulic conductivities.

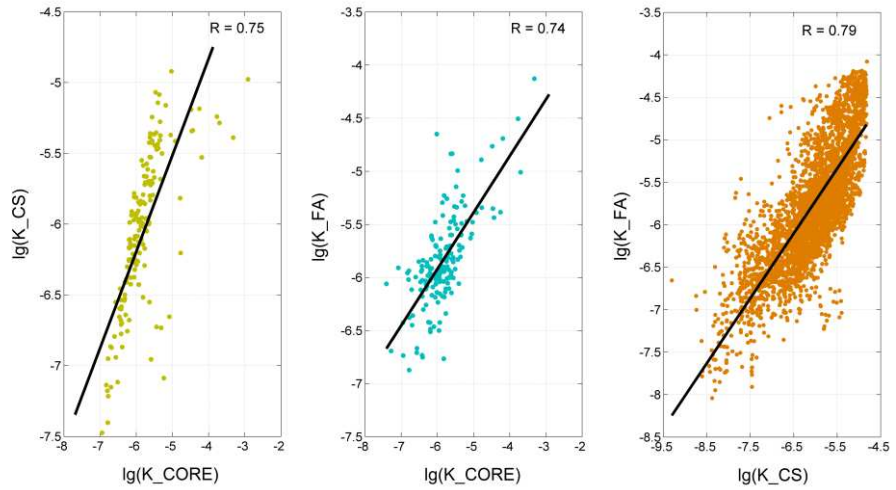

Figure 6
Regression relations between hydraulic conductivity estimation results in Baktalórántháza-1

The regression connections between different petrophysical/hydraulic quantities are examined below. It is found that there is a slight nonlinear relation between the shale volume and hydraulic conductivity, both estimated by factor analysis. The suggested regression function is

$$\lg\left(K^{(\mathrm{FA})}\right) = c_1^* \left(V_{sh}^{(\mathrm{FA})}\right)^{c_2^*} + c_3^*, \tag{48}$$

where the regression coefficients are obtained with 95 % level of confidence: $c_1^* = -6.168$ [−6.264, −6.072], $c_2^* = -2.148$ [−2.27, −2.026], $c_3^* = 0.4849$ [0.467, 0.5028]. The rank correlation coefficient ($\rho = -0.97$) shows a strong correlation between the above variables. The strength of correlation between shale volume estimated by the Larionov formula and factor analysis-based hydraulic conductivity is also strong

($\rho = -0.94$); this can be approximated also by Eq. (48). The regression coefficients are modified a little as $c_1^* = -6.339$ [−6.556, −6.122], $c_2^* = -1.696$ [−1.947, −1.446], $c_3^* = 0.398$ [0.3719, 0.424]. Both regression functions can be seen in Figure 7. Other linear regression relations between shale volume and hydraulic conductivity are listed in Table 1, where the independent estimation results agree with each other. In Figure 8, the specific surface calculated by Eq. (21) can be compared to porosity, and dimensionless hydraulic conductivity and critical velocity of flow, whose linear connections are quantified in Table 1.

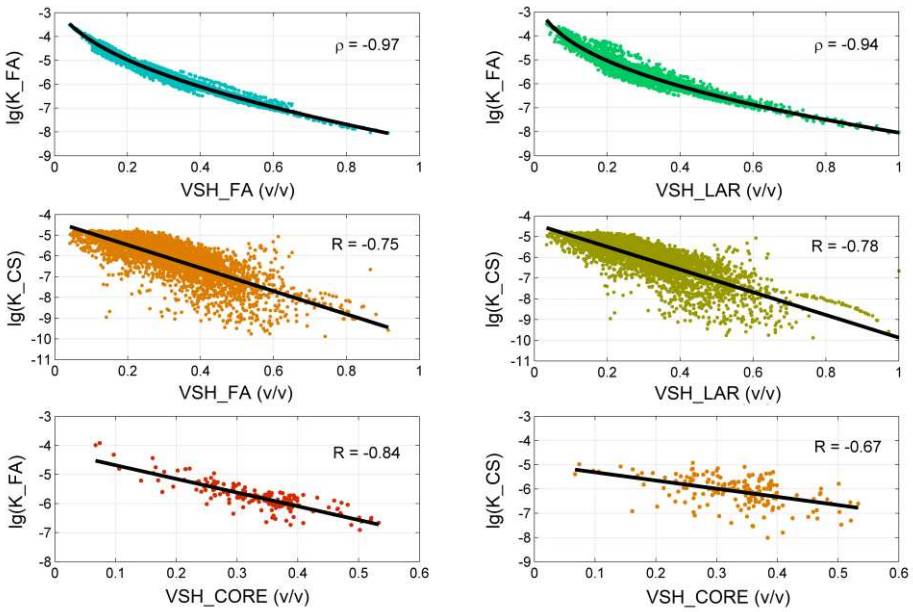

Figure 7
Regression relations between shale volume and hydraulic conductivity in Baktalórántháza-1

Table 1
Regression relations between petrophysical/hydraulic parameters of groundwater formations estimated from different methods in Baktalórántháza-1

Regression function	a_{min}	a	a_{max}	b_{min}	b	b_{max}	RMS	R
$V_{sh}^{(FA)} = aV_{sh}^{(CORE)} + b$	0.8875	0.9657	1.044	0.0038	0.0307	0.0577	4.89%	0.88
$V_{sh}^{(FA)} = aV_{sh}^{(LAR)} + b$	0.9669	1.010	1.053	0.0018	0.0165	0.0313	3.25%	0.96
$V_{sh}^{(CORE)} = aV_{sh}^{(LAR)} + b$	0.7177	0.7964	0.8752	0.0411	0.0683	0.0955	5.08%	0.83
$\lg K^{(CS)} = a \lg K^{(CORE)} + b$	0.5886	0.6811	0.7735	–2.65	–2.107	–1.564	6.10%	0.75
$\lg K^{(FA)} = a \lg K^{(CORE)} + b$	0.4587	0.5322	0.6057	–3.158	–2.726	–2.294	5.82%	0.74
$\lg K^{(FA)} = a \lg K^{(CS)} + b$	0.7432	0.7632	0.7833	–1.26	–1.139	–1.018	5.31%	0.79

Regression function	amin	a	amax	bmin	b	bmax	RMS	R
$\lg K^{(CS)} = aV_{sh}^{(FA)} + b$	–5.733	–5.567	–5.401	–4.413	–4.355	–4.297	–	-0.75
$\lg K^{(CS)} = aV_{sh}^{(LAR)} + b$	–5.627	–5.482	–5.337	–4.443	–4.392	–4.341	–	-0.78
$\lg K^{(FA)} = aV_{sh}^{(CORE)} + b$	–5.122	–4.676	–4.229	–4.373	–4.219	–4.065	–	-0.84
$\lg K^{(CS)} = aV_{sh}^{(CORE)} + b$	–4.313	–3.371	–2.428	–5.297	–4.974	–4.651	–	-0.67
$V_{sh}^{(FA)} = aS^{(CS)} + b$	$8 \cdot 10^{-4}$	$9 \cdot 10^{-4}$	$9 \cdot 10^{-4}$	6.884	7.697	8.51	–	0.74
$\lg K^{(FA)} = aS^{(CS)} + b$	$-5 \cdot 10^{-5}$	$-5 \cdot 10^{-5}$	$-5 \cdot 10^{-5}$	–4.36	–4.313	–4.267	–	-0.73
$\Phi^{(NN)} = aS^{(CS)} + b$	$-4 \cdot 10^{-6}$	$-4 \cdot 10^{-6}$	$-4 \cdot 10^{-6}$	0.3063	0.3123	0.3183	–	-0.58
$\lg v_c^{(FA)} = aS^{(CS)} + b$	$-2 \cdot 10^{-5}$	$-2 \cdot 10^{-5}$	$-2 \cdot 10^{-5}$	–2.356	–2.333	–2.309	–	-0.73

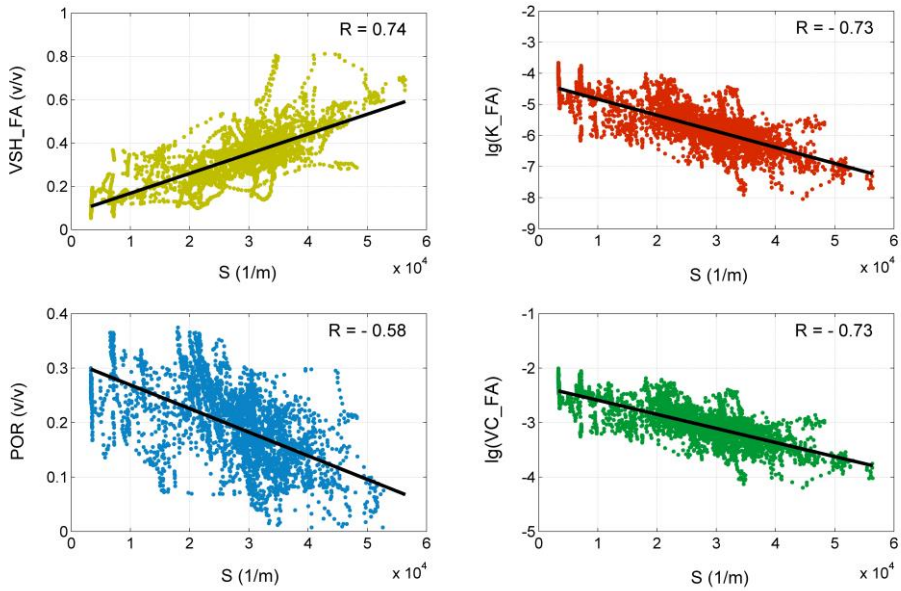

Figure 8
Regression relations between specific surface and petrophysical/hydraulic quantities in Baktalórántháza-1

6. CONCLUSIONS

The feasibility of the Csókás-method and statistical factor analysis have been demonstrated in a shallow hydrogeological environment. Both methods using only well-logging information give a continuous (in-situ) estimate of petrophysical/hydraulic parameters in the form of well logs. The Csókás-method is applicable to estimate hydraulic conductivity, critical velocity of flow, and specific surface of grains in typical unconsolidated aquifers, which are of high importance in

extending the information of aquifer tests. The interpretation results are confirmed by the Kozeny–Carman-procedure using core measurements. Factor analysis of the same well logs gives a reliable estimate of the amount of shaliness and hydraulic conductivity. The independent estimation for shaliness helps us to refine the lithology of formations and improve the aquifer storage model. Factor analysis uses all available well logs sensitive to lithology and water content (including caliper and temperature logs that cannot be used in inverse modeling without probe response functions), integrated into one statistical procedure to maximize the accuracy and reliability of the interpretation results. The petrophysical/hydrogeophysical information can be given also to a larger investigation area by using a special factor analysis algorithm extended to multidimensional model geometries.

The comparative regression study shows that the results of factor analysis are close to that of core analysis. Factor analysis uses five types of well logs and larger statistical sample in a joint statistical procedure for the estimation of hydraulic conductivity in Baktalórántháza-1. On the contrary, the Csókás-method utilizes two types (i.e. resistivity and porosity logs) in estimating the relevant parameter. The Csókás-method can give an estimate to a larger number of petrophysical/hydraulic parameters, which are connected to well-logging data deterministically. Factor analysis has been tested earlier in deep-seated (hydrocarbon-bearing) structures, while the Csókás-formula was developed specifically for shallow sediments. According to field experience, an optimal solution can be obtained with the Csókás-procedure in medium or coarse-grained (well-sorted) unconsolidated sediments with a formation factor of less than 10. In the case of highly cemented aquifers, the estimation results show considerable deviations from the Kozeny–Carman-model. Also in very fine-grained rocks, the hydraulic conductivities show sometimes a difference of more than one order of magnitude, which may require the revision of the Alger formula. Taking one thing with another, the independent estimation results agree with each other, which is proven by the regression connections revealed at the well site. The well-logging techniques presented in this paper is hereby recommended to the community of hydrogeophysicists; the techniques can be complemented with new types of measurements or advanced techniques used for the observation of input parameters to increase the efficiency of the evaluation of groundwater formations.

7. ACKNOWLEDGEMENTS

The author as the leading researcher of OTKA project No. PD-109408 thanks the support of the Hungarian Scientific Research Fund as well as to the support of the János Bolyai Research Fellowship of the Hungarian Academy of Sciences. The authors thank Professor Mihály Dobróka and László Hursán, honorary associate professor, for their valuable scientific advice, and László Bucsi Szabó of the Háromkő Deposit Company and Béla Latrán of Geokomplex Ltd. for professional consultation on well-site applications.

8. LIST OF SYMBOLS

Symbol	Description	Unit
a	Tortuosity factor in Archie's equation	–
c_1, c_2	Regression coefficients for K vs. F'_1 relation	–
c_1^*, c_2^*, c_3^*	Regression coefficients for K vs. V_{sh} relation	–
C	Temperature coefficient for calculating SP response	–
C_d	Regression coefficient for d_{10} vs. F relation	–
C_t	Temperature coefficient of ratio g/υ	–
d, D	Dominant grain size	m
d_{10}, D10	Hazen's effective grain diameter	m
d_{60}, D60	Grain diameter derived from the grain-size distribution curve at 60 % cumulative frequency	m
D'	Matrix of standardized well-logging data	–
E	Matrix of residuals in the decomposition of **D'**	–
F	Archie's formation factor	–
F	Matrix of factor scores	–
F_1'	First (scaled) factor	–
g	Normal acceleration of gravity	cm/s^2
GG	Gamma-gamma log reading	cps
GR	Natural gamma-ray intensity log reading	cps
GR_{sd}, GR_{min}	Natural gamma-ray intensity of sand	cps
GR_{sh}, GR_{max}	Natural gamma-ray intensity of shale	cps
h_0	Length of filter pack	m
h	Communality in the main diagonal of $\mathbf{R}^*$	–
$\mathbf{H}^2$	Matrix of communalities	–
I	Identity matrix	–
k	Hydraulic conductivity	m/s
K	Dimensionless hydraulic conductivity	–
L	Number of applied well log types	–
m	Cementation exponent in Archie's equation	–
M	Number of extracted statistical factors	–
N	Number of measuring points along a borehole	–
NN	Neutron-neutron intensity log reading	cpm
NN_f	Neutron-neutron intensity of pore-fluid	cpm
NN_{sh}	Neutron-neutron intensity of shale	cpm
NN_{sd}	Neutron-neutron intensity of sand	cpm
p	Pore pressure	Pa
P	Likelihood function used for the estimation of **F**	–
Q_{max}	Maximal theoretical water discharge	m^3/s
r_0	Radius of filter pack	m
R	Pearson's correlation coefficient	–
R	Correlation matrix of well-logging data	–

$\mathbf{R}^*$	Reduced correlation matrix of well-logging data	–
RMS	Root-mean-square error	%
S	Specific surface of rock grains	1/m
S	Sample covariance matrix of standardized data	–
S_w	Water saturation in the undisturbed formation	v/v
SP	Spontaneous potential log reading	mV
SP_{sh}	Spontaneous potential of shale	mV
t	Time	s
T	Temperature	°C
R_d, RD	Deep resistivity log reading	ohmm
R_{mf}	Resistivity of mud filtrate	ohmm
R_s, RS	Shallow resistivity log reading	ohmm
R_w	Resistivity of pore water	ohmm
R_0	Resistivity of rock fully saturated with water	ohmm
$\mathbf{S}_e$	Matrix of singular values	–
u	Relative displacement vector	m
U	Uniformity coefficient	–
U, **V**	Orthogonal matrices	–
v_c	Critical flow velocity	m/s
V_{sh}, VSH	Shale volume	v/v
V_{sd}, VSD	Sand volume	v/v
W	Matrix of factor loadings	–
z	Measured depth along a borehole	m
Z	Matrix of eigenvectors of $\mathbf{R}^*$	–
α_0	Shape factor of sample particles	–
α, β, γ	Regression coefficients for V_{sh} vs. F'_1 relation	–
$\mathbf{\Gamma}$	Matrix of sorted eigenvalues	–
θ	Constant for testing the number of statistical factors	–
$\mathbf{\Gamma}$	Matrix of eigenvalues (λ) of $\mathbf{R}^*$	–
κ	Intrinsic permeability	m^2
μ	Dynamic viscosity of water	Ns/m^2
υ	Kinematic viscosity of water	m^2/s
ρ	Spearman's rank correlation coefficient	–
ρ_b, DEN	Bulk density log reading	gcm^{-3}
ρ_{mf}	Density of mud filtrate	gcm^{-3}
ρ_{sd}	Density of sand	gcm^{-3}
ρ_{sh}	Density of shale	gcm^{-3}
ρ_w	Density of pore water	gcm^{-3}
σ	Data variance explained by a statistical factor	–
Φ, POR	Formation porosity	v/v
$\mathbf{\psi}$	Matrix of specific variances	–
Ω	Objective function used for estimating **W**	–
$\mathbf{\Omega}$	Matrix of eigenvectors	–

9. REFERENCES

[1] SERRA, O.: *Fundamentals of Well-log Interpretation*. Elsevier, Amsterdam, 1984.
[2] TSELENTIS, G. A.: The processing of geophysical well logs by microcomputers as applied to the solution of hydrogeological problems. *Journal of Hydrology*, 1985, 80, 215–236.
[3] RUBIN, Y.–HUBBARD, S. S.: *Hydrogeophysics*. Water Science and Technology Library Series 50. Springer-Verlag, Dordrecht–Berlin–Heidelberg–New York, 2005.
[4] WALSH, D.–TURNER, P.–GRUNEWALD, E.–ZHANG, H.–BUTLER, J. J.–REBOULET, E.–KNOBBE, S.–CHRISTY, T.–LANE, J. W.–JOHNSON, C. D.–MUNDAY, T.–FITZPATRICK A.: A small-diameter NMR logging tool for groundwater investigations. *Groundwater*, 2013, 51, 914–926.
[5] CSÓKÁS, J.: Determination of yield and water quality of aquifers based on geophysical well logs (in Hungarian). *Magyar Geofizika*, 1995, 35 (4), 176–203.
[6] ALGER, R. P.: Interpretation of electric logs in fresh water wells in unconsolidated formation. *SPE Reprint Series 1*, 1971, 255.
[7] LAWLEY, D. N.–MAXWELL, A. E.: Factor analysis as a statistical method. *The Statistician*, 1962, 12, 209–229.
[8] SZABÓ, N. P.: Shale volume estimation based on the factor analysis of well-logging data. *Acta Geophysica*, 2011, 59, 5, 935–953.
[9] BEAR, J.: *Dynamics of Fluids in Porous Media*. Dover Publications Inc., New York, 1972.
[10] JUHÁSZ, J.: *Hydrogeology* (in Hungarian). Akadémiai Kiadó, Budapest, 2002.
[11] LARIONOV, V. V.: *Radiometry of Boreholes* (in Russian). Nedra, Moscow, 1969.
[12] ALBERTY, M.–HASHMY, K.: Application of ULTRA to log analysis. *SPWLA Symposium Transactions*, 1984, Paper Z, 1–17.
[13] TIMUR, A.: An investigation of permeability, porosity, and residual water saturation relationships. *SPWLA 9th Annual Logging Symposium*, 1968, SPWLA-1968-J.
[14] DRAHOS, D.: Inversion of engineering geophysical penetration sounding logs measured along a profile. *Acta Geodetica et Geophysica*, 2005, 40, 193–202.
[15] SZABÓ, N. P.–DOBRÓKA, M.: Float-encoded genetic algorithm used for the inversion processing of well-logging data. In: Michalski, A. (ed.) *Global optimization: Theory, developments and applications*. Mathematics Research Developments, Computational Mathematics and Analysis Series, Nova Science Publishers Inc, New York, 2013.
[16] KOVÁCS, GY.: *Hydraulics of Filtration* (in Hungarian). Akadémiai Kiadó, Budapest, 1972.
[17] ARCHIE, G. E.: The electrical resistivity log as an aid in determining some reservoir characteristics. *SPE, Transactions of the AIME*, 1942, 146 (1), 54–62.

[18] OGBE, D.–BASSIOUNI, Z.: Estimation of aquifer permeabilities from electric well logs. *The Log Analyst*, 1978, 19 (5), 21–27.
[19] PIRSON, S. J.: *Handbook of Well Log Analysis*. Prentice-Hall Inc., New York, 1963.
[20] GÁLFI, J.–LIEBE, P.: The permeability coefficient in clastic water bearing rocks (in Hungarian). *Vízügyi Közlemények*, 1981, 63 (3), 437–448.
[21] SCHMIEDER, A.: *Water-Risk and Water Economy in Mining* (in Hungarian). Műszaki Könyvkiadó, Budapest, 1975.
[22] KASSAI, F.–JAMBRIK, R.: *Water Mining II.* (in Hungarian). Tankönyvkiadó, Budapest, 1986.
[23] JÖRESKOG, K. G.: Factor analysis and its extensions. In: Cudeck, R.–MacCallum, R. C. (eds.): *Factor analysis at 100, Historical developments and future directions.* Lawrence Erlbaum Associates, New Jersey, 2007.
[24] JÖRESKOG, K. G.: A general approach to confirmatory maximum likelihood factor analysis. *Psychometrika*, 1969, 34 (2), 183–202.
[25] BARTLETT, M. S.: Factor analysis in psychology as a statistician sees it. *Nordisk Psykologi's Monograph Series 3*, 1953, Almqvist & Wiksell, Uppsala, 23–34.
[26] BARTLETT, M. S.: Tests of significance in factor analysis. *British Journal of Psychology*, 1950, 3 (2), 77–85.
[27] KAISER, H. F.: The varimax criterion for analytical rotation in factor analysis. *Psychometrika*, 1958, 23, 187–200.

Geosciences and Engineering, Vol. 4, No. 6 (2015), pp. 72–80.

JOINT INVERSION OF DIFFERENT TYPES OF GEODETIC MEASUREMENTS TO OBTAIN ACCURATE HORIZONTAL COORDINATES

GÁBOR MOLNÁR

MTA–ELTE Geological, Geophysical and Space Science Research Group
molnar@sas.elte.hu

Abstract. In this paper the adjustment (joint inversion) of different types of position, distance and bearing measurements is presented to get accurate horizontal coordinates of the stations of an open traverse. An approximately 1 km long open traverse was measured in a hilly area, in a forest covered gully, where GPS signal for the handheld receivers (used to measure horizontal coordinates of the stations) was weak. Typical station distances were 5 to 10 meters, and were directly measured with a measuring tape. The bearing (azimuth) between the subsequent stations was measured with a geological (magnetic) compass.

To get adjusted horizontal coordinates of the stations, the formulation of conditional adjustment is applied [1]. Conditional equations express the relationship between different types of measurements. The measurements usually do not fulfill the conditional equations because of the measurement error, but adjusted measurement values (measured values plus their correction) do. As usually the number or measurements is greater than the number of conditional equations, the problem is underdetermined. To solve the equations we have to add another criterion: the sum of the weighted squares of these corrections should be minimal. Applying this minimum criteria results in an algebraic equation system. By solving these equations we get the corrections of the measurements. Finally we present the corrected horizontal coordinates overlaid on a map demonstrating the method's accuracy.

1. INTRODUCTION

It is typical in the case of field geophysical measurements that the location information (map grid coordinates) are measured with handheld GPS receivers. If measurement points are spread several thousand meters from each other, the typical GPS error of some tens of meters is negligible. However, if measurement points are situated some tens of meters (or even less) from each other, errors cannot be neglected. If we try to overlay the measured coordinates on a map, the coordinates measured along a straight profile appear as a zigzag line on the map (see blue dots in Figure 1).

To overcome this problem we might measure the distances between the measurement locations (stations) with measuring tape, with an accuracy of some centimeters. Additionally we might measure the relative direction (azimuth) of two stations with a magnetic compass with an accuracy of some degrees. Combining these two measurements we might also calculate the coordinate differences of the two stations, but with this method we do not get map grid coordinates.

In this paper a method is presented to combine GPS and classical (measuring tape and compass) measurement. GPS measurement supports the global positioning, while the measuring tape and compass ensure the accuracy of the relative locations of the measurements.

There are several approaches and methods to combine such different types of position measurements [2]. A widely used, real-time processing solution is the Kalman-filter method [3]. Applying a Kalman-filter for location calculation, the estimated coordinates of the stations are calculated combining the previous station position plus the actual measurements. The disadvantage of the Kalman-filter method is that it requires a long initialization time-span.

The conditional least squares method presented in this paper enables us to combine all available measurements along the traverse in a post-processing step.

2. MATERIALS AND METHODS

2.1. Conditional equations

2.1.1. Distance measurements

If we measure the map grid coordinates of two stations with GPS, we get 4 values: easting and northing coordinates of the two points. Let us also measure the distance between the two stations with a measuring tape. If all measurements are free of errors, then the next equation (the Pythagoras equation expressed in Cartesian coordinates) will have been fulfilled:

$$\sqrt{(E_2 - E_1)^2 + (N_2 - N_1)^2} - d_{12} \neq 0 \tag{1}$$

where E_1 and E_2 are eastings, N_1 and N_2 are northings of the two stations measured by GPS and d_{12} is the distance between the two stations measured with a measuring tape. In reality the right hand side is usually not zero, we call this value misclosure.

Let us suppose that we know the 'true' or 'error-free' values of the measurements! The difference between the 'error-free' and the measured values is called 'correction' and denoted by ν. With these corrections, the conditional equation would be fulfilled

$$\sqrt{((E_2 + v_{E2}) - (E_1 + v_{E1}))^2 + ((N_2 + v_{N2}) - (N_1 + v_{N1}))^2} - (d_{12} + v_{d12}) = 0\,, \tag{2}$$

where ν_{E1}, ν_{E2}, ν_{N1}, ν_{N2}, and ν_{d12} are the corrections for the GPS coordinate measurements and measuring tape measurements, respectively.

2.1.2. Azimuth measurements

A similar condition equation can be written for the bearing (azimuth) from one station to another: in the case of 'error-free' measurements, the azimuth measured

with a magnetic compass should fit the azimuth computed from map grid coordinates measured with GPS:

$$\arctan\left(\frac{N_2 - N_1}{E_2 - E_1}\right) - \varphi_{12} \neq 0 \tag{3}$$

where E_1 and E_2 are eastings, N_1 and N_2 are northings of the two stations measured by GPS and φ_{12} is the azimuth from the first station to the second, measured with a magnetic compass.

Adding corrections to the measured values, the conditional equation could be fulfilled:

$$\arctan\left(\frac{\left(N_2 + \nu_{N2}\right) - \left(N_1 + \nu_{N1}\right)}{\left(E_2 + \nu_{E2}\right) - \left(E_1 + \nu_{E1}\right)}\right) - \left(\varphi_{12} + \nu_{\varphi 12}\right) \neq 0 \tag{4}$$

where $\nu_{\varphi 12}$ is the correction for the magnetic compass azimuth measurement. It is important to emphasize that four of the corrections (ν_{E1}, ν_{N1}, ν_{E2}, ν_{N2}) are the same as in Eq. (2).

2.1.3. Measurements along an open traverse

In the previous section we saw that for two stations, we have six measurements and two conditional equations. If we develop our traverse, by adding one further station point we increase the number of measurements by four (two GPS coordinates, one measuring tape and one compass measurement) and we increase the number of conditional equations by two.

If we have the number of stations n, then the number of measurements is $4n+2$, and the number of conditional equations is $2n-2$. For practical reasons we order our measurements in the sequence:

$$E_1, N_1, d_{12}, \varphi_{12}, E_2, N_2, d_{23}, \varphi_{23}, E_3, N_3, d_{34}, \varphi_{34}, \ldots E_N, N_N \tag{5}$$

(In this case, adding new traverse stations to the calculations, the sequence of the previous measurements does not need to be changed.)

2.2. Weighted least squares

If we have only two stations along the traverse, then Eqs. (2) and (4) have six unknowns: ν_{E1}, ν_{N1}, ν_{d12}, $\nu_{\varphi 12}$, ν_{E2}, ν_{N2}. Certainly we could find many sets of six correction values that could be substituted into Eqs. (2) and (4) so that the right hand side would be zero. As we have only two equations and six unknowns (the corrections) our problem is underdetermined. This case does not change by adding further stations to the traverse; the number of unknowns is always greater than the number of equations.

We might overcome this problem by introducing another condition, that the sum of the squares of the residuals should be minimal.

$$\sum v_i^2 := \min \tag{6}$$

We use the squares because we want the correction values as small (as close to zero) as possible. In our case, however we have to take into account that different types of measurements have different measured quantities (length and angles) and different degrees of accuracy. For a more accurate measurement we accept a small correction value, and for a less accurate measurement we might get a greater correction value. We might overcome this problem by minimizing the sum of the squares of residuals multiplying by weights. We call it weighted squares of the residuals:

$$\sum p_i v_i^2 := \min \tag{7}$$

The weight applied for a measurement is usually the reciprocal of the variance (square of the standard deviation) of the measurement:

$$\sum \frac{1}{\sigma_i^2} v_i^2 := \min \tag{8}$$

We might re-formulate this in an array-matrix form:

$$\mathbf{v}^{\mathbf{T}} \mathbf{P}_{\mathbf{LL}} \mathbf{v} := \min \ , \tag{9}$$

where $\mathbf{v}$ denotes the array notation of residuals, $(\ldots)^T$ stands for transpose and $\mathbf{P}_{\mathbf{LL}}$ is the weight matrix composed of the weights. Statistical theory proves that if the measurements are correlated, the best unbiased estimation of the corrections is using the inverse of the covariance matrix of measurements as a weight matrix [1]:

$$\mathbf{P}_{\mathbf{LL}} = \mathbf{\Sigma}_{\mathbf{LL}}^{-1} \tag{10}$$

In our case, as we could not repeat the measurements to get a real covariance matrix, we applied a weight matrix containing only diagonal elements. For two stations, and supposing the standard deviation of GPS measurements is 10 meters, that of measuring tape measurements is 0.1 meters and that of compass azimuth measurements is 5 degrees, we get (following the sequence of measurements, Eq. (5)):

$$\mathbf{P_{LL}} = \begin{pmatrix} \frac{1}{\sigma^2_{E_1}} & & & & & & \\ & \frac{1}{\sigma^2_{N_1}} & & & & & \\ & & \frac{1}{\sigma^2_{d_{12}}} & & & & \\ & & & \frac{1}{\sigma^2_{\varphi_{12}}} & & & \\ & & & & \frac{1}{\sigma^2_{E_2}} & & \\ & & & & & \frac{1}{\sigma^2_{N_2}} \end{pmatrix} = \begin{pmatrix} 0.01 & & & & & & \\ & 0.01 & & & & & \\ & & 100 & & & & \\ & & & 0.04 & & & \\ & & & & 0.01 & & \\ & & & & & 0.01 \end{pmatrix} \quad (11)$$

If a further station point is added, the matrix will have four more diagonal elements.

2.3. Conditional least squares

2.3.1. Formulation of the conditional least squares

In our case we want to use the weighted least squares condition to calculate the corrections, but at the same time the conditional equation should be fulfilled. This problem is known as 'conditional least squares' or the 'Gauss–Helmert-formulation' of the method of least squares [1]:

In this case the minimum condition:

$$\mathbf{v}^{\mathbf{T}}\mathbf{P}_{LL}\mathbf{v} - 2\cdot\mathbf{k}^{\mathbf{T}}\left(\mathbf{Bv}-\mathbf{l}\right) := \min \quad (12)$$

where **k** is the array of Lagrange multipliers and **Bv–l** is the conditional equation rewritten as a linear function of the corrections (**v**). To get this linear form, we are using a Taylor series to the first term of expansion.

2.3.2. Jacobian and the misclosure array

In Eq. (12) we see that the conditional equations should be rewritten as a linear function of the corrections, this is denoted:

$$\mathbf{Bv}-\mathbf{l}=0 \quad (13)$$

Let us consider the meaning of the **l** array. This so-called misclosure array is the deviation of the condition equations from zero. If we have only two stations and so only two conditional equations, then the misclosure array has only two components: first the value of Eq. (1) and for the second component the value of Eq. (3). Adding a further station to the calculations increases the number of elements of the misclosure array by two.

The **B** matrix is the Jacobian of the conditional equations, i.e. the partial derivatives of the conditional equations with respect to the corrections (**v**). For two stations and the condition related to the distance measurements (Eq. (2)) the derivatives are:

$$\begin{aligned}
\frac{\partial l_{d_{12}}}{\partial E_1} &= \frac{-E_1}{\sqrt{(E_2-E_1)^2+(N_2-N_1)^2}} \\
\frac{\partial l_{d_{12}}}{\partial E_2} &= \frac{E_2}{\sqrt{(E_2-E_1)^2+(N_2-N_1)^2}} \\
\frac{\partial l_{d_{12}}}{\partial N_1} &= \frac{-N_1}{\sqrt{(E_2-E_1)^2+(N_2-N_1)^2}} \\
\frac{\partial l_{d_{12}}}{\partial N_2} &= \frac{N_2}{\sqrt{(E_2-E_1)^2+(N_2-N_1)^2}} \\
\frac{\partial l_{d_{12}}}{\partial d_{12}} &= -1
\end{aligned} \tag{14}$$

For the azimuth measurements, the derivatives of Eq. (4) are:

$$\begin{aligned}
\frac{\partial l_{\varphi_{12}}}{\partial E_1} &= \frac{E_1}{(E_2-E_1)^2+(N_2-N_1)^2} \\
\frac{\partial l_{\varphi_{12}}}{\partial E_2} &= \frac{-E_2}{(E_2-E_1)^2+(N_2-N_1)^2} \\
\frac{\partial l_{\varphi_{12}}}{\partial N_1} &= \frac{N_1}{(E_2-E_1)^2+(N_2-N_1)^2} \\
\frac{\partial l_{\varphi_{12}}}{\partial N_2} &= \frac{-N_2}{(E_2-E_1)^2+(N_2-N_1)^2} \\
\frac{\partial l_{\varphi_{12}}}{\partial \varphi_{12}} &= -1
\end{aligned} \tag{15}$$

Similar derivatives can be written for the conditional equations of every pair of side-by-side situated stations. We have to arrange these expressions into the **B** matrix in the sequence of measurements defined by Eq. (5):

$$\mathbf{B}=\begin{bmatrix} \frac{\partial l_{d_{12}}}{\partial E_1} & \frac{\partial l_{d_{12}}}{\partial N_1} & \frac{\partial l_{d_{12}}}{\partial d_{12}} & 0 & \frac{\partial l_{d_{12}}}{\partial E_2} & \frac{\partial l_{d_{12}}}{\partial N_2} & 0 & 0 & 0 & 0 & \cdots \\ \frac{\partial l_{\varphi_{12}}}{\partial E_1} & \frac{\partial l_{\varphi_{12}}}{\partial N_1} & 0 & \frac{\partial l_{\varphi_{12}}}{\partial \varphi_{12}} & \frac{\partial l_{\varphi_{12}}}{\partial E_2} & \frac{\partial l_{\varphi_{12}}}{\partial N_2} & 0 & 0 & 0 & 0 & \cdots \\ 0 & 0 & 0 & 0 & \frac{\partial l_{d_{23}}}{\partial E_2} & \frac{\partial l_{d_{23}}}{\partial N_2} & \frac{\partial l_{d_{23}}}{\partial d_{23}} & 0 & \frac{\partial l_{d_{23}}}{\partial E_3} & \frac{\partial l_{d_{23}}}{\partial N_3} & \cdots \\ 0 & 0 & 0 & 0 & \frac{\partial l_{\varphi_{23}}}{\partial E_2} & \frac{\partial l_{\varphi_{23}}}{\partial N_2} & 0 & \frac{\partial l_{\varphi_{23}}}{\partial \varphi_{23}} & \frac{\partial l_{\varphi_{23}}}{\partial E_3} & \frac{\partial l_{\varphi_{23}}}{\partial N_3} & \cdots \\ \vdots & \vdots & \vdots & \vdots & \vdots & \vdots & \vdots & \vdots & \vdots & \vdots & \ddots \end{bmatrix} \tag{16}$$

2.3.3. Solution of the equations: corrections and Lagrange-multipliers

Equation (12) as a function of corrections (**v**) and Lagrange-multipliers (**k**) should be minimal. This implies that the derivative of Eq. (12) with respect to the corrections and to the Lagrange-multipliers should be zero. This defines two equations:

$$\begin{aligned} \mathbf{P}_{LL}\mathbf{v}-\mathbf{B}^{\mathrm{T}}\mathbf{k}&=\mathbf{0} \\ \mathbf{B}\mathbf{v}-\mathbf{l}&=\mathbf{0} \end{aligned} \tag{17}$$

We might rearrange this equation into a hypermatrix form:

$$\begin{pmatrix} \mathbf{P}_{LL} & -\mathbf{B}^{\mathrm{T}} \\ -\mathbf{B} & \mathbf{0} \end{pmatrix} \cdot \begin{pmatrix} \mathbf{v} \\ \mathbf{k} \end{pmatrix} = \begin{pmatrix} \mathbf{0} \\ -\mathbf{l} \end{pmatrix} \tag{18}$$

Solving this algebraic equation yields the array of residuals (**v**) and Lagrange-multipliers (**k**). Adding the residual values to the measurement we get the adjusted values of the measurements.

Two problems arise. First, the conditional equations are not the linear function of the residuals (we just linearized them neglecting higher order terms). Secondly the initial values of the measurements are not close to the finally adjusted ones and so the initial values of the derivatives greatly differ from the derivatives at the adjusted measurements.

As a consequence, we do not get the corrections in one step, we have to iterate, i.e. repeat the calculations with the adjusted values until the order of magnitude of the corrections is less than a predefined threshold. Typically the required number of iteration steps is in the magnitude of the number of stations.

3. RESULTS

In Figure 1 the map grid coordinates of the traverse are overlaid on a topographic map. Blue dots represent the GPS measurements, while black ones represent the

adjusted (corrected) coordinates. It is obvious that the traverse follows a smoother trajectory, situated in the sole valley.

One possible way of improvement of the method is applying a more realistic covariance matrix of measurements. For example the errors of subsequent GPS measurements are rarely uncorrelated, but the correlation decreases with time. So the correlation values of subsequent GPS measurement can be approximated as a decreasing function of time difference of GPS measurements, forming a band matrix with greatest values in the diagonal and decreasing with the distance from the diagonal.

The method presented here is well known for geodesists since long time ago, but it is not applied by geodesists because the results do not meet the high accuracy requirements of the geodesists. However this method can be applied by geographers, geologists and geophysicist to locate their field observations and measurements using commonly available surveying instruments as handheld GPS, measuring tape and a compass.

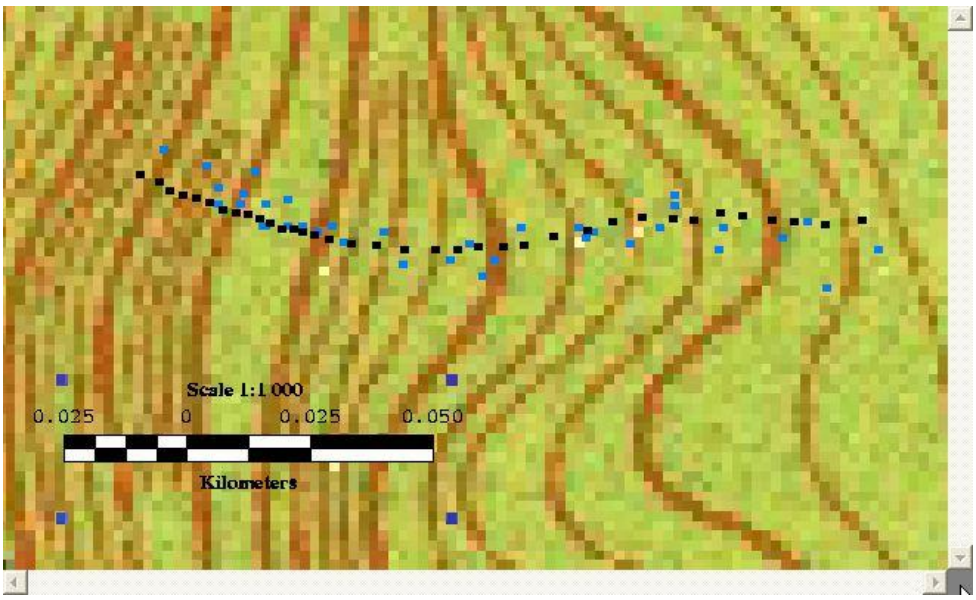

Figure 1
A traverse overlaid on a 1:10000 scale topographic map. Blue dots are station coordinates measured with GPS, black dots represent the adjusted horizontal coordinates

4. LIST OF SYMBOLS

Symbol	Description	Unit
E_1	easting of the first station	m
E_2	easting of the second station	m
d_{12}	distance between the first two stations	m
N_1	northing of the first station	m

N_2	northing of the second station	m
φ_{12}	azimuth from the first station to the second	°
v	correction, i.e. the difference between the measured and the 'errorfree' values	–
p_i	weight of the i^{th} measurement	dimensionless number
σ_i	variance of the i^{th} measurement	–
$\mathbf{v}$	array notation of corrections	–
$\mathbf{P_{LL}}$	weight matrix of measurements	–
$\mathbf{k}$	array of Lagrange-multipliers	–
$\mathbf{l}$	misclosure array	–
$\mathbf{B}$	Jacobian-matrix	–

5. REFERENCES

[1] MIKHAIL, E. M.–ACKERMANN. F. E.: *Observations and Least Squares*. University Press of America, 1982.
[2] KAHMEN, H.–FAIG, W.: *Surveying*. de Gruyter, Berlin–New York, 1988.
[3] KALMAN, R. E.: A New Approach to Linear Filtering and Prediction Problems. *Transactions of the ASME – Journal of Basic Engineering*, 1960, 82, 35–45.

Geosciences and Engineering, Vol. 4, No. 6 (2015), pp. 81–92.

INVERSION RECONSTRUCTION OF 3D GRAVITY POTENTIAL FUNCTION INCLUDING VERTICAL DEFLECTIONS

LAJOS VÖLGYESI[1]–GYULA TÓTH[1]–MIHÁLY DOBRÓKA[2]

[1]*Department of Geodesy and Surveying, Faculty of Civil Engineering, Budapest University of Technology and Economics*
volgyesi@eik.bme.hu, gtoth@agt.bme.hu
[2]*Department of Geophysics, University of Miskolc*
dobroka@uni-miskolc.hu

Abstract. Inversion reconstruction of 3D gravity potential based on gravity data measured by gravimeters, horizontal gravity gradients and curvature data measured by torsion balance and vertical gradients, including vertical deflection data have been obtained by our 3D solution. By applying this method the potential function – apart from an additive constant – and all the first and second derivatives of this potential function (elements of the full Eötvös-tensor) can be determined not only at points of the region covered by measurements, but anywhere in the surroundings of these measurement points, using the coefficients of expansion in a series of a known set of basis function. The advantage of this method is that the solution can be performed by a significantly overdetermined inverse problem.

Computations were made for the inversion reconstruction of gravity potential at a test area where gravity, torsion balance, vertical gradient measurements and vertical deflection data were available. Gravity potential, vertical deflections and both the first and the second derivatives of the potential were determined for the whole area by this suggested method.

1. INTRODUCTION

There are more than 45,000 torsion balance measurements in a computer database in Hungary. Earlier measurements were made mainly for geophysical prospecting, but nowadays more efficient methods are applied in geophysics and instead of a geophysical application of the torsion balance measurements, geodetic applications have come to the front. Possibilities of geodetic applications of gravity gradients are continually growing [1] [2] [3] [4] [5].

Determination of the potential function has great importance because all components of the gravity vector, vertical deflection and the elements of the full Eötvös tensor can be derived from it as the first and the second derivatives of this function. Now a solution of the determination of 3D potential function is given here as an improvement on our former solution of 2D inversion [6] and [7]. Besides gravity and gravity gradients, now we have integrated vertical deflection data into the computations. Nowadays revolutionary changes are expected in geodesy because we have a new system which is capable of measuring very precise vertical deflection data with high efficiency [8].

For verification of the 3D inversion algorithm, test computations were performed at the south part of Csepel Island, a location where gravity, torsion balance, vertical gradient and vertical deflection data are available from a new model.

2. THE INVERSION ALGORITHM

Let us choose the 3D gravity potential $W(x, y, z)$ as a series expansion into a known set of basis function $\Psi_1,.\Psi_2,..., \Psi_P$:

$$W(x,y,z) = \sum_{i=1}^{N_x}\sum_{j=1}^{N_y}\sum_{k=1}^{N_z} B_n \Psi_i(x)\Psi_j(y)\Psi_k(z), \tag{1}$$

where $n = i + (j-1)N_y + (k-1)N_xN_y$ and B_n are unknown coefficients of the series expansion. In our investigations Legendre polynomials are applied as basis functions. The constant term is marked by index 1, so the possibility of $I = j = k = 1$ can be precluded, because the potential is unique apart from an additive constant.

The second derivatives of the potential Eq. (1) (the elements of the Eötvös-tensor) give the computed values of horizontal gradients W_{zx}, W_{zy}, curvature data W_Δ, W_{xy} and vertical gradients W_{zz} as

$$W_{zx} = \frac{\partial^2 W}{\partial x \partial z} = \sum_{i=1}^{N_x}\sum_{j=1}^{N_y}\sum_{k=1}^{N_z} B_n \Psi_i'(x)\Psi_j(y)\Psi_k'(z)\,, \tag{2}$$

$$W_{zy} = \frac{\partial^2 W}{\partial y \partial z} = \sum_{i=1}^{N_x}\sum_{j=1}^{N_y}\sum_{k=1}^{N_z} B_n \Psi_i(x)\Psi_j'(y)\Psi_k'(z)\,, \tag{3}$$

$$W_{xy} = \frac{\partial^2 W}{\partial x \partial y} = \sum_{i=1}^{N_x}\sum_{j=1}^{N_y}\sum_{k=1}^{N_z} B_n \Psi_i'(x)\Psi_j'(y)\Psi_k(z), \tag{4}$$

$$\begin{aligned} W_\Delta = W_{yy} - W_{xx} &= \frac{\partial^2 W}{\partial y^2} - \frac{\partial^2 W}{\partial x^2} = \\ &= \sum_{i=1}^{N_x}\sum_{j=1}^{N_y}\sum_{k=1}^{N_z} B_n \left\{ \Psi_i(x)\,\Psi_j''(y) - \Psi_i''(x)\,\Psi_j(y) \right\} \Psi_k(z)\,, \end{aligned} \tag{5}$$

$$W_{zz} = \frac{\partial^2 W}{\partial z^2} = \sum_{i=1}^{N_x}\sum_{j=1}^{N_y}\sum_{k=1}^{N_z} B_n \Psi_i(x)\,\Psi_j(y)\,\Psi_k''(z), \tag{6}$$

where the prime $'$ denotes differentiation with respect to the argument of the basis function.

The required first derivatives for the inversion algorithm are

$$W_x = \frac{\partial W}{\partial x} = \sum_{i=1}^{N_x}\sum_{j=1}^{N_y}\sum_{k=1}^{N_z} B_n \Psi_i'(x)\,\Psi_j(y)\,\Psi_k(z)\,, \tag{7}$$

$$W_y = \frac{\partial W}{\partial y} = \sum_{i=1}^{N_x}\sum_{j=1}^{N_y}\sum_{k=1}^{N_z} B_n \Psi_i(x)\,\Psi_j'(y)\,\Psi_k(z)\,, \tag{8}$$

$$W_z = \frac{\partial W}{\partial z} = \sum_{i=1}^{N_x}\sum_{j=1}^{N_y}\sum_{k=1}^{N_z} B_n \Psi_i(x)\,\Psi_j(y)\,\Psi_k'(z)\,. \tag{9}$$

Because the potential field should fulfill the Laplace-equation $\Delta W = W_{xx} + W_{yy} + W_{zz} = 0$ at each (free air) measurement point, the computed value of ΔW can be written as

$$\begin{aligned}\Delta W &= \frac{\partial^2 W}{\partial x^2} + \frac{\partial^2 W}{\partial y^2} + \frac{\partial^2 W}{\partial z^2} = \\ &= \sum_{i=1}^{N_x}\sum_{j=1}^{N_y}\sum_{k=1}^{N_z} B_n \left\{ \Psi_i''(x)\Psi_j(y)\Psi_k(z) + \Psi_i(x)\Psi_j''(y)\Psi_k(z) + \Psi_i(x)\Psi_j(y)\Psi_k''(z) \right\}.\end{aligned} \tag{10}$$

At an arbitrary measurement point $P(x_P, y_P, z_P)$ the computable data based on Eqs. (2)–(10) are:

$$^{comp.}W_{zx}^{(P)} = \sum_{n=1}^{M} B_n A_{Pn}^{(1)}\,, \tag{11}$$

$$^{comp.}W_{zy}^{(P)} = \sum_{n=1}^{M} B_n A_{Pn}^{(2)}\,, \tag{12}$$

$$^{comp.}W_{xy}^{(P)} = \sum_{n=1}^{M} B_n A_{Pn}^{(3)}\,, \tag{13}$$

$$^{comp.}W_{\Delta}^{(P)} = \sum_{n=1}^{M} B_n A_{Pn}^{(4)}\,, \tag{14}$$

$$^{comp.}W_{zz}^{(P)} = \sum_{n=1}^{M} B_n A_{Pn}^{(5)}\,, \tag{15}$$

$$^{comp.}W_{x}^{(P)} = \sum_{n=1}^{M} B_n A_{Pn}^{(6)}\,, \tag{16}$$

$$^{comp.}W_{y}^{(P)} = \sum_{n=1}^{M} B_n A_{Pn}^{(7)}\,, \tag{17}$$

$$^{comp.}W_z^{(P)} = \sum_{n=1}^{M} B_n A_{Pn}^{(8)}\,, \tag{18}$$

$$^{comp.}\Delta W^{(P)} = \sum_{n=1}^{M} B_n A_{Pn}^{(9)}\,, \tag{19}$$

where $M = N_x N_y N_z - 1$ is the number of coefficients of the series expansion, and

$$A_{Pn}^{(1)} = \Psi_i'(x_P)\Psi_j(y_P)\Psi_k'(z_P)\,, \tag{20}$$

$$A_{Pn}^{(2)} = \Psi_i(x_P)\Psi_j'(y_P)\Psi_k'(z_P)\,, \tag{21}$$

$$A_{Pn}^{(3)} = \Psi_i'(x_P)\Psi_j'(y_P)\Psi_k(z_P)\,, \tag{22}$$

$$A_{Pn}^{(4)} = \left\{\Psi_i(x_P)\,\Psi_j''(y_P) - \Psi_i''(x_P)\,\Psi_j(y_P)\right\}\Psi_k(z_P)\,, \tag{23}$$

$$A_{Pn}^{(5)} = \Psi_i(x_P)\Psi_j(y_P)\Psi_k''(z_P)\,, \tag{24}$$

$$A_{Pn}^{(6)} = \Psi_i'(x_P)\Psi_j(y_P)\Psi_k(z_P)\,, \tag{25}$$

$$A_{Pn}^{(7)} = \Psi_i(x_P)\Psi_j'(y_P)\Psi_k(z_P)\,, \tag{26}$$

$$A_{Pn}^{(8)} = \Psi_i(x_P)\Psi_j(y_P)\Psi_k'(z_P)\,, \tag{27}$$

$$A_{Pn}^{(9)} = \left\{\Psi_i''(x_P)\Psi_j(y_P)\Psi_k(z_P) + \Psi_i(x_P)\Psi_j''(y_P)\Psi_k(z_P) + \Psi_i(x_P)\Psi_j(y_P)\Psi_k''(z_P)\right\} \tag{28}$$

are known (computable) matrix elements at the P^{th} measurement point.

The P^{th} element of the discrepancy vector of the *measured* and the *computed* data is:

$$\varepsilon_P^{(1)} = {}^{meas.}W_{zx}^{(P)} - \sum_{n=1}^{M} B_n A_{Pn}^{(1)}\,, \tag{29}$$

$$\varepsilon_P^{(2)} = {}^{meas.}W_{zy}^{(P)} - \sum_{n=1}^{M} B_n A_{Pn}^{(2)}\,, \tag{30}$$

$$\varepsilon_P^{(3)} = {}^{meas.}W_{xy}^{(P)} - \sum_{n=1}^{M} B_n A_{Pn}^{(3)}\,, \tag{31}$$

$$\varepsilon_P^{(4)} = {}^{meas.}W_{\Delta}^{(P)} - \sum_{n=1}^{M} B_n A_{Pn}^{(4)}\,, \tag{32}$$

$$\varepsilon_P^{(5)} = {}^{meas.}W_{zz}^{(P)} - \sum_{n=1}^{M} B_n A_{Pn}^{(5)}\,, \tag{33}$$

$$\varepsilon_P^{(6)} = {}^{meas.}W_{x}^{(P)} - \sum_{n=1}^{M} B_n A_{Pn}^{(6)}\,, \tag{34}$$

$$\varepsilon_P^{(7)} = {}^{meas.}W_y^{(P)} - \sum_{n=1}^{M} B_n A_{Pn}^{(7)}, \tag{35}$$

$$\varepsilon_P^{(8)} = {}^{meas.}W_z^{(P)} - \sum_{n=1}^{M} B_n A_{Pn}^{(8)}, \tag{36}$$

$$\varepsilon_P^{(9)} = 0 - \sum_{n=1}^{M} B_n A_{Pn}^{(9)}. \tag{37}$$

The ${}^{meas.}W_{zx}^{(P)}$, ${}^{meas.}W_{zy}^{(P)}$, ${}^{meas.}W_{xy}^{(P)}$ and the ${}^{meas.}W_{\Delta}^{(P)}$ in Eqs. (29)–(32) are torsion balance measurements, ${}^{meas.}W_{zz}^{(P)}$ in Eq. (33) are vertical gradient data, ${}^{meas.}W_z^{(P)}$ in Eq. (36) are gravity values measurable by gravimeters while ${}^{meas.}W_x^{(P)}$ in Eq. (34) and ${}^{meas.}W_y^{(P)}$ in Eq. (35) can be computed from vertical deflections. The first derivatives of the potential W from the vertical deflections are expressed as:

$$W_x = -g\xi + U_x, \tag{38}$$

$$W_y = -g\eta + U_y, \tag{39}$$

where U is normal potential [9], g is gravity and ξ, η are components of the deflection of the vertical. Equation (37) is equivalent to the Laplace-equation.

Let our inverse problem be overdetermined and let the function to be minimized be the L_2 norm of the discrepancy vector:

$$E = \sum_{s=1}^{9} \sum_{P=1}^{N_s} (\varepsilon_P^{(s)})^2, \tag{40}$$

where N_s is the number of measurements.

Let us introduce the following vector notations for measured and computed data:

$$\begin{aligned} {}^{meas.}\mathbf{d} = \{ & {}^{meas.}W_{zx}^{(1)},\ldots,{}^{meas.}W_{zx}^{(N_1)},\ldots,{}^{meas.}W_{zy}^{(1)},\ldots,{}^{meas.}W_{zy}^{(N_2)},\ldots\ldots \\ & \ldots\ldots,{}^{meas.}W_z^{(1)},\ldots,{}^{meas.}W_z^{(N_8)}, 0^{(1)},\ldots,0^{(N_9)} \} \end{aligned} \tag{41}$$

$$\begin{aligned} {}^{comp.}\mathbf{d} = \{ & {}^{comp.}W_{zx}^{(1)},\ldots,{}^{comp.}W_{zx}^{(N_1)},\ldots,{}^{comp.}W_{zy}^{(1)},\ldots,{}^{comp.}W_{zy}^{(N_2)},\ldots\ldots \\ & \ldots\ldots,{}^{comp.}W_z^{(1)},\ldots,{}^{comp.}W_z^{(N_8)},{}^{comp.}\Delta W^{(1)},\ldots,{}^{comp.}\Delta W^{(N_9)} \} \end{aligned} \tag{42}$$

All of the values of $A_{Pn}^{(i)}$ in Eqs. (20)–(28) can be written to a single coefficient matrix (to the so-called Jacobian):

$$G_{Pj}=\begin{cases} A_{Pj}^{(1)} & P \le N_1 \\ A_{Pj}^{(2)} & N_1 < P \le N_1 + N_2 \\ \vdots & \\ A_{Pj}^{(9)} & \sum_{s=1}^{8} N_s < P \le \sum_{s=1}^{9} N_s \end{cases}. \tag{43}$$

and using Eqs. (11)–(19) the vector of computed data takes the form of

$$^{comp}\mathbf{d}=\mathbf{GB}. \tag{44}$$

The discrepancy vector of measured and computed data is:

$$\boldsymbol{\varepsilon}=\,^{meas}\mathbf{d}-\mathbf{GB}, \tag{45}$$

and substituting this into (40) one gets

$$E=(\boldsymbol{\varepsilon},\boldsymbol{\varepsilon})=\sum_{P=1}^{N} e_P^2 \tag{46}$$

for the norm, where $N=\sum_{s=1}^{9} N_s$, the total number of measurements.

The solution of this inverse problem is based on the system of conditions

$$\frac{\partial E}{\partial B_n}=0,\ (n=1,...,M) \tag{47}$$

resulting in the set of normal equations

$$\mathbf{G}^T\mathbf{GB}=\mathbf{G}^T\,^{meas.}\mathbf{d}. \tag{48}$$

Since this inverse problem is linear, the vector **B** of series expansion coefficients can be determined by solving the above set of equations, yielding

$$\mathbf{B}=\left(\mathbf{G}^T\mathbf{G}\right)^{-1}\mathbf{G}^T\,^{meas.}\mathbf{d}. \tag{49}$$

So the potential function in this approximation – apart from an additive constant – and all of the first and second derivatives of this potential function (the elements of the full Eötvös-tensor) can be determined not only at points of the region covered

by measurements, but anywhere in the surroundings of these measurement points using the coefficients of expansion in a series of a known set of basis function.

3. TEST COMPUTATIONS

To verify the 3D inversion algorithm, test computations were made at the south part of Csepel Island in Hungary, where gravity, torsion balance (TB) and vertical gradient (VG) measurements have been performed, furthermore vertical deflection data were available from a new model [12]. Torsion balance measurements were made here in 1950 and 30 new measurements were made in a denser net between the years 2006 and 2009, supplemented by gravity and vertical gradient observations (supported by an earlier OTKA project managed by G. Csapó [10] [11]). The location of the 4 earlier torsion balance measurement points is marked by squares, the 30 new measurement points are marked by circles and dots, while the 21 gravity measurement points are marked by crosses in Figure 1. Vertical gradient data have been measured at 27 torsion balance stations, marked by dark dots in Figure 1.

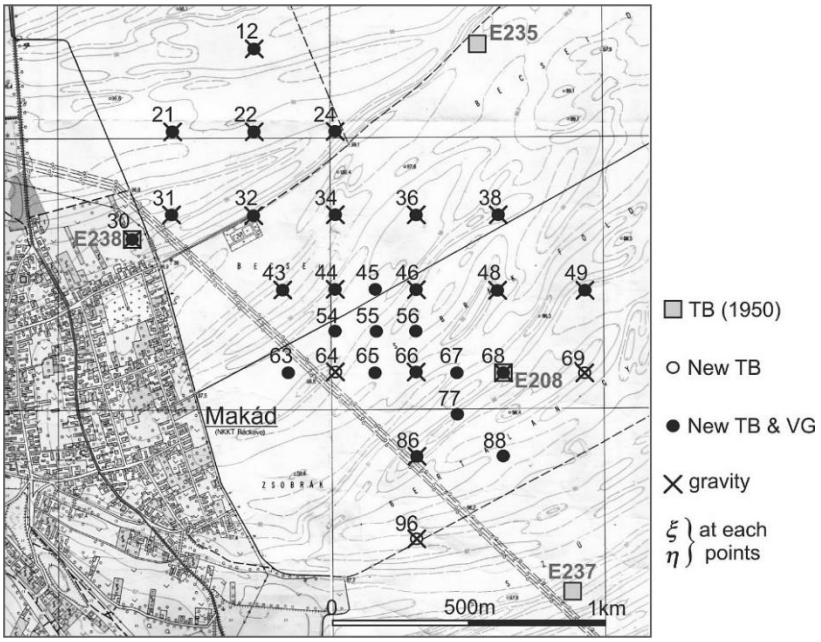

Figure 1

Torsion balance stations (marked by squares, circles, and dots), gravity measurements (marked by crosses), and vertical gradient measurements (marked by black dots) within the test area. Components ξ and η of vertical deflections are known at each point from the Hirt-model.

Deflections of the vertical have been determined for all points in the test area by the *Hirt-model* [12]. The GGMplus (Global Gravity Model plus) is constructed as a composite of data: 7 years of GRACE satellite data, 2 years of GOCE satellite, the

EGM2008 global gravity model, 7.5 arc-sec SRTM topography and 30 arc-sec SRTM30_PLUS bathymetry data, and includes North-South and East-West ξ, η components of deflections of the vertical. On the left and right side of Figure 2 ξ and η components of deflections of the vertical can be seen, respectively, in the GRS80 system in the test area (the isoline interval is 0.05 arcsec).

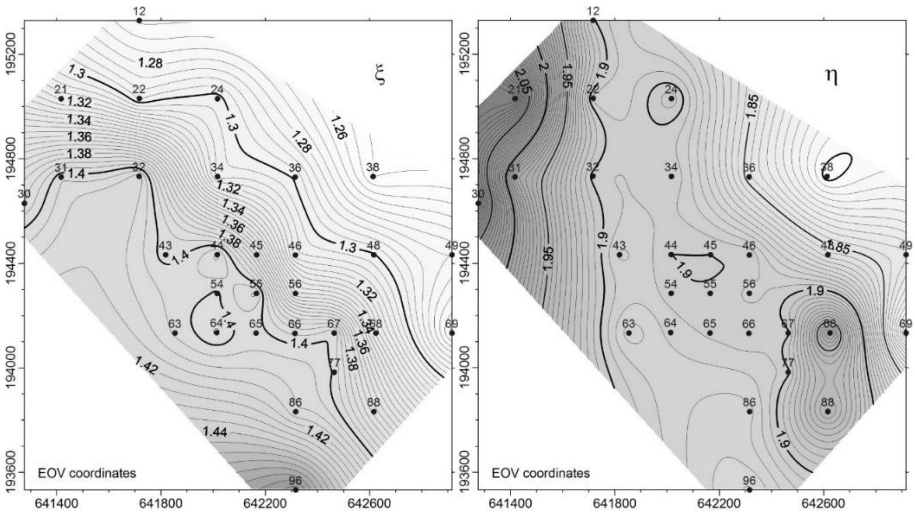

Figure 2
Vertical deflection components ξ and η within the test area from the Hirt-model. Contour interval is 0.05 arcsec

All the known horizontal gradients W_{zx} , W_{zy} , curvature data W_{xy} , W_{Δ} , vertical gradients W_{zz} and gravity values g were used as input data, but only a part of the known vertical deflection values were used as input data (as points for the training set) for the inversion; the remaining points (points of the validation set) were used for validating the computational results (15 points were considered for training, and 15 for the validation).

Our gravity and VG measurements are exremely accurate, but unfortunately torsion balance measurements have less accuracy. Vertical deflections originated from the Hirt-model [12] are available for each point, but it is important to emphasize that these are not real measurements – they do not contain the fine structure of the field, but are simply the results of a very accurate model computation. Taking this into consideration, different weights were applied for the input data: weights of the torsion balance measurements W_{zx} , W_{zy} , W_{xy} , W_{Δ} and the vertical deflection data were chosen to be 1 while the weights of gravity and VG measurements were chosen to be 10, as was the weight of the Laplace-equation.

In our solution, by substituting the computed expansion coefficients B_i from Eq. (49) into the expansion formulas (1)–(9), the potential function of the gravity field and all of its first and second derivatives were computed for the whole test area. Comparing measured and computed data, we obtained practically the same

horizontal gradients W_{zx} , W_{zy} , curvature data W_{xy} , W_{Δ} , vertical gradients W_{zz} and gravity values from the inversion as the input data of the measurements.

The relatively high spatial variations of gradients points to the need for high polinomial order in the series expansion represenation of the potential field. Our experience shows (similarly to our previous work [5]) that care should be taken in choosing the polynomial order, because when increasing its value the condition number of the normal equation increases rapidly. This can make parameter estimation (coefficients **B**) unreliable, with high estimation errors and strong correlation between some coefficients. It was earlier found that P = 18–24 can give a good compromise between resolution and stability [5], – and for this study P = 20 was applied in our computation.

From the 30 given vertical deflections 15 points were chosen as input data for the training set and are marked in Figure 3 by crosses; the remaining 15 points of the validation set as control points are marked by triangles. Our computational results are summarized in Table 1, where point number of the control points and the EOV *Y*, *X* coordinates in [m] can be found in the first three columns; then computed and given ξ , η components of the vertical deflections with their $\Delta\xi = \xi^{(comp)} - \xi^{(Hirt)}$ and $\Delta\eta = \eta^{(comp)} - \eta^{(Hirt)}$ differences can be found in the next six columns. Contour plots of $\Delta\xi$ and $\Delta\eta$ differences can be seen in Figure 3 at the same time (the contour interval is 0.05 arcsec in the figure).

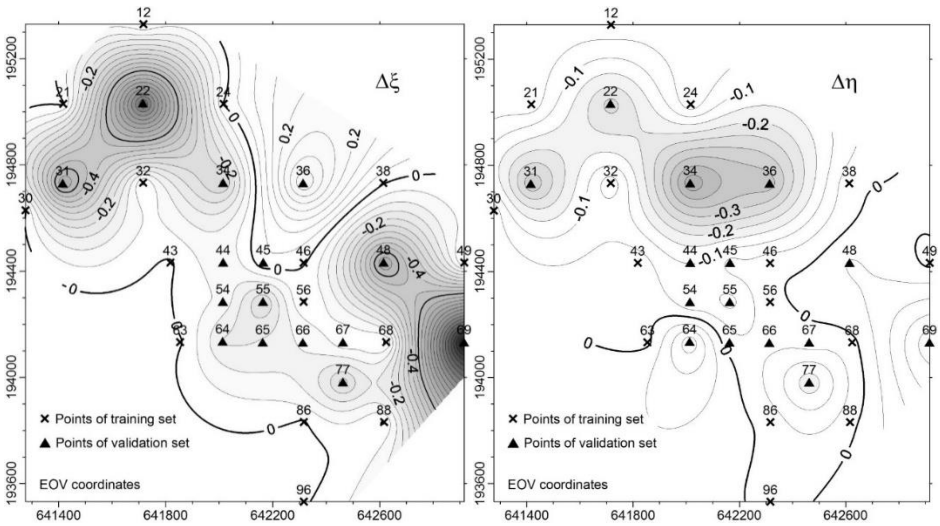

Figure3

Differences between the computed vertical deflection components by inversion and the given ξ and η determined by the Hirt-model within the test area. Points of training set are marked by crosses; points of validation set are marked by triangles.
Contour interval is 0.05 arcsec

Table1

Differences between computed and given vertical deflection data at the validation points

Point	Y [m]	X [m]	ξ (comp.) [arcsec]	ξ (Hirt) [arcsec]	Δξ [arcsec]	η (comp.) [arcsec]	η (Hirt) [arcsec]	Δη [arcsec]
31	641416.58	194729.93	0.79	1.40	–0.61	1.62	1.97	–0.35
34	642016.12	194732.41	1.00	1.31	–0.31	1.41	1.90	–0.50
36	642314.85	194730.44	1.70	1.30	0.41	1.47	1.85	–0.38
44	642015.85	194433.08	1.32	1.41	–0.09	1.80	1.90	–0.10
48	642615.88	194432.72	0.69	1.30	–0.61	1.91	1.86	0.05
64	642013.94	194135.08	1.24	1.39	–0.16	2.08	1.89	0.19
66	642313.68	194131.56	1.30	1.39	–0.09	1.87	1.90	–0.03
69	642915.90	194132.69	–0.04	1.26	**–1.30**	2.04	1.80	**0.24**
22	641716.60	195031.40	0.33	1.29	–0.96	1.62	1.89	–0.27
45	642166.00	194433.00	1.41	1.37	0.04	1.87	1.90	–0.03
54	642015.10	194284.80	1.34	1.40	–0.06	1.80	1.90	–0.10
55	642165.00	194285.00	1.15	1.41	–0.26	1.78	1.90	–0.12
65	642164.00	194132.70	1.26	1.40	–0.14	1.86	1.90	–0.04
77	642464.00	193983.00	1.12	1.40	–0.28	1.71	1.90	–0.19
67	642464.00	194133.00	1.38	1.40	–0.02	1.88	1.90	–0.02
				RMS=	**±0.36**		RMS=	**±0.16**

Root mean square (RMS) values of the differences between the vertical deflection components computed by inversion and ξ and η determined by the Hirt-model can be found in the last row of Table 1: $\mathrm{RMS}(\Delta\xi) = \pm 0.36''$ and $\mathrm{RMS}(\Delta\eta) = \pm 0.16''$. The largest error can be seen at Point 69, which is at the eastern edge of the test area, the most unfavorable place for the computation (generally extrapolation is much more unfavorable than interpolation). If we mit Point 69, the RMS values of $\Delta\xi$ and $\Delta\eta$ decrease significantly: $\mathrm{RMS}(\Delta\xi) = \pm 0.27''$, $\mathrm{RMS}(\Delta\eta) = \pm 0.15''$.

These results are quite good, compared with the accuracy of the measured vertical deflections by the QDaedalus system [8], which is about $\pm 0.1 - 0.3''$.

4. CONCLUSIONS

Inversion reconstruction of 3D gravity potential has been carried out here based on gravity data, torsion balance and vertical gradient measurements, including vertical deflection data. Computations were performed for a test area where gravity, torsion balance, vertical gradient measurements and vertical deflection data were available. Using the coefficients of a seriesexpansion of the gravity potential, both the first and the second derivatives of this potential were determined for the whole area by joint inversion.

In this study we focused on how this inversion method can be applied to the determination of vertical deflections. It can be seen that vertical deflections can be computed by this inversion method with $\pm 0.1 - 0.3''$ accuracy in our test area, which is the same as the accuracy of the vertical deflections measured by the QDaedalus system. Thus we have a very good possibility to compute vertical

deflections with suitable accuracy based on the large amount and good quality of gravity and gravity gradient data in Hungary.

5. ACKNOWLEDGEMENTS

Our investigations were supported by the National Scientific Research Fund, Project numbers OTKA K-076231 and OTKA K-109441.

6. LIST OF SYMBOLS

Symbol	Description
$A_{Pn}^{(i)}$	matrix elements at the P^{th} measurement point
B_n	coefficients of the series expansion
$\mathbf{d}$	vector of computed data
g	gravity constant
M	number of coefficients of the series expansion
N	number of measurements
$P(x_P, y_P, z_P)$	measurement point
U	normal potential
$W(x, y, z)$	gravity potential
W_{zx} , W_{zy}	horizontal gradients
W_{zz}	vertical gradients
W_{Δ} , W_{xy}	curvature data
$\boldsymbol{\varepsilon}$	discrepancy vector of measured and computed data
ξ , η	components of the deflection of the vertical
Ψ_1,Ψ_2,..., Ψ_P	set of basis function

7. REFERENCES

[1] VÖLGYESI, L.: Local geoid determinations based on gravity gradients. *Acta Geodaetica et Geophysica Hungarica*, 2001, 36, 153–162.

[2] VÖLGYESI, L.: Deflections of the vertical and geoid heights from gravity gradients. *Acta Geodaetica et Geophysica Hungarica*, 2005, 40, 147–159.

[3] VÖLGYESI, L.–TÓTH, GY.–CSAPÓ, G.–SZABÓ, Z.: The present state of geodetic applications of Torsion balance measurements in Hungary. *Geodézia és Kartográfia*, 2005, 57 (5), 3–12 (in Hungarian with English abstract).

[4] VÖLGYESI, L.–TÓTH, GY.–CSAPÓ, G.: Determination of gravity field from horizontal gradients of gravity. *Acta Geodaetica et Geophysica Hungarica*, 2007, 42 (1), 107–117.

[5] VÖLGYESI, L.–DOBRÓKA, M.–ULTMANN, Z.: Determination of vertical gradients of gravity by series expansion based inversion. *Acta Geodaetica et Geophysica Hungarica*, 2012, 47 (2),233–244.

[6] DOBRÓKA, M.–VÖLGYESI, L.: Inversion reconstruction of gravity potential based on torsion balance measurements. *Geomatikai Közlemények*, VIII, 2008, 223–230 (in Hungarian with English abstract).
[7] DOBRÓKA, M.–VÖLGYESI, L.: Inversion reconstruction of gravity potential based on gravity gradients. *Mathematical Geosciences*, 2008, 40 (3), 299–311.
[8] BÜRKI, B.–GUILLAUME,S.–SORBER, P.–PETER, O. H.: DAEDALUS: A Versatile Usable Digital Clip-on Measuring System for Total Stations. *2010 International Conference on Indoor Positioning and Indoor Navigation (IPIN)*, 15–17 September 2010, Zürich, Switzerland.
[9] TORGE, W.: *Gravimetry*. Walter de Gruyter, Berlin–New York, 1989.
[10] CSAPÓ, G.–ÉGETŐ, CS.–KLOSKA, K.–LAKY, S.–TÓTH, GY.–VÖLGYESI, L.:Test measurements by torsion balance and gravimeters in view of geodetic application of torsion balance data. *Geomatikai Közlemények*, 2009, XII, 91–100 (in Hungarian with English abstract).
[11] CSAPÓ, G.–LAKY, S.–ÉGETŐ, CS.–ULTMANN, Z.–TÓTH, GY.–VÖLGYESI, L.: Test measurements by Eötvös-torsion balance and gravimeters. *Periodica Polytechnica Civil Engineering*, 2009, 53 (2), 75–80.
[12] HIRT, C. S.–CLAESSENS, J.–FECHER, T.–KUHN, M.–PAIL, R.–REXER, M.: New ultra-high resolution picture of Earth's gravity field. *Geophysical Research Letters*, 2013, 40 (16), 4279–4283.

Geosciences and Engineering, Vol. 4, No. 6 (2015), pp. 93–104.

INVERSION OF WELL LOGGING MEASUREMENTS WITH A CONSTANT INTERVAL PARAMETER

LÁSZLÓ BALÁZS

Eötvös Loránd University, Department of Geophysics and Space Sciences
balazslaszlo@windowslive.com

Abstract. In the inversion of well logging measurement, some of the fitted parameters can be regarded as constant in a given depth interval at multiple measuring points (interval parameter or zone parameter). In most cases these parameters are related to the rock matrix or physical properties of formation water. To estimate the interval parameters, the measurements of the whole depth interval are inverted together using a common likelihood function. In this way the over determination and the degree of freedom increase but the other local parameters – which are independent in conventional inversion – are also linked in common inversion, resulting in correlations and hence equivalences as well. In this article the statistical effect of a common interval parameter is examined by analyzing the estimated parameter covariance matrix.

1. INTRODUCTION

In the traditional approach, the well logging data are interpreted depth by depth separately in the parameter fitting procedure, using separate minimization of statistical distance between measured and calculated log values. In some cases certain rock parameters can be regarded constant due to the layer structure, e.g. formation water resistivity (R_w) is practically constant in a water-bearing zone or reservoir, or if accumulated sediments have produced in constant environment, some matrix parameters can also be kept constant. Involving measurements at several depth points in the inversion may reduce the interval parameter uncertainty, but the statistical consequences – uncertainties, parameter correlations, bias – must be studied. A similar problem is faced with the so-called interval inversion introduced in [1]. In this approximation the coefficients of extension can also be regarded as an interval parameter. Joint inversion algorithms are also based on common parameters with the same difficulties [2].

2. THEORETICAL BACKGROUND OF COMBINED INVERSION

If during the petrophysical inversion a constant interval parameter (p_c) is assumed for the examined depth interval in addition to the local parameters (p_j), then a common, combined interval likelihood function (L) can be used in the inversion as a product of different depth point likelihood functions. If the measurements (ordered in matrix form: Y_{NxM}) are statistically independent, the combined, multi-depth-point likelihood function is:

$$L(\mathbf{Y},\mathbf{P}) = \prod_{j=1}^{M}\prod_{i=1}^{N} pdf_i\left(Y_{i,j}\middle|\mathbf{p}_j,\mathbf{p}_c\right) \tag{1}$$

The probability density function (pdf_i) is depends on the measurement error model for the i-th measurement. In the case of Gaussian error assumption, the maximization of unified likelihood function leads the weighted least square (Q) for all involved measurements as a parameter fitting criteria:

$$Q = \sum_{j=1}^{M}\sum_{i=1}^{N} w_i\left(Y_{i,j} - f_i\left(\mathbf{p}_j,\mathbf{p}_c\right)\right)^2 = \sum_{j=1}^{M} Q_j \tag{2}$$

The minimum of Q determines the fitted parameter vector in a so-called normal equation system:

$$\frac{\partial Q}{\partial P_{m,n}} = 0; m{:}1..M; n{:}1..K+J \tag{3}$$

In the case of a common interval parameter the weighted sum belonging to the given depth point (Q_j) may increase to achieve the overall minimum in Q functional. This means that the local parameter at given depth point may deviate from the value determined from the local minimum, but this deviation may correlate the deviation of parameter fitted at some other depth point. To determine the consequences of an interval fitting procedure the combined parameter covariance matrix has to be examined, and also the possible parameter biases, focusing on how uncertainty changes as a function degree of freedom, and parameter correlation as a source of possible equivalences.

2.1. The covariance matrix of fitted parameters

The customary Jacobian-matrix form, the measurement data matrix (Y) and parameter matrix (P) are converted to vector (y,p) row continuous form, as shown in Figure 1. In the parameter vector the last elements are the constant interval parameters.

Using the converted vector format the Jacobian-matrix (J) can be derived as a simple dyadic product:

$$\mathbf{J} = \mathbf{y} \circ \frac{\partial}{\partial \mathbf{p}} \tag{4}$$

The least square minimum can be derived from the vector equation, after linearization, expressed by Jacobian-matrix [3]:

$$\mathbf{J}^T\mathbf{W}\mathbf{y} = \mathbf{J}^T\mathbf{W}\mathbf{J}\mathbf{p} \tag{5}$$

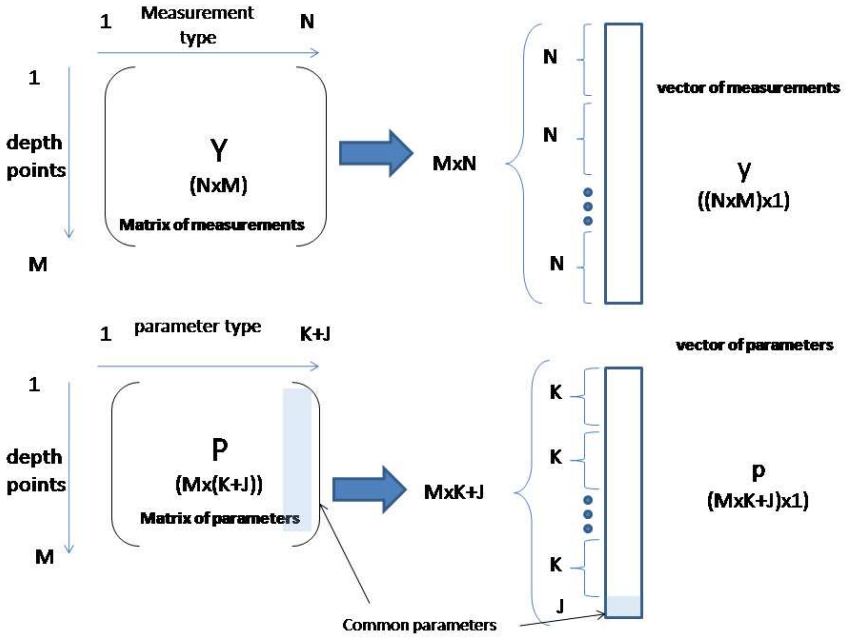

Figure 1
Measurement and parameter data matrix and vector form

To simplify the expressions the following notation is introduced:

$$\mathbf{R} = \mathbf{J}^T \mathbf{W}\mathbf{J} \tag{6}$$

The statistical variation of the parameter vector ($d\mathbf{p}$) and measurement vector ($d\mathbf{y}$) must also be related to Eq. (5). Finally the fitted parameter covariance matrix (C) can be derived as an expected value of $d\mathbf{p}$ based dyadics:

$$\mathbf{C} = (\mathbf{R})^{-1} \frac{Q_{\min}}{N \cdot M - M \cdot K - J} \tag{7}$$

Since the local parameters are regarded as independent from each other in the normal equation, the Jacobian- and R matrix has a special symmetry due to the off-diagonal zeros, and consequently the covariance matrix also inherits some special symmetry (Figure 2). In the figure the measurement weight matrix (W) is the identity matrix.

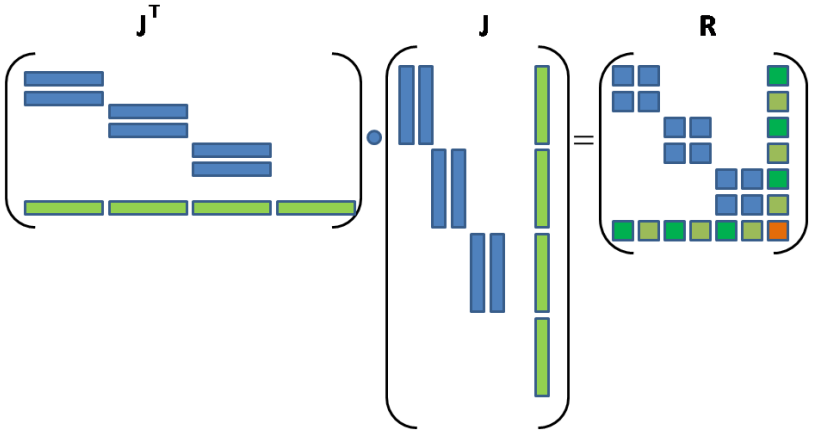

Figure 2
The symmetries of Jacobian and **R** matrix, in the case of one interval parameter (nonzero values are indicated by color code)

The "arrow shape" R matrix structure is the following, e.g. in the case of one local and one interval parameter for *M* depth point inversion:

$$R_{m,n} = \delta_{m,n} \cdot \sum_{i=1}^{N} J_{i,m} \cdot J_{i,n} + \left(\delta_{m,M+1} + \delta_{M+1,n}\right) \sum_{i=1}^{N} J_{i,m} \cdot J_{i,n} + \delta_{M+1,n}\delta_{m,M+1} \cdot \sum_{i=1}^{N} J_{i,M+1}^{2} \quad (8)$$

The arrow structure makes the derivation of matrix inverse easier. It can be easily proven that the inverse of R also inherits the arrow shape, but the off-diagonal elements are not zeros. This means that significant covariances may exist between local parameters as a consequence of combined inversion.

3. THEORETICAL EXAMPLE: LINEARIZED INVERSION PROBLEM

To demonstrate and examine the possible covariance between the local parameters, a simple two-parameter (per depth point) case is examined with one local (p_j) and one interval (p_c) parameter. The interval parameter is constant in the model calculations. The local parameter changes depth by depth. A simple linear measurement model with additive, zero mean measurement noise is used in the study:

$$Y_{i,j} = a_i \cdot p_j + b_i \cdot p_c + n_i \quad (9)$$

The coefficients may be the coefficient of a Taylor series. Using Eq. (6), the combined multi-depth-point R matrix with arrow shape can be expressed by the dot product of the coefficient vector of the measurement model.

$$R_{m,n} = \delta_{m,n} \cdot \langle a,a \rangle + \left(\delta_{m,M+1} + \delta_{M+1,n}\right) \cdot \langle a,b \rangle + \delta_{M+1,n}\delta_{m,M+1} \cdot (M) \langle b,b \rangle \quad (10)$$

For further simplification the symbol for a one-depth-point problem determinant is introduced:

$$Det_1 = \langle a,a \rangle \cdot \langle b,b \rangle - \langle a,b \rangle^2 \quad (11)$$

It has to be noted that parallel coefficient vectors cause singularity at matrix inversion due to the zero Det_1 value. The inverse of **R**, after some manipulation:

$$R^{-1}_{m,n} = \delta_{m,n} \cdot \frac{1}{\langle a,a \rangle} + \frac{\langle a,b \rangle^2}{M \cdot \langle a,a \rangle \cdot Det_1} - \left(\delta_{j,M+1} + \delta_{M+1,j}\right) \cdot \frac{\langle a,b \rangle}{M \cdot Det_1} + \delta_{M+1,n}\delta_{m,M+1} \cdot \frac{\langle a,a \rangle}{M \cdot Det_1} \quad (12)$$

From Eq. (12) the correlation between the interval and local parameters can be seen, as well as the fact that the local and another local parameter tend to zero with the depth point number (the second and third terms in Eq. (12)) as shown in Figure 3.

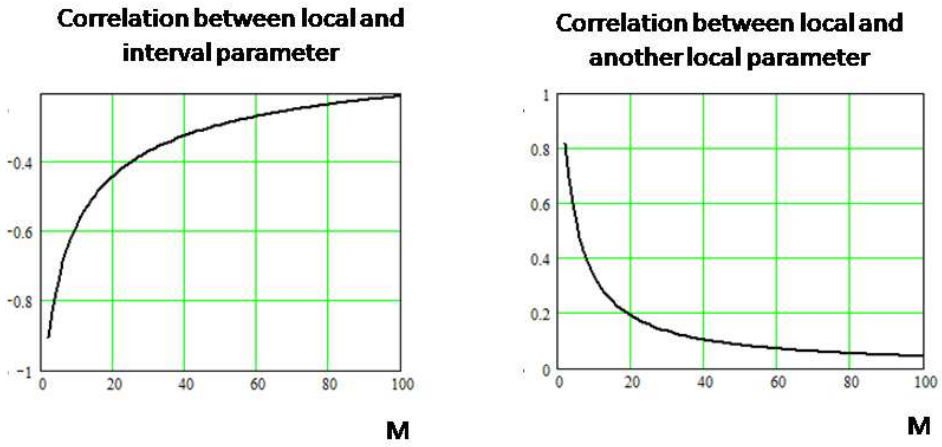

Figure 3
Changes in parameter correlation between local and interval parameters (left) and another local parameter (right) as a function of depth point number

The correlations also depend on the dot product of coefficient vector; if **a** and **b** are orthogonal, there is no parameter correlation. The standard deviation also decreases by the number of involved depth points, but the local parameter standard deviation is limited by the standard deviation value derived from the case where the interval parameter is exactly known. This asymptotic value is approached by the statistical convergence of the interval parameter (Figure 4).

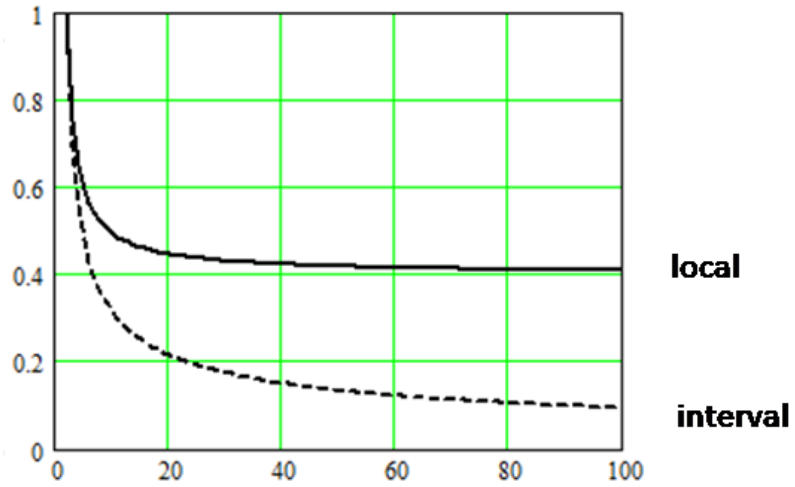

Figure 4
The relative decrease in parameter standard deviations by number of depth points

4. PRACTICAL EXAMPLE: SANDSTONE RESERVOIR

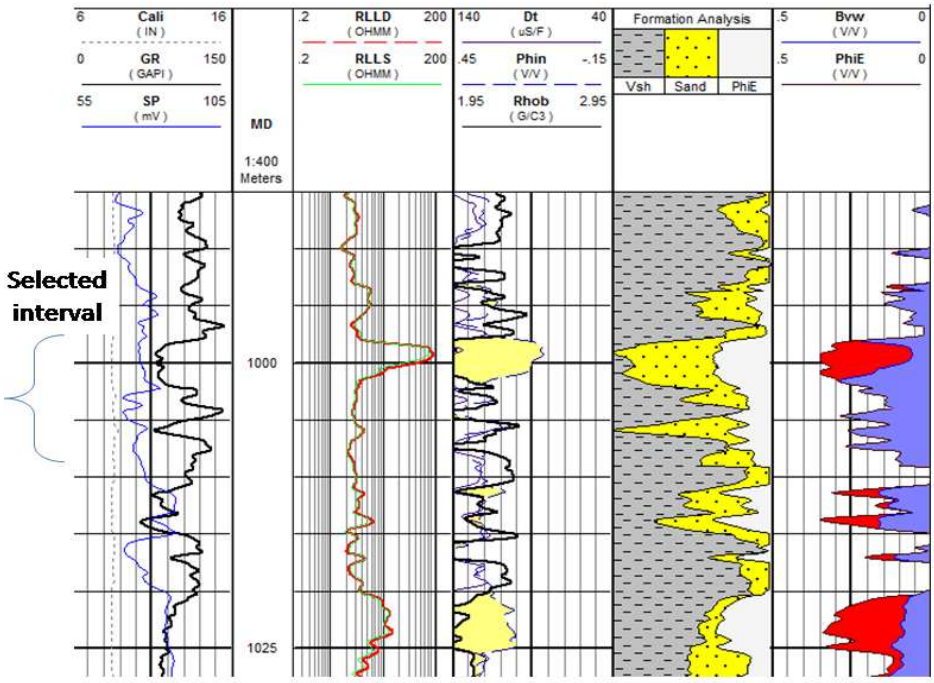

Figure 5
Well logs for a shaly-sandstone sequence at a gas reservoir, in the right tracks the petrophysical interpretation results are displayed

In this chapter the combined inversion method is applied for real well logs measured at a shaly-sandstone hydrocarbon reservoir interval. The logs and the results are displayed in Figure 5. The gamma ray, deep laterolog, neutron log and density log were used in the combined inversion. The basic petrophysical model equations defining the log response:

$$R_{LLD} \approx R_t = \frac{R_{sh}R_w}{V_{sh}R_w + (1-V_{sh})R_{sh}S_w^n \Phi^m} \tag{13}$$

$$GR = V_{sh}GR_{sh} + (1-V_{sh}-\Phi)GR_{ss} \tag{14}$$

$$\Phi_N = V_{sh}\Phi_{Nsh} + (1-V_{sh}-\Phi)\Phi_m + \Phi S_w \Phi_{Nw} + \Phi(1-S_w)\Phi_g \tag{15}$$

$$\rho = V_{sh}\upsilon_{sh} + (1-V_{sh}-\Phi)\rho_m + \Phi S_w \rho_w + \Phi(1-S_w)\rho_g \tag{16}$$

As described in the previous chapter, in the combined inversion the essential parameters – porosity (Φ), water saturation (S_w), shale volume (V_{sh}) as a local parameter, and formation water resistivity (R_w) as an interval parameter – were fitted in a selected reservoir region.

In this approach all of the petrophysical parameters of the examined depth interval are elements of a multidimensional random variable vector, and can be characterized by the expected value vector and covariance matrix. Due to the large number of depth points the standard deviation of local parameters approximates the asymptotics defined in Eq. (12). The decrement of interval parameter (R_w) standard deviation can be seen in Figure 6. The function is not as smooth as in the theoretical example, since the lithology changes feedback through the local parameters.

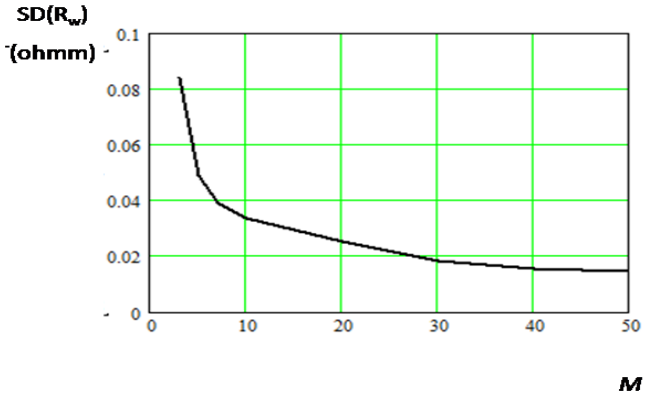

Figure 6
The standard deviation of interval parameter (Rw) as a function of depth point number

The results of inversion are displayed in Figure 7 and the related standard deviation also indicated. The estimated error strongly depends on the lithology.

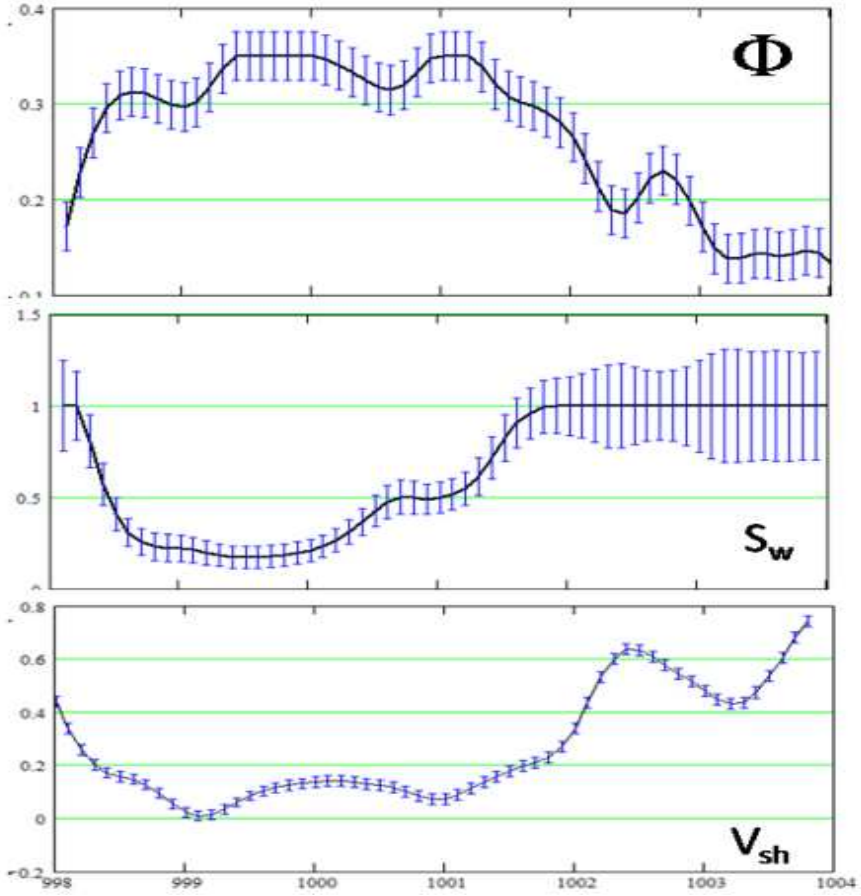

Figure 7
Interval inversion results (local parameters: porosity, water saturation, shale volume) and their standard deviations over the gas reservoir region, from 60 depth points

The parameter correlations are also examined. This correlation is not a real dependence between the parameters; it just follows from the measurement system and the way of inversion. A relatively high cross-correlation occurred between the formation water resistivity and other local parameters. The correlation depends on the local parameter values. The highest correlation can be seen in the high porosity reservoir region shown in Figure 8. The correlation of local parameters shown in Figure 9 is negligible due to the large number of involved depth points; higher correlations are only found for the local parameter belonging to the same depth point (at the reference depth of correlation).

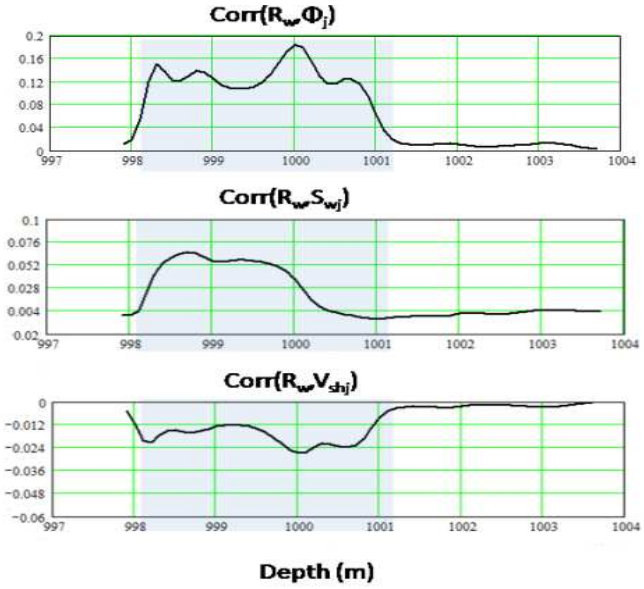

Figure 8
Cross-correlations between interval and local parameters at different depth points.
The reservoir region is highlighted

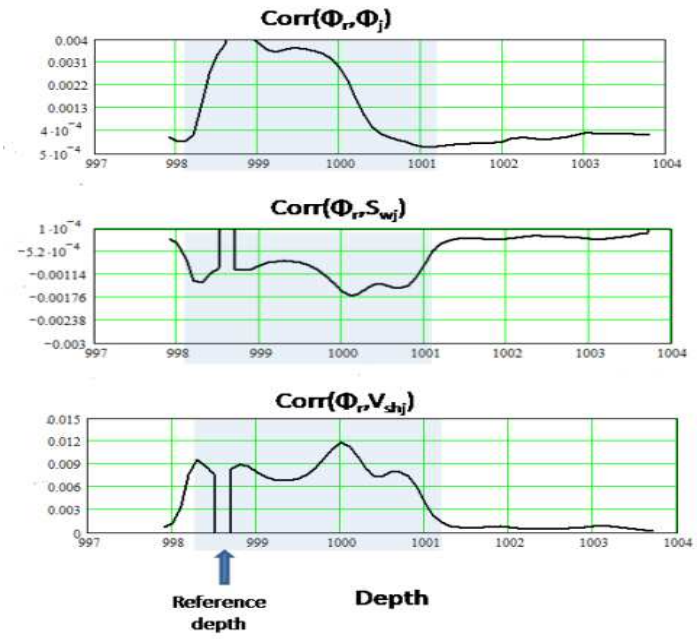

Figure 9
Cross-correlations between local parameters at different depth points.
The reference value for calculation was taken from the depth indicated by the blue arrow

5. FORCED INTERVAL PARAMETER

If the interval parameter is not really constant, fluctuates or slowly changes, just the equivalent value can be achieved in this combined inversion. For the statistical study of this inversion problem, a simple linear measurement model is applied again. The interval parameter real value (p_c) is now changing depth by depth:

$$Y_{i,j} = a_i \cdot p_j + b_i \cdot pc_j + n_i \tag{17}$$

but a constant parameter value (p_c) is assumed in the fitting function:

$$f(\hat{\mathbf{p}}) = a_i \cdot \hat{p}_j + b_i \cdot \hat{p}_c \tag{18}$$

The Jacobian-matrix in linear case does not depend on the parameters, therefore the **R** matrix is the same as it was in Eq. (10). Now the role of measurements is played by Eq. (17). Using Eqs. (17) and (18) in the normal equation, the following linear equation can be derived:

$$\mathbf{R}\hat{\mathbf{p}} = \mathbf{g} \tag{19}$$

where the elements of vector **g**:

$$g_j = p_j \cdot \langle a,a \rangle + pc_j \cdot \langle a,b \rangle \tag{20}$$

The last element in **g**:

$$g_{M+1} = \langle a,b \rangle \sum_{j=1}^{M} p_j + \langle b,b \rangle \sum_{j=1}^{M} pc_j \tag{21}$$

Applying the form of **R** inverse Eq. (12) to g vector, the expected value of estimated parameters can be calculated. After a short arrangement the parameter bias can be identified. The estimated local parameter at *j*-th depth point:

$$\hat{p}_j = p_j + \frac{\langle a,b \rangle}{\langle a,a \rangle} \left(pc_j - \frac{1}{M} \sum_{l=1}^{M} pc_l \right) \tag{22}$$

The bias term depends on the coefficient correlation and the local fluctuations of the forced interval parameter. That is, the changes in a parameter which is regarded constant in the interpretation cause bias in the local parameters.

Solving Eq. (19), the estimated equivalent value for interval parameter is the unbiased interval mean:

$$\hat{p}_c = \frac{1}{M}\sum_{j=1}^{M} pc_j \tag{23}$$

6. CONCLUSIONS

In well log interpretation, combined interval parameter inversion is a possible and efficient way to determine the local and interval parameters together. In this way the estimation degree of freedom can be increased, hence the variance of the estimated parameter can be reduced, especially the variance of interval parameters, which decreases with the number of involved depth points. By increasing the depth point number of inversion, the local parameter variances converge to the value which can be achieved when the interval parameter is exactly known.

The combined – multi-depth-point – interpretation may lead to correlations between fitted parameters. The correlation between the interval parameter and other local parameters is generally higher than the correlation between the local parameters of different depth points and depends on the Jacobian column vectors. The correlations generally decrease with the number of depth points involved.

If the interval parameter may change in the real layers but is forced to be constant in the interval inversion, this causes bias in the local parameters and the bias is proportional to the local fluctuation of interval parameter.

7. LIST OF SYMBOLS

Symbol	Description	Unit
a,b	Coefficient vectors in linear model	–
d**p**	Variation of parameter vector	–
d**y**	Variation of measurement vector	–
GR,GR_{sh},GR_{ss}	Gamma ray, Gamma intensity of shale and sand	GAPI
J	Jacobian-matrix	–
J	Number of interval parameters	–
K	Number of local parameters	–
L	Likelihood function	–
M	Number of depth points involved	–
m	Cementation exponent	–
N	Number of independent measurements	–
n	Saturation exponent	–
n_i	Noise vector for i-th measurement	–
R_w	Formation water resistivity	Ωm
p_c	Vector of interval parameter	–
p_j	*j*-th row of parameter matrix	–
P	Parameter matrix (Mx(K+J))	–
pdf_i	Probability density function of *i*-th measurement	–

Q	Weighted sum of squares	–
Q_j	Weighted sum of squares at *j*-th depth point	–
$\mathbf{R}$	$\mathbf{J^T WJ}$	–
R_t	True resistivity of formation	Ωm
R_{LLD}	Resistivity of deep laterolog	Ωm
S_w	Water saturation	–
SD	Standard deviation	–
V_{sh}	Shale volume	–
$\mathbf{Y}$	Measurement matrix (MxN)	–
$\mathbf{W}$	Weight matrix of measurements	–
w_i	Element of weight matrix	–
δ_{ij}	Kroneckerdelta	–
Φ	Porosity	–
Φ_n, Φ_{Nsh}, $\Phi_{Nw}\Phi_{Ng}$	Neutron porosity, shale, water and gas neutron porosities	–
ρ, ρ_{sh}, $\rho_{m,}$, ρ_g	Density, shale, matrix and gas densities	g/cm^3

8. REFERENCES

[1] DOBRÓKA, M.–SZABÓ, N. P.: Combined global/linear inversion of well-logging data in layer- wise homogeneous and inhomogeneous media. *Acta Geodaetica et Geophysica Hungarica* , 2005, 40 (2), 203–214.

[2] DRAHOS, D.–GYULAI, Á.–ORMOS, T.–DOBRÓKA, M.: Automated weighting joint inversion of geoelectric data over a two dimensional geologic structure. *Acta Geodaetica et Geophysica Hungarica*, 2011, 46, 309–316.

[3] SEN, M.–STOFFA, P. L.: *Global Optimization Methods in Geophysical Inversion*. Elsevier, Amsterdam, 1995.

Geosciences and Engineering, Vol. 4, No. 6 (2015), pp. 105–115.

MAGNETOTELLURIC EXPLORATION IN THE VICINITY OF IROTA AND GADNA

ENDRE NÁDASI[1]–ANDRÁS MADARASI[2]–ENDRE TURAI[1]

[1]*Department of Geophysics, University of Miskolc*
[2]*Geological and Geophysical Institute of Hungary*

Abstract. Magnetotelluric (MT) measurements were performed in the wooded area between Irota and Gadna. Irota is situated in the Cserehát region of NE Hungary. The main purpose of the measurements was to specify the depth of the Paleozoic basement and to identify occasional resistivity inhomogenities in the basement. Based on previous geological data, the area is prospected for base and precious mineralization. Mineral exploration of the area has been renewed in recent years, indicating the current significance of this work. The MT measurements were performed along three nearly parallel profiles. Data processing was carried out using WinGLink software. Apparent resistivity and impedance phase graphs were produced after the estimation of the impedance tensor. The nonlinear conjugate gradients algorithm was used for the 2D inversion of all three sections. A low resistivity zone is observable in the middle of the easternmost section. Based on the results of the inversion, geological conclusions were drawn. To make a complex interpretation and to understand the geological causes of the difference between the sections more precisely, further geophysical and geological investigations are needed.

1. INTRODUCTION

Raw materials have always been fundamental in human history. However, the technological revolution of our days has radically reshaped the list of strongly needed raw materials. The European Union decided to define a number of raw materials with a high economic importance to the EU combined with a high risk associated with their supply. Fourteen critical raw materials were specified in 2010. These are indispensable to the manufacture of high-tech products (LEDs, tiny electromotors, solar cells, catalysts, hybrid cars etc.). The research of these materials (in primary and in secondary resources) was the focus of the CriticEl project in Hungary. One of the target places of the project was an ore exploration area in the Cserehát area, NE Hungary, that has long been inactive [1].

Because the sought elements can be connected to sulphide mineralization, the delineation of a low resistivity zone seemed to be momentous regarding additional explorations. The magnetotelluric (MT) method proved to be the most effective tool to solve this problem and investigate the desired depth (500–600 m). The direct current (DC) sounding methods would have required extremely large current electrode distances, which would not have been cost effective. The main purpose of the measurements was to specify the depth of the Paleozoic basement and to identify occasional resistivity inhomogenities in the basement.

The MT subproject (as a part of the CriticEl project) was realized in cooperation with the Geological and Geophysical Institute of Hungary and the University of Miskolc (Institutional Department of Geology and Mineral Deposits, Institutional Department of Geophysics). The measurements were performed on three occasions during 2013 and 2014.

2. THE MAGNETOTELLURIC (MT) METHOD

Magnetotellurics is a natural field (passive) electromagnetic (EM) geophysical exploration method. The use of this method is based on the fact that the measured EM field depends not only on the strengths and other characteristics of the source, but also on the geoelectric structure of the earth. The fluctuations in the natural magnetic (H) and electric (E) fields are registered on the Earth's surface. The method can be applied for investigating the conductivity structure of the Earth at depth ranging from a few tens of meters to several hundreds of kilometers. The theoretical concept of exploration MT was first published by Tikhonov [2] in the USSR and, in more detail, by Cagniard [3] in France.

The MT signals have two main sources: global or regional lightning activity and the interaction between solar wind and the magnetosphere. The signals are very small in amplitude (tens of mV) and thus are easily distorted by man-made noises (power lines, railways) [4].

When the electromagnetic waves reach the Earth's surface, they can be reflected and penetrate into the ground. Because of the very high resistivity contrast between the air and the rocks, the EM wave passes vertically downward, so it is independent of the angle of incidence. In the subsurface of the Earth the energy and the amplitude of the wave begins to decrease exponentially. The quantity of the attenuation can be expressed by the absorption coefficient. It depends on the angular frequency (ω) and the electromagnetic properties (permittivity ε, magnetic permeability μ, conductivity σ) of the medium. The reciprocal of the absorption coefficient (a) is the skin depth (d_s), which expresses the penetration depth of the EM wave.

$$a = \sqrt{\frac{\mu\sigma\omega}{2}} \tag{1}$$

$$d_s = \sqrt{\frac{2}{\mu\sigma\omega}} \cong 500\sqrt{\rho T} \tag{2}$$

The connection between the horizontal electric (E_x, E_y) and magnetic field (H_x, H_y) components is described by the so-called impedance tensor [5].

$$\overline{E} = \underline{\underline{Z}} \cdot \overline{H} \quad ; \qquad \begin{bmatrix} E_x \\ E_y \end{bmatrix} = \begin{bmatrix} Z_{xx} Z_{xy} \\ Z_{yx} Z_{yy} \end{bmatrix} \cdot \begin{bmatrix} H_x \\ H_y \end{bmatrix} \tag{3}$$

The impedance tensor ($\underline{\underline{Z}}$) contains the information about the subsurface conductivity distribution. It depends on only the electromagnetic properties of the medium at a given frequency and is independent from the source of the EM field. Thus, it can be considered as the response function of the magnetotelluric method.

3. LOCATION, GEOLOGICAL SETTINGS

The exploration area is a wooded zone between Irota and Gadna villages, situated in the Cserehát area, NE Hungary (Figure 1). The Cserehát consists of metamorphosed Paleozoic rocks and Cenozoic sediments. A major sedimentary hiatus (Devonian–Miocene) is observable between them. The Paleozoic formations consist of mainly limestone and shale with notable graphite content. They underwent a low-grade (greenschist facies) metamorphism in the Cretaceous [6]. The Miocene-Pliocene sediments involve alternating sandstone, clay and silt layers.

A considerable geomagnetic anomaly was explored in the mid-20th century, in the vicinity of Irota. Uranium exploration started in the 1960s with a detailed exploration drilling program. Although uranium was not found in significant amounts, the exploration generated a great deal of important geological information. The analysis of core samples proved the presence of mostly pyrrhotite containing sulphide mineralization [7]. In addition, as a result of new geological observations, it is known, that the area is dissected by Neogene faults with significant downthrows [8]. Based on previous information, the area is being prospected for base and precious mineralization. Furthermore, REE minerals (monacite, xenotime) were described [1] in the near-surface young sediments.

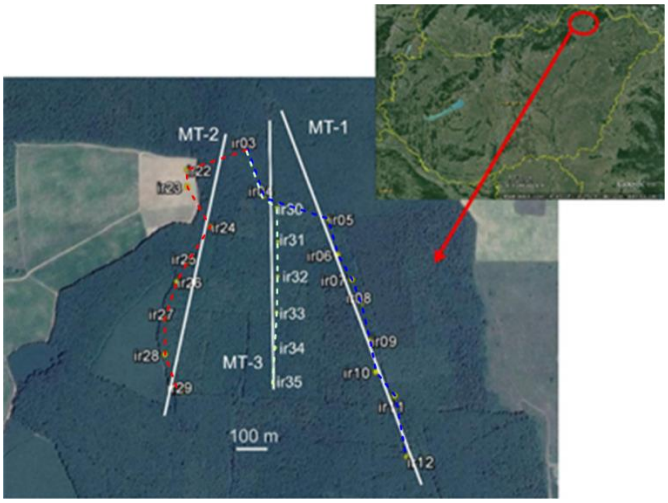

Figure 1
Satellite picture of the exploration area with the location of the measured points (ir03–ir12, ir22–ir29, ir30–ir35) and profiles of 2D inversions (MT-1, MT-2 and MT-3). Dashed lines indicate the original profile tracks

4. DATA ACQUISITION AND PROCESSING

MT measurements were performed along three profiles (MT-1, MT-2 and MT-3). MT signals were recorded at 24 stations (Figure 1) altogether. The measurements were carried out with a Metronix GMS-06 24-Bit MT-System. The recordings were registered in three frequency bands (LF1, free, LF2), with 4096, 512 and 64 Hz sampling frequencies, respectively. The registration time at one station was about one hour.

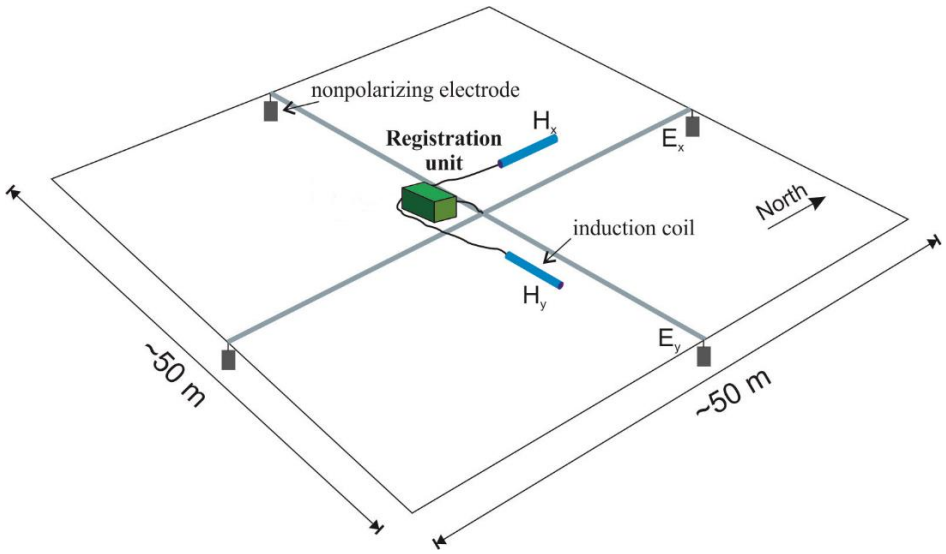

Figure 2
Simplified view of an MT station as deployed at the Irota exploration area

The magnetic field components were registered with induction coils, the electric components with non-polarizable Pb-Pb_2Cl_2 electrodes. The layout of the MT measuring system is outlined in Figure 2.

The basic task of the MT data processing is to determine the elements of the impedance tensor. There are two main types of processing methods: digital processing using time domain filters and statistical spectral (frequency) analysis [9]. Here the latter one is described.

Sign X_n the time series of the arbitrary component of the EM field, sampled at Δt interval (n = 1,2,…,N), where N is the number of sampling points. The real sign must have finite energy, therefore each record has to be transformed to zero series, as follows:

$$X_n^{(transformed)} = X_n - \frac{\sum_{n=1}^{N} X_n}{N} \tag{4}$$

After that, we form the autocorrelation ($R(H_x,H_x)$; $R(H_y,H_y)$) and cross-correlation ($R(H_x,H_y)$; $R(H_y,H_x)$; $R(E_x,H_x)$; $R(E_x,H_y)$; $R(E_y,H_x)$; $R(E_y,H_y)$) functions of the recordings. With the Δt interval, sampled time series of the two recordings are X_n and Y_n (n = 1,2,…,N), which should be correlated. In this case, the discrete correlation can be described with

$$R_k(X,Y) = \frac{1}{N-k}\sum_{n=1}^{N-k} X_n Y_{n+k} \tag{5}$$

If we correlate the horizontal EM field components with each other, for example the north-south direction electric component (E_x) with the west-east direction magnetic component (H_y):

$$E_x = Z_{xx}H_x + Z_{xy}H_y \ / \ \mathrm{corr}(H_y), \tag{6}$$

we will get the following equation:

$$R(E_x,H_y) = Z_{xx}R(H_x,H_y) + Z_{xy}R(H_y,H_y). \tag{7}$$

If we form the correlation of the same electric field component (E_x) and the other horizontal magnetic field component (H_x), we will receive a very similar equation:

$$R(E_x,H_x) = Z_{xx}R(H_x,H_x) + Z_{xy}R(H_y,H_x). \tag{8}$$

With the Fourier transform of the correlation functions, the power spectra of the recordings can be calculated:

$$S(H_x,H_x) = \mathrm{F}[R(H_x,H_x)] \qquad S(H_y,H_y) = \mathrm{F}\big[R(H_y,H_y)\big] \tag{9–10}$$
$$S(E_x,H_x) = \mathrm{F}[R(E_x,H_x)] \qquad S(E_x,H_y) = \mathrm{F}\big[R(E_x,H_y)\big] \tag{11–12}$$
$$S\big(E_y,H_x\big) = \mathrm{F}\big[R\big(E_y,H_x\big)\big] \qquad S(E_y,H_y) = \mathrm{F}\big[R(E_y,H_y)\big] \tag{13–14}$$
$$S\big(H_x,H_y\big) = \mathrm{F}\big[R\big(H_x,H_y\big)\big] \qquad S(H_y,H_x) = \mathrm{F}\big[R(H_y,H_x)\big] \tag{15–16}$$

Based on this, the above presented Eqs. (7)–(8) will be:

$$S(E_x,H_y) = Z_{xx}S(H_x,H_y) + Z_{xy}S(H_y,H_y) \tag{17}$$
$$S(E_x,H_x) = Z_{xx}S(H_x,H_x) + Z_{xy}S(H_y,H_x). \tag{18}$$

They can be handled as a system of linear equations. Expressing Z_{xx} from one of these equations and substituting it into the other equation, Z_{xy} can be calculated. Similarly, if Z_{xy} is expressed and substituted into the other equation, Z_{xx} can be

derived. The correlation of the other electric field component (E_y) with both magnetic field strengths (H_x, H_y) will result in an equation system from which the Z_{yx} and Z_{yy} can be expressed.

$$S(E_y, H_y) = Z_{yx} S(H_x, H_y) + Z_{yy} S(H_y, H_y) \tag{19}$$

$$S(E_y, H_x) = Z_{yx} S(H_x, H_x) + Z_{yy} S(H_y, H_x)\,. \tag{20}$$

Performing the above-presented method, the elements of the impedance tensor can be derived from the power spectra as a function of the frequency:

$$Z_{xx}(f) = \frac{S(E_x,H_x)S(H_y,H_y) - S(H_y,H_x)S(E_x,H_y)}{S(H_x,H_x)S(H_y,H_y) - S(H_y,H_x)S(H_x,H_y)} \tag{21}$$

$$Z_{xy}(f) = \frac{S(H_x,H_x)S(E_x,H_y) - S(E_x,H_x)S(H_x,H_y)}{S(H_x,H_x)S(H_y,H_y) - S(H_y,H_x)S(H_x,H_y)} \tag{22}$$

$$Z_{yx}(f) = \frac{S(E_y,H_x)S(H_y,H_y) - S(H_y,H_x)S(E_y,H_y)}{S(H_x,H_x)S(H_y,H_y) - S(H_y,H_x)S(H_x,H_y)} \tag{23}$$

$$Z_{yy}(f) = \frac{S(H_x,H_x)S(E_y,H_y) - S(E_y,H_x)S(H_x,H_y)}{S(H_x,H_x)S(H_y,H_y) - S(H_y,H_x)S(H_x,H_y)} \tag{24}$$

The WinGLink MT data processing software follows this statistical spectral analysis, but it uses an extra accuracy and stability increasing method published by Sims et al. [10]. It calculates the main impedances (Z_{xy}, Z_{yx}) four different ways and accepts the expected value of these as a final result.

After the estimation of the impedance tensor, the apparent resistivity and impedance phase can be derived as follows:

$$\rho_a = \frac{1}{\mu\omega}\left|Z_{ij}\right|^2 \text{ [ohmm] (i,j = x,y)} \tag{25}$$

$$\varphi_{ij}(\omega) = arctg\left(\frac{\mathrm{Im}(Z_{ij}(\omega))}{\mathrm{Re}(Z_{ij}(\omega))}\right) \text{ [rad] (i,j = x,y)} \tag{26}$$

5. RESULTS

Apparent resistivity and impedance phase graphs were produced after the estimation of the impedance tensor. The impedance tensors were rotated into profile direction. These formed the input parameters for the 2D inversion. The nonlinear conjugate gradients algorithm [11] was used for the 2D inversion of the three sections.

It can be seen on the MT-1 section shown in Figure 3 that the Paleozoic Basement can be found in a deeper and deeper position southward. In the Palezoic basement – which can be considered as an insulator – an extremely well conducting rock body appears (Figure 3). This zone probably contains sulphide mineralization, according to drillhole information (Fv-1, Gad-1) [1]. The top of this conductive body can be

found at 500 m depth. From the succession of the Felsővadász-1 well the depth of the Paleozoic Basement was extrapolated along the section.

As we can see in Figure 3, the resistivity of the Paleozoic Basement is about 100–200 Ωm on the figure of the MT-1 section. However, it decreases below –300 m (above sea level) and can be lower than 50 Ωm. Above the boundary of the Neogene and Paleozoic rocks, additional lower resistivity zones can be observed. They can signal shaly or weathered sedimentary units.

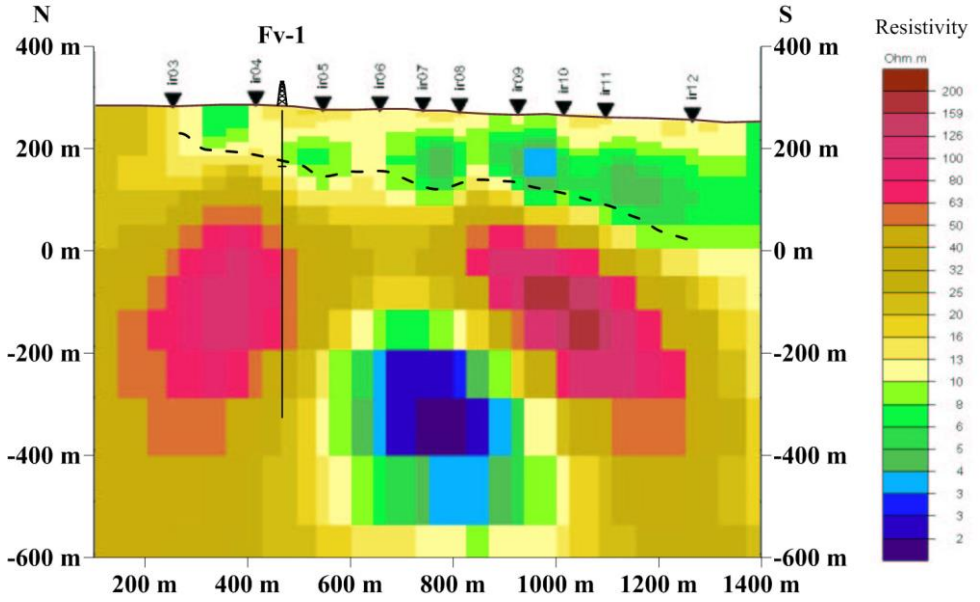

Figure 3

2D inversion model of the MT-1 section. Fv-1 indicates a borehole, which penetrated pyrrhotite-bearing zones. The dashed line indicates the Paleozoic basement, the boundary of the Neogene and Paleozoic rocks

The aim of the investigation in the MT-2 (ir22-ir29) section was to find the continuation of the low resistivity zone that was recognized in the MT-1. It was confirmed after the evaluation of MT-2 that no similarly well-conducting zone can be found in the MT-2 section (Figure 4). To clarify the cause of the very different resistivity distribution under the two profiles, the MT-3 profile was measured between the two sections.

On the 2D resistivity picture of the MT-2 and MT-3 sections (Figures 4 and 5), a relatively high resistive (above 100 Ωm) and thick (200–300) body appears. This means that the low resistivity zone of the MT-1 section does not have continuity towards the west. The northern part of the MT-2 and MT-3 sections was complemented with the ir03 and ir04 stations. These belong originally to the MT-1 profile.

It can be observed in Figure 4 that the deepening of the basement southward is not as characteristic as in the case of the MT-1 section. Interestingly, the horizontal resistivity map in Figure 6 raises the possibility of a SSW-NNE direction fault zone.

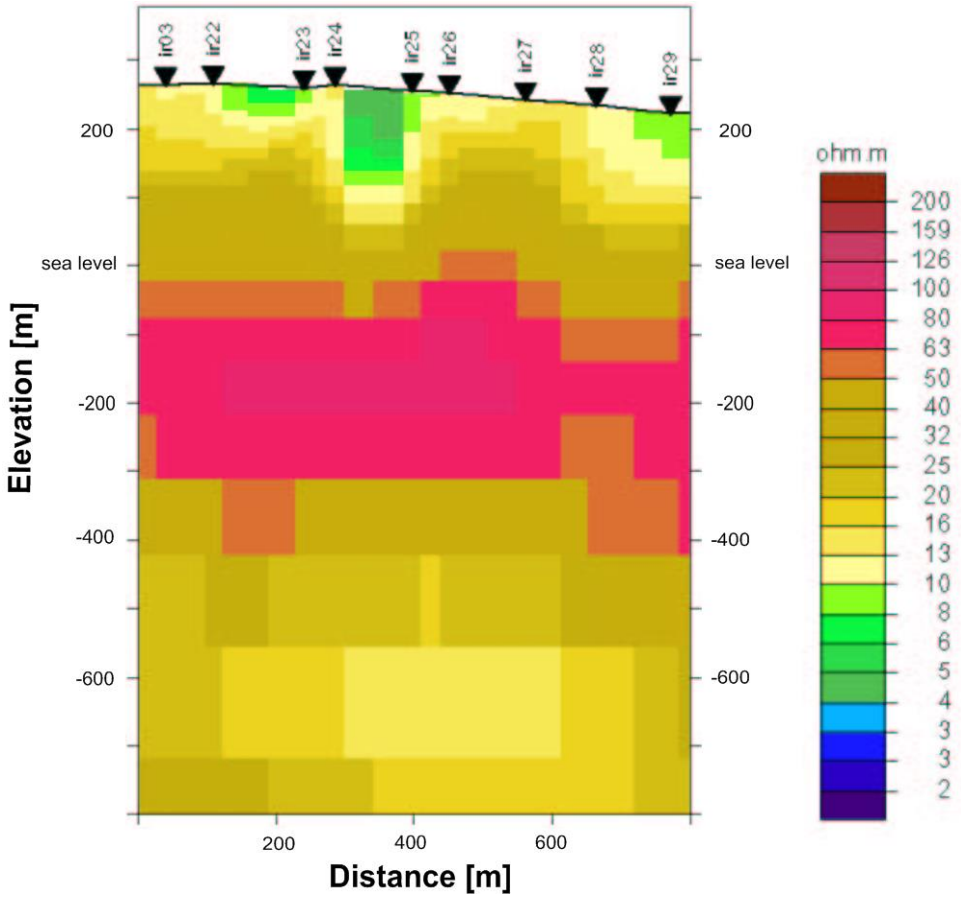

Figure 4
2D inversion model of the MT-2 section

6. CONCLUSION

A significant low resistivity zone appears clearly on the image of the MT-1 profile, at a depth of about 400–500 meters under Stations ir06, ir07 and ir08. The image of the middle (MT-3) section is quite different; a relatively high resistivity zone is observable there.

Since the low resistivity zone does not appear on the 2D inversion image of the western (MT-2, MT-3) profiles, the anomaly may continue towards east. It is also conceivable that the anomaly does not link to a structural fault, but is the manifestation of a local post volcanic effect. In this case, the extension of the low resistivity unit may not be so significant.

To find the geological cause (sulphide, graphite, clay mineralization) of this anomaly (MT-1) and to clarify the geometry of the low resistivity body, further geophysical and geological investigations (especially exploration drilling) are needed. In addition, the application of the induced polarization (IP) method has to be taken into consideration, because of the presence of pyrrhotite. With the measuring of the MT-3 profile, it became possible to build a 3D geophysical model. This has a great importance, because the geoelectric structure of the exploration area shows a significant 3D effect, therefore the 2D approximation is uncertain.

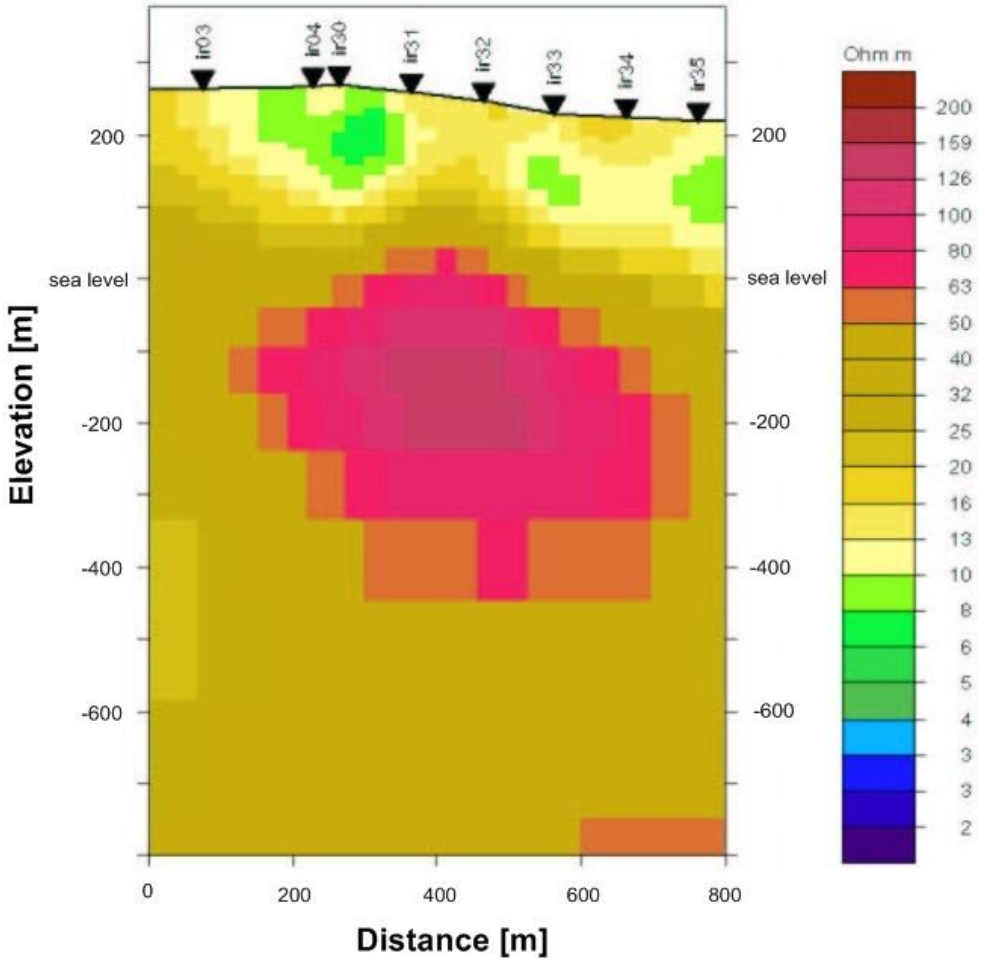

Figure 5
2D inversion model of the MT-3 section

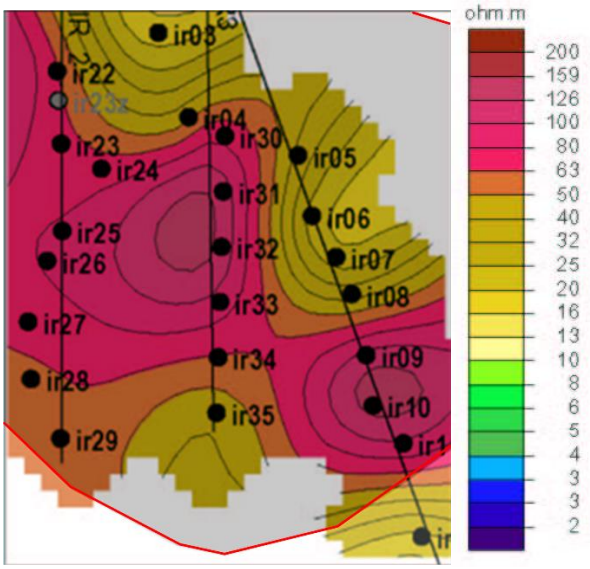

Figure 6
Horizontal distribution of the resistivity, 100 m below sea level. The magnetic anomaly (bordered with red line) covers almost the whole MT exploration area [12]

The assumed hydrothermal system can modify the physical parameters of the rocks strongly. In this case, the magnetic susceptibility has been increased (pyrrhotite enrichment), and the resistivity has been increased (silification) or decreased (clay mineralization). In the inversion, we could not take into consideration the induced polarization phenomenon. Furthermore, our model supposes an isotrope medium, but the succession has petrological anisotropy, which influences the electromagnetic wave propagation.

These factors increase the uncertainty of the interpretation. To create a more reliable geological model, further information (IP, seismic and drilling) should be taken into consideration. The next key step of this MT project is to make 3D inversion with the data from the 24 stations.

7. ACKNOWLEDGEMENTS

We are grateful to Szabolcs Tóth, Marcell Szilvási and Recep Güney for their help in the field measurements.

This work was carried out as part of the TÁMOP-4.2.2.A-11/1/KONV-2012-0005 project in the framework of the New Széchenyi Plan supported by the European Union, co-financed by the European Social Fund.

8. LIST OF SYMBOLS

Symbol	Description	Unit
a	absorption coefficient	1/m
d_s	skin depth	m
$\overline{\mathbf{E}}$	electric field intensity vector	V/m
$\overline{\mathbf{H}}$	magnetic field intensity vector	A/m
f	frequency	Hz
ω	angular frequency	rad/s
σ	conductivity	S/m
μ	magnetic permeability	H/m (Vs/Am)
ε	permittivity	F/m
φ	impedance phase	degree
ρ	resistivity	ohmm
ρ_a	apparent resistivity	ohmm
$\underline{\underline{Z}}$	impedance tensor	–

9. REFERENCES

[1] FÖLDESSY, J.: Basic research of the strategic raw materials in Hungary. *CriticEl Monography series 10*, Miskolc, 2014.

[2] TIKHONOV, A. N.: On determining electrical characteristics of the deep layers of the Earth's crust. *Doklady*,1950, 73, 295–297.

[3] CAGNIARD, L.: Basic theory of the magnetotelluric method of geophysical prospecting. *Geophysics*, 1953, 18, 605–635.

[4] SIMPSON, F.–BAHR, K.: *Practical Magnetotellurics*. University Press, Cambridge, 2005.

[5] CANTWELL, T.: *Detection and Analysis of Low-Frequency Magnetotelluric Signals*. PhD Thesis, Massachusetts Institute of Technology, Cambridge, Massachusetts, 1960.

[6] ÁRKAI, P.: Low-grade metamorphism of Paleozoic sedimentary formations of the Szendrő Mountains (NE-Hungary). *Acta Geologica Academiae Scientarium Hungaricae*, 1977, 21/1–3, 53–80.

[7] CSÁKI, F.: *Complex geological investigation of the Paleozoic formations in the Cserehát* (in Hungarian). Doctoral thesis, Eötvös Loránd University, 1976.

[8] NÉMETH, N.: Geological observation in the Cserehat between Irota and Gadna. *Geosciences and Engineering*, 2012, 1 (1), 261–269.

[9] TURAI, E.: Magnetotelluric data processing (in Hungarian). Lecture notes, University of Miskolc, 1986.

[10] SIMS, W.E.-BOSTICK, F.X.-SMITH, H.W.: The estimation of magnetotelluric impedance tensor elements from measured data. *Geophysics*, 1971, 36, 938-942.

[11] RODI, W.-MACKIE, R.L.: Nonlinear conjugate gradients algorithm for 2-D magnetotelluric inversion. *Geophysics*, 2001, 66, 174-187.

[12] CZEGLÉDI, B.: Joint evaluation of the exploration data, geochemical and geophysical relationship of the Gadna-Irota area (in Hungarian). MSc Thesis, University of Miskolc, 2013.

Geosciences and Engineering, Vol. 4, No. 6 (2015), pp. 116–124.

THE IMPROVEMENT OF THE REGIONAL FLOW MODEL OF THE TOKAJ MOUNTAINS WITH THE HELP OF GEOPHYSICAL INVERSION METHODS

PÉTER SZŰCS[1,2]–ZOLTÁN FEJES[1]–BALÁZS ZÁKÁNY[1]–
FERENC SZÉKELY[1]–ENDRE TURAI[1]–ÁKOS GYULAI[1]–
NORBERT PÉTER SZABÓ[1]–MÁTYÁS KRISZTIÁN BARACZA[1]

[1] *Faculty of Earth Science and Engineering, University of Miskolc*
[2]*MTA–ME Research Group of Geoengineering*
hgszucs@uni-miskolc.hu

Abstract. The WELL aHEAD Project has realized the first regional-scale complex hydrogeological study of the Tokaj Mountains. The complex geology of this region was well known, but a general hydrogeological description did not exist. Based on the derived information, a regional scale flow model has been built to understand the regional flow systems of the Tokaj Mountains. This is the first time that the water budget can also be estimated to provide valuable information for groundwater management measures. Different geophysical methods gave the opportunity to refine the modeling activity in order to receive better calibration results during the trial and error inversion procedure. As a result, it can be concluded that valuable drinking and thermal water resources are available in the Tokaj Mountains, and can be the basis of future developments.

1. INTRODUCTION

The Tokaj Mountain range, located in the north-eastern part of Hungary – part of the Carpathian Basin – is one of the most famous volcanic mountain ranges of Hungary. It strikes north-south and is approximately 100–120 km long. The mountains run between Tokaj and Eperjes (Slovakia) [2]. Thermal and geothermal research in the Tokaj Mountains has always been of secondary importance from the point of view of hydrogeology, due to its complex geological structure and the insufficient number of deep exploration wells. During our research we learned that several potential thermal aquifers may be found in the investigated area despite the complex geological structure. Many wells in the mountains produce good quality outflow water with a high amount of total dissolved solids. Data was collected about various groundwater parameters, then a hydrogeological-hydrochemical database was built, which serves as the basis of the regional hydrogeological research.

2. THE GEOLOGICAL SETTINGS

The investigated area was defined mainly by natural boundaries. The boundary in the North is the Hungarian-Slovakian border, while the western boundary runs along the Hernád Valley, which is a north-northeast south-southwest structural line, known also as the ALCAPA-Tisza tectonic line, a part of the Central Hungarian lineament.

The southern boundaries of the area are the Tisza and the Sajó Rivers. Finally, the eastern borders are the Tisza and the Bodrog Rivers.

The geological structure of the Tokaj Mountains is rather complicated. The depth and the rock material of the basement are still in question. Some basement maps show that it is approximately at 1500–2000 m deep and the material of the basement is probably metamorphic mica [3]. Concerning the geological structure of the investigated area, it has been proved in the thermal karst of Sárospatak and Bükk that shallow marine carbonate sediments were also deposited in the Triassic [4]. Neogene vulcanite formations settled on the basement with hundreds or in some places thousands of meters in thickness. The reason for the extraordinary thickness is that volcanism started in the Miocene and ended in the Lower Pannonian. The Pannonian Lake gradually lost its salinity and was filled by river drift. The Upper Pannonian clastic sediments pinched out on the southern part of the research area, but toward the Great Hungarian Plain their thickness increases. In several areas above the Pannonian layers Pleistocene fluvial sediments settled in great thickness, where Holocene formations are negligible. Figure 1 shows the geological model of the Tokaj Mountains.

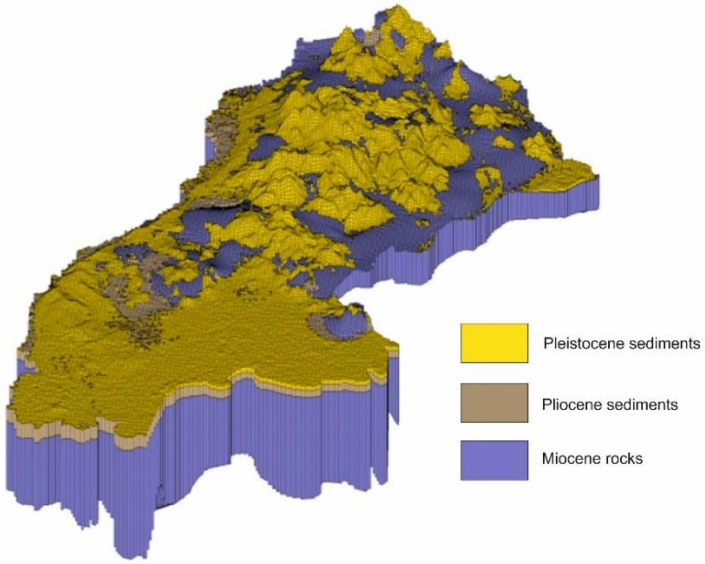

Figure 1
Geological model of the Tokaj mountains

3. THE GROUNDWATER RESOURCES OF THE INVESTIGATED REGION

The hydrogeology of the research area is very diverse and complex, like its geological structure. We have classified the groundwater bodies by the 2010 Watershed Management Plan (WMP). The WMP divides the Tokaj Mountains into two parts: the northeastern part is the Tokaj Foothills and the southwestern part is

the watershed of the Hernád and Takta rivers. Four groundwater body types can contain potential hot water aquifer formations. Table 1 shows the groundwater bodies in the research area.

Table 1

Potential warm water aquifers in Tokaj Mountains [4]

Type of groundwater body	**Name of area**	**Surface**
Mountainous	Zemplén Mountains–Hernád Watershed Zemplén Mountains–BodrogWatershed	504,1 km^2 615,1 km^2
Porous	Sajó–Hernád Valley Sajó–Takta Valley, Hortobágy Bodrogköz	458,2 km^2 303,1 km^2 61,9 km^2
Porous thermal	Basins of the Northern Mountains Northern Great Plains	1142,6 km^2 28,7 km^2
Thermal karst	Thermal karst in Sárospatak Thermal karst in the Bükk Mountains	62,2 km^2 174.3 km^2

The wells in the southern part of the research area are dominantly screened to the porous aquifers (Pleistocene and Pannonian layers) and the thicknesses of these layers increase to the South; therefore, the effluent water temperature also increases. These Pleistocene and Pannonian formations are excellent aquifers, consisting of high porosity sediment layers with good porosity and excellent aquifer properties, but they are too shallow, and the geothermal gradient cannot prevail. Only in the southern parts of the area did the Pannonian layer reach a sufficiently large depth to provide hot water. Within the research area the main aquifers are Pleistocene sands and Upper Pannonian sand and gravel. The yield of these aquifers is high and increases with depth, but the recharge of the wells is limited, due to the poor infiltration conditions from the mountainside. The groundwater level can dramatically decrease because of the inadequate production rates of the wells. (In the case of Prügy Waterworks, the dynamic water level depression was 43 m!). In spite of favorable hydrological and geothermal conditions, only a few deep wells have been drilled in the south part of the investigated area. In Kesznyéten and Girincs the depth of the wells did not reach 100 m, but the bottom of the Upper Pannonian formation is at more than 1000 m depth. The most significant Neogene aquifer formations are the cracked tuff layers, in which the water flows in a rift system to the wells. The greater part of the Tokaj Mountains was formed from high and medium strength porous Miocene (Tertiary) volcanic rocks and debris. These rocks have medium hydraulic conductivity. The lava rocks (rhyolite, dacite, and andesite) and tuffs store fissure water, with their hydraulic conductivity depending on the fracture system [3].

4. THE REGIONAL FLOW MODEL OF THE TOKAJ MOUNTAINS

The main objective of this regional scale groundwater flow model is to give the water budget of the investigated volcanic area and to understand the underground flow systems in the deep fractured aquifers. The USGS MODFLOW program package was applied to simulate groundwater flow in the Tokaj Mountains. The calibrated flow model is now capable of simulating different water management scenarios concerning drinking, mineral, medicinal and even thermal water resources. There is a strong need in these regions for mineral and thermal water resources to develop the touristic infrastructure. The realization of the model grid was a real challenge because the investigated region is a volcanic area, where the main rock is the andesite and volcanic tuff. A large background database was built to provide reliable values for the model data (geophysical, drilling deep layer lines etc.) and some other important parameters (hydraulic conductivity, porosity, infiltration data etc.). The model involved fractured zones, natural infiltration, recharge and discharge areas etc.

The creation of the surface of the top layer was based on satellite images using GIS, as shown in Figure 2. The estimated position of the basement was determined by geophysical basement maps (Figure 3).

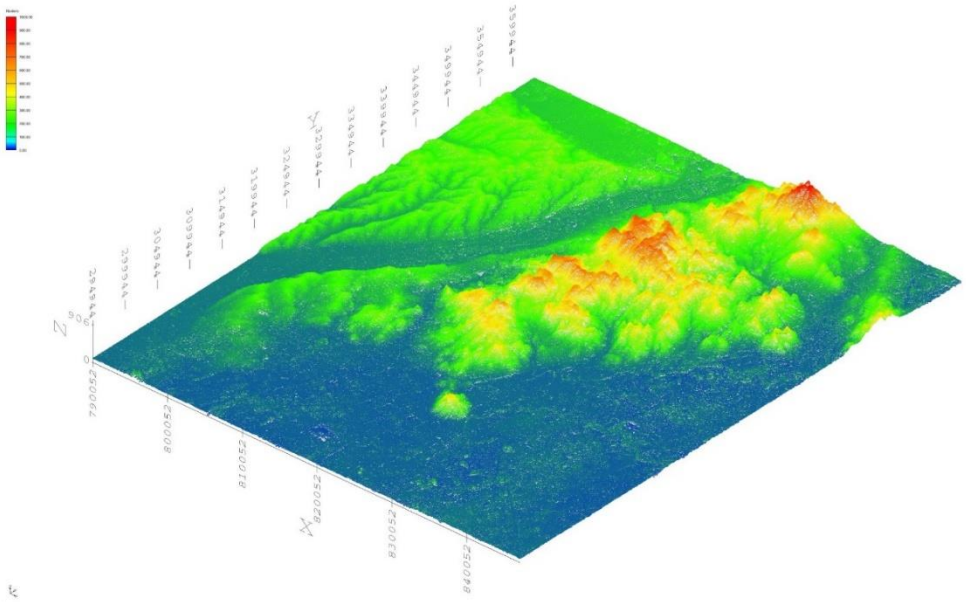

Figure 2
Surface of the Tokaj Mountains in the Groundwater Modeling System (GMS) program

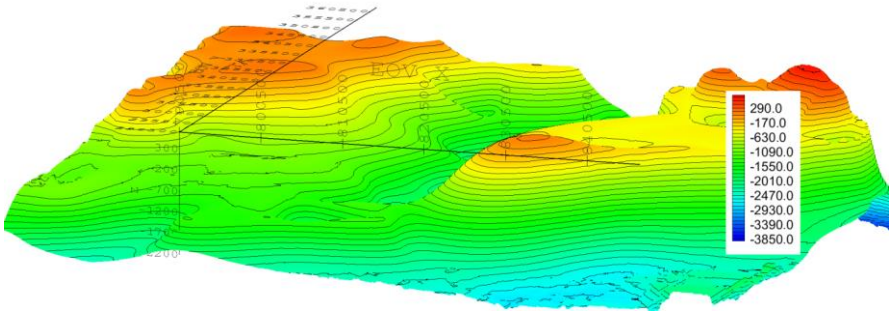

Figure 3
3D digitized image of the surface of the basement

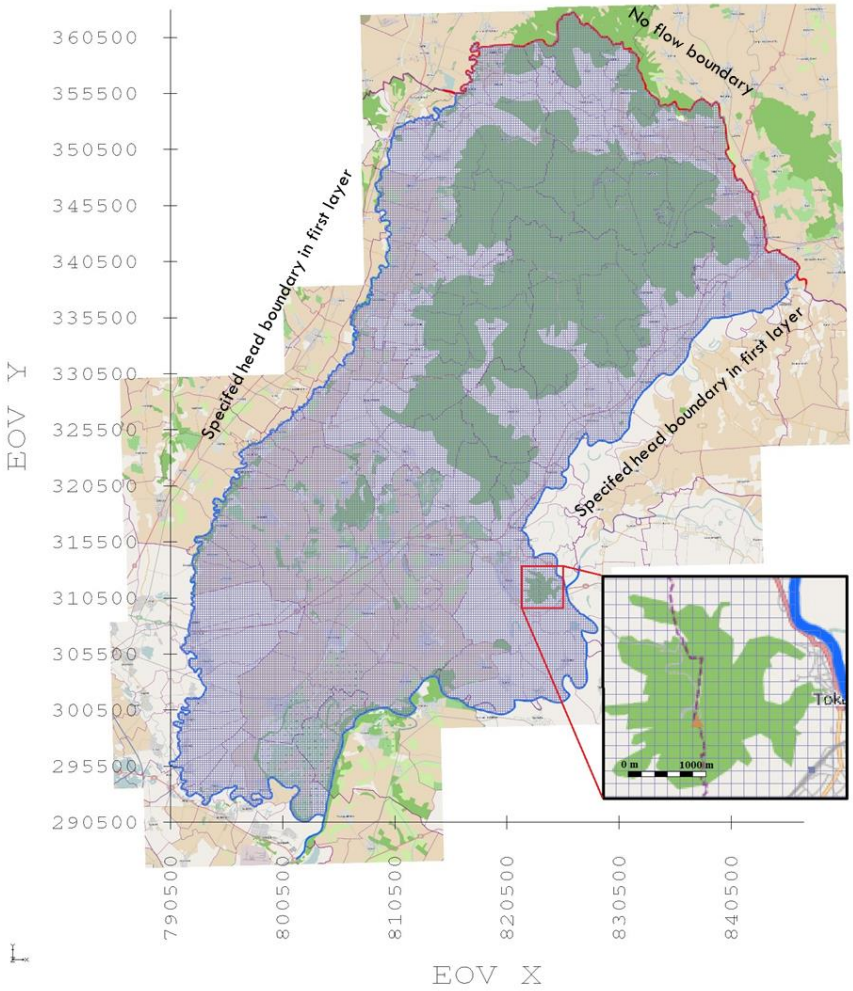

Figure 4
Grid and boundary conditions used in the model

The geophysical basement maps were generated on the basis of 173 pieces of borehole information. Three hydrogeological layers (Pleistocene, Pannonian, Miocene) were modeled. Due to the thickness the Miocene layer was divided into further three layers to simulate the flow systems in a detailed manner. It was assumed that the bedrock is an impermeable layer (see Figure 1). In the model, the northern Tokaj Mountains active (no flow) boundary conditions were set to variable cell potential, while the rest of the border areas were set at constant pressure on the cells (Figure 4).

The hydraulic conductivity is given by zones based on the results of geophysical measurements. The value of the infiltration was chosen from literature and field measurements for this study, but in the future the distribution of infiltration throughout will be calculated for the entire area by an in-house program. The modeling results show the field of water relief (Figure 5). These data will be calibrated by real measurement results in the next phase of the project. The water levels in the model differed from the real water level, so we built no real monitoring wells into the model.

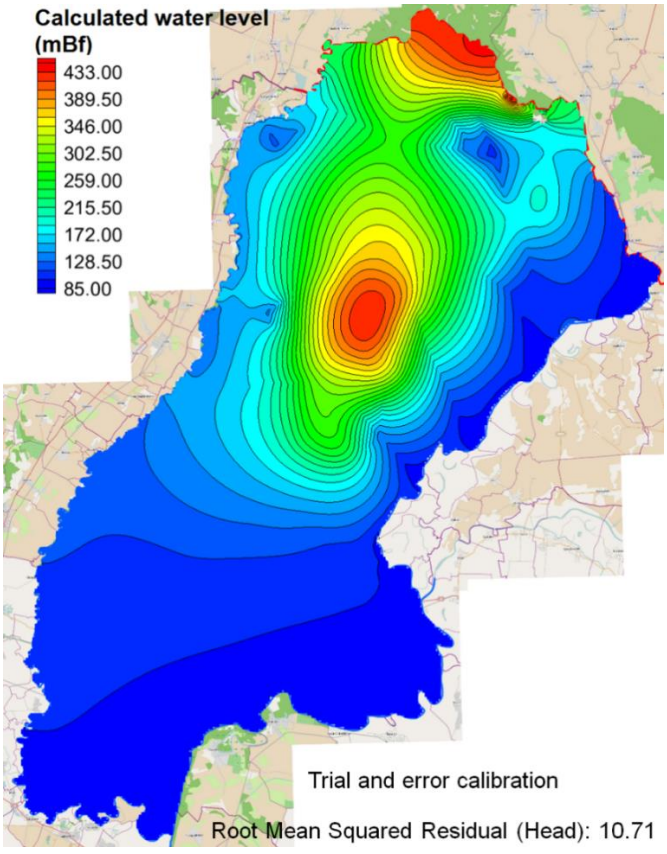

Figure 5
Water levels calculated by GMS

5. GEOPHYSICAL AND INVERSION METHODS TO IMPROVE THE CALIBRATION RESULTS OF THE FLOW MODEL

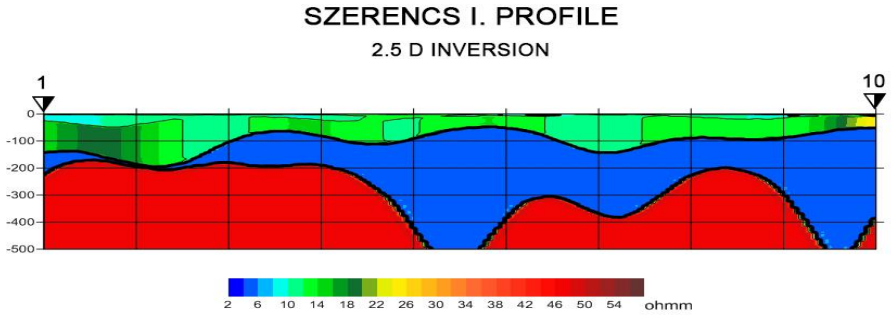

Figure 6
VES measurement result profile (N-S)

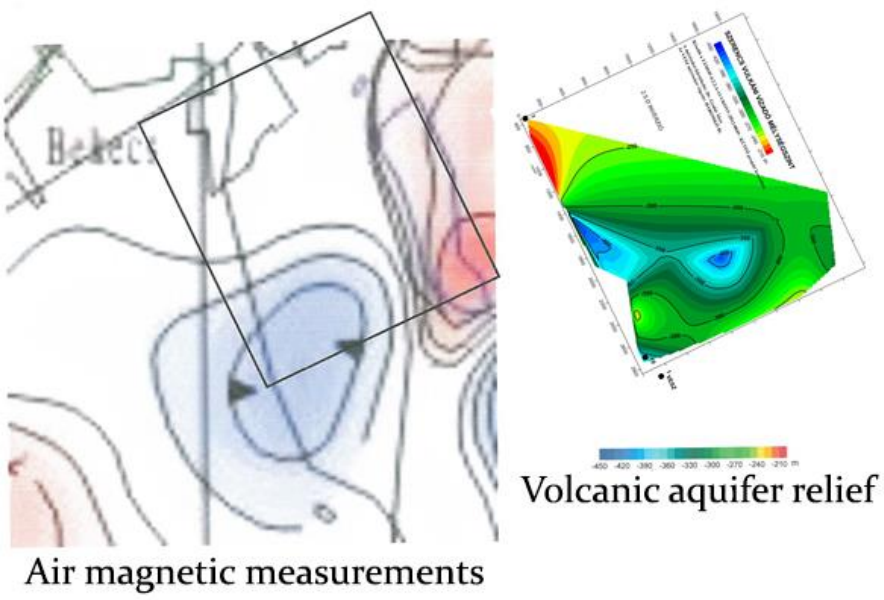

Figure 7
Comparison of two measuring results

In 2013 we carried out surface geophysical measurement in Szerencs for geothermal exploration, combining geoelectric, geomagnetic and hydrogeological studies. Vertical electrical sounding (VES) and multielectrode measurements are a geophysical method for investigation of a geological medium. The method is based on the estimation of the electrical conductivity or resistivity of the medium. The estimation is performed based on the measurement of voltage of electrical field induced by the distant grounded electrodes (current electrodes).

The results of the measurements show a fault system deep in the research area. The detection of this fracture was the main goal of the research, and the perception of it was possible with surface geophysical methods (VES method, geomagnetic methods). The deep warm water flows through the fault system, and then up to the shallow monitoring wells. In the investigated area three different layers can be found. The top layer is Pannonian sediment (green), the middle layer is volcanic weathered tuff (blue), and the bottom is the Miocene lava rocks, like andesite or rhyolite (Figure 6). The sudden position change of the lava rock marks the fault in the depths (Figure 7) [1].

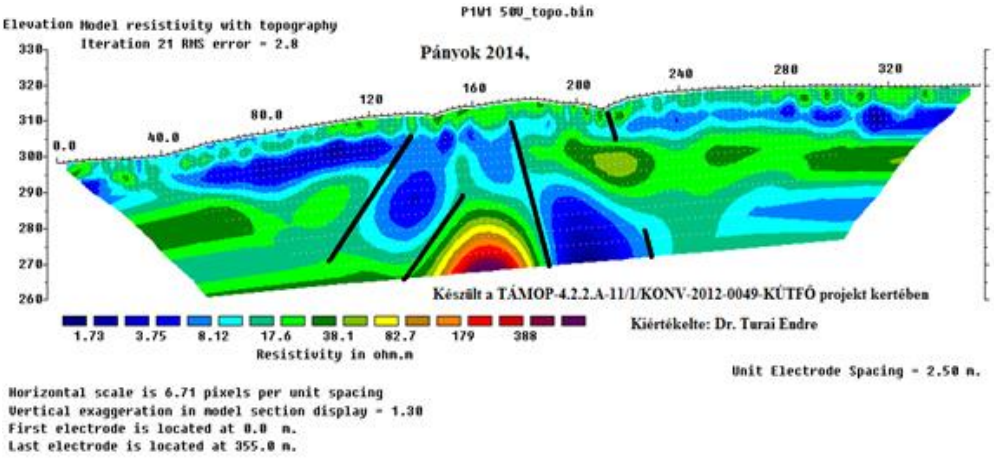

Figure 8
Multielectrode measurement profile in Pányok

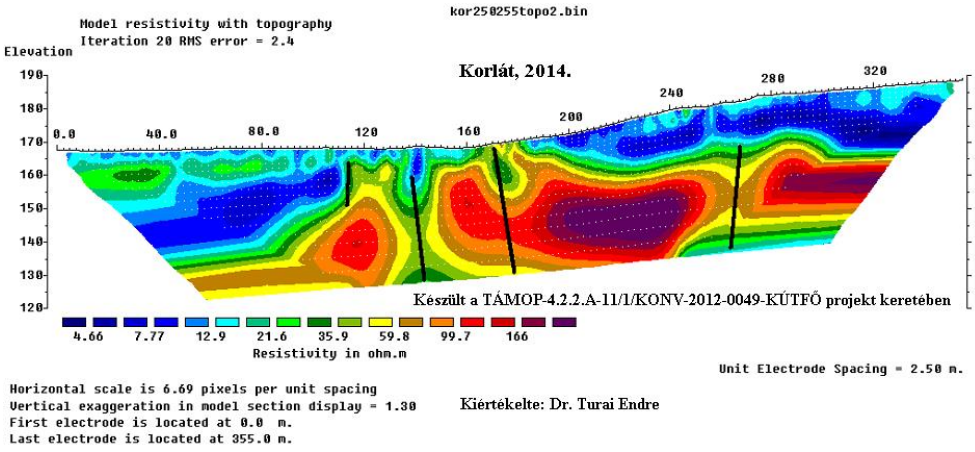

Figure 9
Multielectrode measurement profile in Korlát

In 2014 we made multielectrode geophysical measurements in Korlát and Pányok, which are villages located in the western part of the Tokaj Mountain. In these settlements there are many tepid and thermal water wells. With this geophysical measurement we can learn the geological and hydrogeological system. This measurements can help us to improve the calibration results of the flow model. With the help of geophysical methods, the important hydrogeological parameters of the layers (porosity, hydraulic conductivity, permeability) can be estimated. The results of the measurements are shown in Figures 8 and 9.

6. SUMMARY

The Tokaj Mountains are one of the most well-known volcanic mountain ranges in Hungary. They are located in the north-eastern part of the country. Their geology and mineralogy have been studied thoroughly; however, we have little knowledge about the hydrogeological features. Research on the hydraulics of groundwater and water-rock interactions had been performed earlier, but a detailed understanding of the flow system was lacking. A goal of the WELL aHEAD project (launched in 2012 at the Institute of Environmental Management, University of Miskolc) is to study the groundwater flow system of the Tokaj Mountains in detail. In the Tokaj Mountains we made many field geophysical measurements that help the understanding of the hydrogeological system. Remote geophysical measurements were used to clarify the hydrogeological model of the mountains.

7. ACKNOWLEDGEMENT

The research was carried out in the framework of the Sustainable Resource Management Center of Excellence at the University of Miskolc, as part of the TÁMOP-4.2.2/A-11/1-KONV-2012-0049 “WELL aHEAD” project in the framework of the New Széchenyi Plan, funded by the European Union, co-financed by the European Social Fund.

8. REFERENCES

[1] FEJES, Z.–SZŰCS, P.–KOMPÁR, L.: Thermal water research in Szerencs region for the purpose of geothermal energy. *MicroCAD XXVI. International Scientific Conference*, 2012, 201–206.

[2] GYULAI, Á.–TOLNAI, É. E.: 2.5D geoelectric inversion method using series expansion. *Acta Geodaetica et Geophysica Hungarica*, 2012, 47 (2), 210–222.

[3] KISS, G.: *The Zemplén Nature Protected Area. The name of the mountain, boundaries and landscapes*. Eger, Bükki publisher, 2007.

[4] SZŰCS, P.–FEJES, Z.–SZLABÓCZKY, P.: Thermal water research in great depth and unknown area in Szerencs region. *Electronic Technical Papers*, 2012, 11, 303–313.

[5] VKKI, ÉKÖVIZIG: Watershed Management Plan, 2–5. Tokaj-hegyalja, 2010.